AIAA DESIGN COMPETITION

BeLI

TEAM BELIEVERS

2022-2023

AIAA

LIÈGE université

BeLI

Disaster Response Search and Identification Attritable Air Vehicle (Dr. SAAV)

RANGE

TAKE OFF

LANDING

CRUISE MACH

PRICE

5240 NM

1782 FT

1421 FT

0.86

USD 2,100,000

"Playing with boundaries"
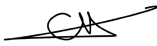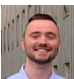
355 LBS

6671 LBS

3036 LBS

MTOW

MISSION PAYLOAD

ZFW

DIMENSIONS

SPAN
29.5 FT

LENGTH
26.2 FT

The team - BeLIevers

Academic year 2022-2023

	Last name	First name	Student ID	AIAA number	Signature
	BATLLE MARI	Lucas	s190873	1404180	
	BIZ	Cem	s225522	1405457	
	DUPONT	Thibaut	s194123	1405927	
	GERARD	Jonas	s226592	1404179	
	PAGE	Louis	s226670	1404181	
	PESESSE	Justin	s220873	1405372	
	VAN HOUTE	Mathieu	s225607	1406026	
	VISEUR	Lucas	s191096	1405543	

Faculty advisors

NOELS Ludovic

DIMITRIADIS Grigorios

Project advisors

CROVATO Adrien

LAMBERT Thomas

BUDO Arnaud

Contents

1   Introduction

In our world of changing climate, the weather is more likely to be a cause of death than a simple subject to discuss. From cyclones savaging the blue sky to typhoons, natural disasters are expected to increase in amplitude and in frequency in the future [1]. In 2021, according to the website *Statista* [2], a total of 97 natural disasters occurred in the United States, most of them being severe thunderstorms.

The necessity to design an air vehicle to find and identify victims in need of first help, potentially within a sea of other debris in less than ideal flight condition, becomes more of a duty than a need. For that purpose, the American Institute of Aeronautics and Astronautics (AIAA) posted a request for proposal for their annual design competition. The aircraft to design has to be a Disaster Response Search and Identification Attritable Air Vehicle (Dr. SAAV).

In this regard, the BELIEVERS team designed the BELI, which has the particularity to take advantage of the boundary layer ingestion (BLI) technology to reduce its overall drag and consequently its fuel consumption. In this aspect, the BELI performance is first studied as if BLI would not occur. Then, a more in-depth analysis of the BLI enhanced performance is performed. This low cost aircraft stands out from the others with its fast arrival on scene, long loiter and capability to reach further lands.

2   Mission requirements

The main (primary) mission consists in reaching as quickly as possible the disaster place in order to identify potential victims. Once identified, the aircraft is expected to provide life-saving drinking water and a communication radio in order to be connected with people that may help them. This primary mission is illustrated in Figure 2.1. Some relevant characteristics of the BELI are summarized hereafter in Table 2.1, and compared with optimal AIAA key performance parameters (KPPs).
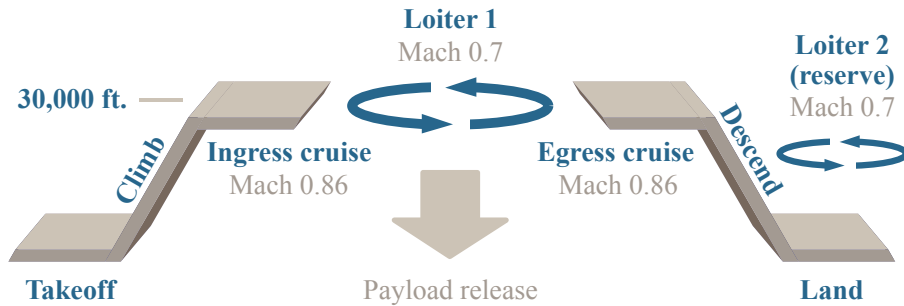
Figure 2.1: Illustration of the primary mission.

Table 2.1: Overview of the BELI characteristics and comparison with optimal/threshold AIAA main KPPs (green: objective reached).

Requirement	BeLI
Mission payload weight	**355** lbs
Ingress range at Mach **0.86**	**960** nm
Egress range at Mach **0.86**	**2,110** nm
Loiter time at Mach **0.7**	**5.3** h
Total range	**5,220** nm
Take-off distance	**1,471** ft
Landing distance	**1,421** ft

The objectives that must be followed by the design of the BELI are:

- the ability to operate in rough weather and having a simple design. Protuberances and control effectors must then be minimized because they could be damaged, caught/tangled in brush or affected by excessive dirt/debris;

- a small overall size to facilitate logistics;

- minimal operational logistics;

- having a beneficial trade-off between cost and attritability, because of the potential loss of vehicle due to harsh weather;

- the Initial Entry into Service (EIS) expected to be 2028.

As secondary missions, the loiter time and the cruise range need to be maximized separately. As the BELI can be deployed anywhere in the world it is essential to maximize its range. These missions are submitted to the same performance parameters. Results are provided in Table 2.2, with the range determined from the payload-range diagram of Section 7.4.

Table 2.2: Ranges of the BELI for the secondary missions.

	Max. loiter (Mach 0.7)	Max. cruise (Mach 0.86)
BELI max. range [nm]	7242	6872

Finally, the BELI must follow the Federal Aviation Administration (FAA) Title 14 in the Code of Federal Regulations (CFR). The BELI is a normal category aircraft, and then respects the Airworthiness Standards described in the Part 23 [3].

3 Market analysis

According to a report of *MarketsandMarkets* [4], the UAV market is in expansion. From 2022 to 2027 it is expected to grow from \$ 26.2 billion to \$ 38.3 billion, representing an increase of \$ 12.1 billion with a CAGR (Compound Annual Growth Rate) of 7.9%. Another report, published by the *Allied Market Research* [5] mentions an even higher CAGR, from 2020 to 2030, equals to 10.0%. Historically, drones are mostly used among defense forces, but investments by both public and private organizations for civil and commercial applications were recently made [4]. These investments led to significant advancements in the civil and commercial sector. The BeLI is an Unmanned Dr.SAAV, and the primary targeted clients are the public organizations. Therefore, it is also part of this tendency. In addition, search and rescue UAVs are by definition very dependant on their sensors and subsystems. The evolution of the sector is therefore a crucial parameter and is directly linked.

Geographically, North America is the region with the largest amount of UAVs, but an important market growth is expected in Asia-Pacific (essentially China and India), particularly for civil and commercial drones. *Allied Market Research* [5] predicts a CAGR of 15.6% for this region only. Moreover, a map taken from the annual technical report *WorldRiskReport 2021* published by the German University *Ruhr University Bochum* [6] is shown hereafter in Figure 3.1. This map illustrates the main relative disaster exposures per country and takes into account events such as earthquakes, tsunamis, coastal flooding, riverine flooding, cyclone, droughts and sea level rise. According to this map, North America and Asia-Pacific regions are very highly exposed to natural disasters.
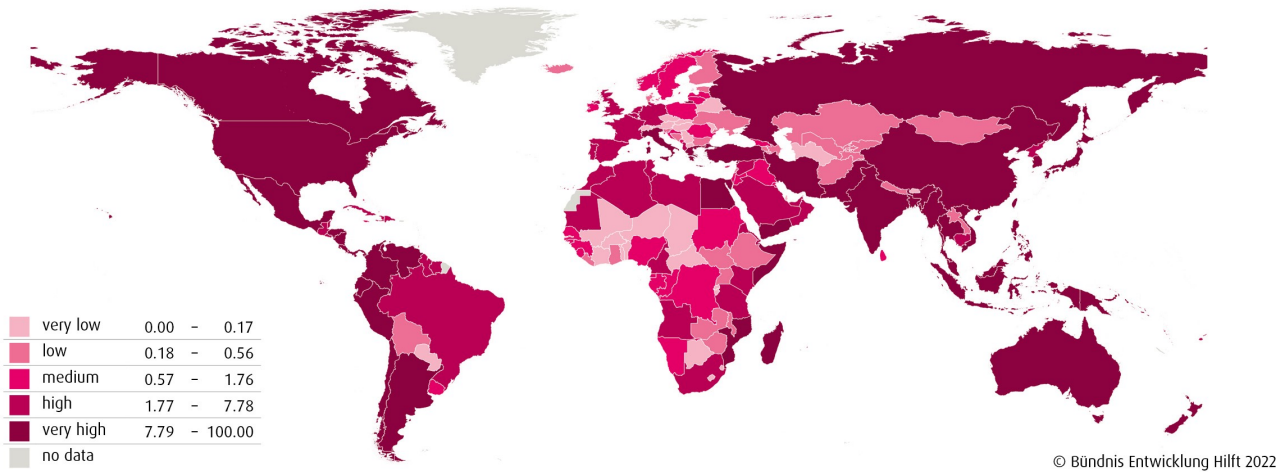
Figure 3.1: Map of the relative natural disasters per country [7].

Hence, according to predictions, the region to focus for the market of the BeLI is definitively the Asia-Pacific region and North America. North America is the safest option as the market is already well established there, so that the primary target remains the North American public sector. As a matter of fact, the number of key player in the market of long range rescue UAVs is very small and the used technologies are close to those used in military sector. The leading companies are *Northrop Grumman Corporation*, *General Atomics Aeronautical* and *Israel Aerospace Industries*.

4 Design methodology

The methodology followed by the BELIEVERS to design the BELI is summarized in Figure 4.1 below. First, it is important to know the mission to be achieved and search for aircraft following similar missions. In parallel, technologies the team wants to involve in the design must be compared to get the most relevant ones for the mission. From there, a first draft design is made and the initial guess for the Maximum Take Off Weight (MTOW) and the Zero Fuel Weight (ZFW) are calculated.
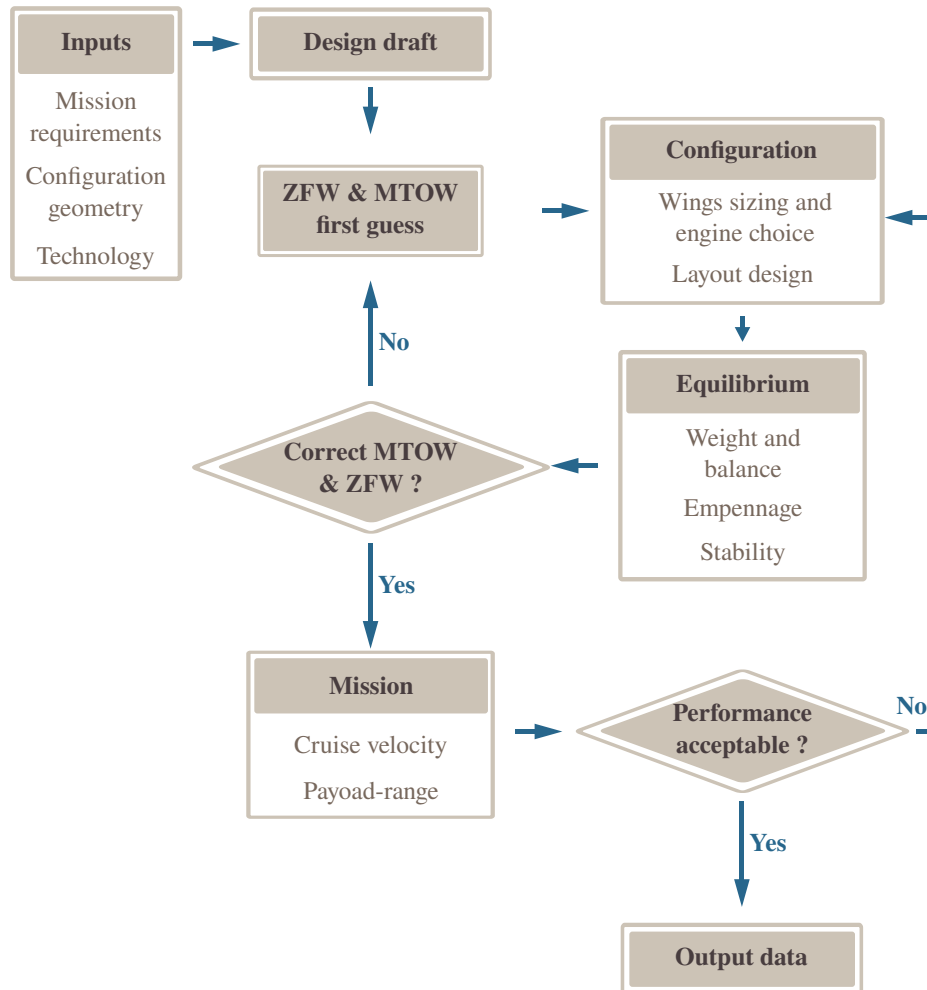
Figure 4.1: Methodology used for the conceptual design [8].

Then, more detailed properties are computed, and all parts of the aircraft are sized. Once every component is tailored, the evolution of the configuration through time is considered, with a stability check. If the aircraft is not stable enough (or too stable), new MTOW and ZFW are guessed and another iteration starts.

Finally, once the equilibrium is satisfied, missions performance is checked. Once more, if it is not acceptable, the configuration is changed. In the opposite case, the conceptual design is thus finished and the preliminary design can start. In addition, a constant trade analysis and a trade-off study must be performed in order to be sure that the current configuration is the optimal one.

5 Configuration

5.1 Existing configurations

The number of UAVs following all mission requirements is very low. This section acts just as a starting point of the conceptual design. As a matter of fact, aircraft which combine a long range, a relatively high speed and a small MTOW are private jets, even though they are still too heavy for the current mission. Figure 5.1 shows the aircraft from which the configuration of the BeLI has been inspired.

(a) Dassault Falcon 2000 MRA[1].

(b) Northrop Grumman MQ-4C Triton[2].

Figure 5.1: Existing aircraft for the same kind of requirements.

On one hand, Figure 5.1a shows the Dassault Falcon 2000 MRA, which is a maritime "multi-role" aircraft. It has then several purposes, including search and rescue, monitoring or surveillance. It should be noted that this aircraft is characterized by a low-wing and a cruciform tail configuration to prevent any interaction with the air ingested by the engines. On the other hand, The Northrop Grumman MQ-4C Triton (Figure 5.1b) is interesting because it is a high altitude and long range reconnaissance UAV. It is a single engine aircraft, with a middle wing position and a V tail to prevent any interference between the empennage and the exhaust. The BeLI is partially inspired from its fuselage shape. Furthermore, even if it is still a prototype, the Aurora D8 airliner shown in Figure 5.2, imagined by the NASA, is a source of inspiration for the BeLI. It has two important characteristics: its use of the BLI technology, and the use of the fuselage as a lifting body in addition to the wing. The BLI implementation technology is the central motivation of the design of the BeLI, and will be discussed in much more details in next sections. However, the concept of lifting body is not retained for the BeLI to avoid any cost increase related to the manufacturing of the fuselage.

Finally, it must be emphasized that the Aurora D8 is a prototype airliner and that no additional characteristics are consequently retained except the BLI implementation.

---

[1]https://images.dassault-aviation.com/f_auto,q_auto,g_center,dpr_auto/wp-auto-upload/1/files/2017/05/150610_ER_Falcon2000MRA_S.jpg
[2]https://upload.wikimedia.org/wikipedia/commons/thumb/2/2f/MQ-4C_Triton_Test_Flight_with_Multi-Intelligence_Upgrade.jpg/1280px-MQ-4C_Triton_Test_Flight_with_Multi-Intelligence_Upgrade.jpg

Figure 5.2: NASA prototype Aurora D8[1]- BLI inspiration.

5.2 Main design choices

Aircraft category

The BeLIevers chose to develop only one single aircraft which will be able to fulfill all mission requirements. Obviously, designing a single aircraft is less expensive than a family. In addition, it allows to make it more versatile and therefore more likely to cope with potential new similar missions. Concerning the aircraft control, a remotely piloted system is preferred for the BeLI. It has the advantage to offer much more freedom in terms of flight decisions compared to an autonomous system.

Engine

The BeLI is a single engine aircraft. A problem while using only one engine for propulsion is the absence of redundancy and therefore the lack of safety it can generate. Nevertheless, this condition is less relevant for UAVs. In addition, as the BeLI goes through rough weather, the probabilities for the aircraft to crash are greater than for most other ones: the aicraft use is limited. Therefore, losing only one engine along with the aircraft presents a better cost aspect. Finally, this choice helps reducing the MTOW of the aircraft, which has to be relatively low.

Concerning the location of the engine, the main characteristic of the BeLI is its use of the Boundary Layer Ingestion technology (BLI). The principle is to reduce the drag and subsequently the fuel consumption by making the engine ingest the flow with the lowest speed possible. This can be done by positioning the engine in order to benefit from the low speed of the boundary layer at the fuselage neighborhood (see Section 6.4.1). Different configurations are investigated as represented in Figure 5.3 and Figure 5.4 (more details in Section 6.4.1).

Figure 5.3a is the classical theoretical model for BLI aircraft. It nevertheless provides asymmetric airflow ingested by the engine with the tail passing through the intake. The second configuration in Figure 5.3b addresses this

---

[1]https://upload.wikimedia.org/wikipedia/commons/9/96/MIT_and_Aurora_D8_wide_body_passenger_aircraft_concept_2010_%28cropped%29.jpg

problem by mounting the tail on the engine nacelle. However, said configuration is tedious in a structural point of view. Figure 5.4 is also suitable for BLI, structurally more robust and in a second concern more original than mainstream BLI prototype. This configuration is therefore chosen for the design of the BeLI.

(a)   (b)
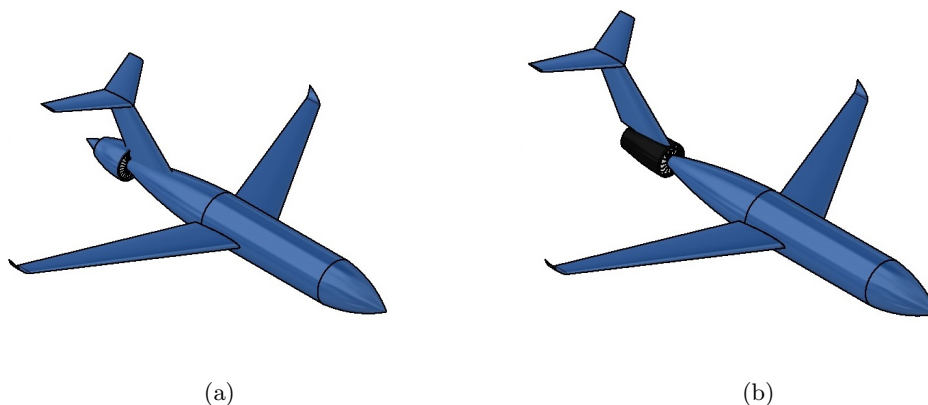
Figure 5.3: Configurations for BLI with the engine at the rear of the fuselage.
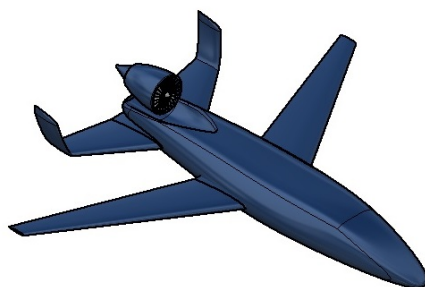
Figure 5.4: Configuration for BLI with the engine on the top end of the fuselage.

Lifting surfaces

A high wing configuration has been preferred. It has the advantage to have a better lateral stability than the mid and low wing configurations since the center of gravity is located under the center of pressure of the wing. Due to the center-back location of the engine, a conventional tail is not suitable. The choice is therefore made to have the Figure 5.4 configuration, which involves a U-shaped tail. This shape as the advantage not to interfere with the air ingested by the engine.

Fuselage

The shape of the fuselage is once again optimized to take advantage of the BLI. It means that the end of the fuselage is shaped to partially surround the engine, which will take as much benefit as possible of the boundary layer produced by the upper surface of the fuselage. Furthermore, the selected shape enables to hold the payload, release it efficiently and reduce the drag. Although the geometry becomes more complex and is then less relevant for rough weather, the overall fuselage shape is still close to standard aircraft shapes. Hence, this geometry is kept.

5.3 BeLI CAD

CAD and 3-views models of the BeLI are illustrated in Figure 5.5 and Figure 5.6.
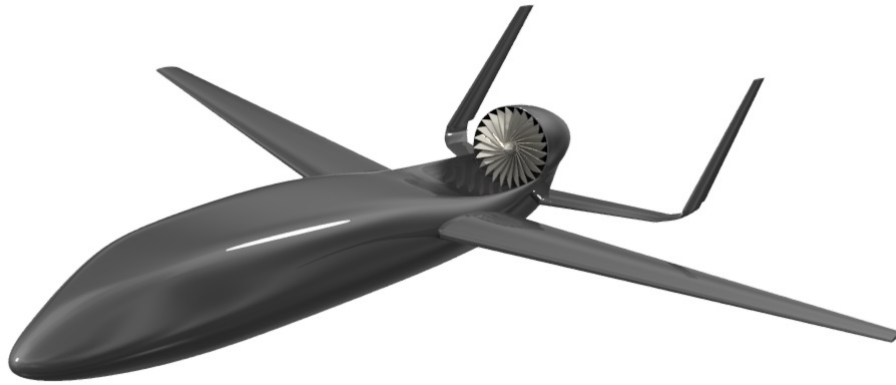
Figure 5.5: CAD model of the BeLI.
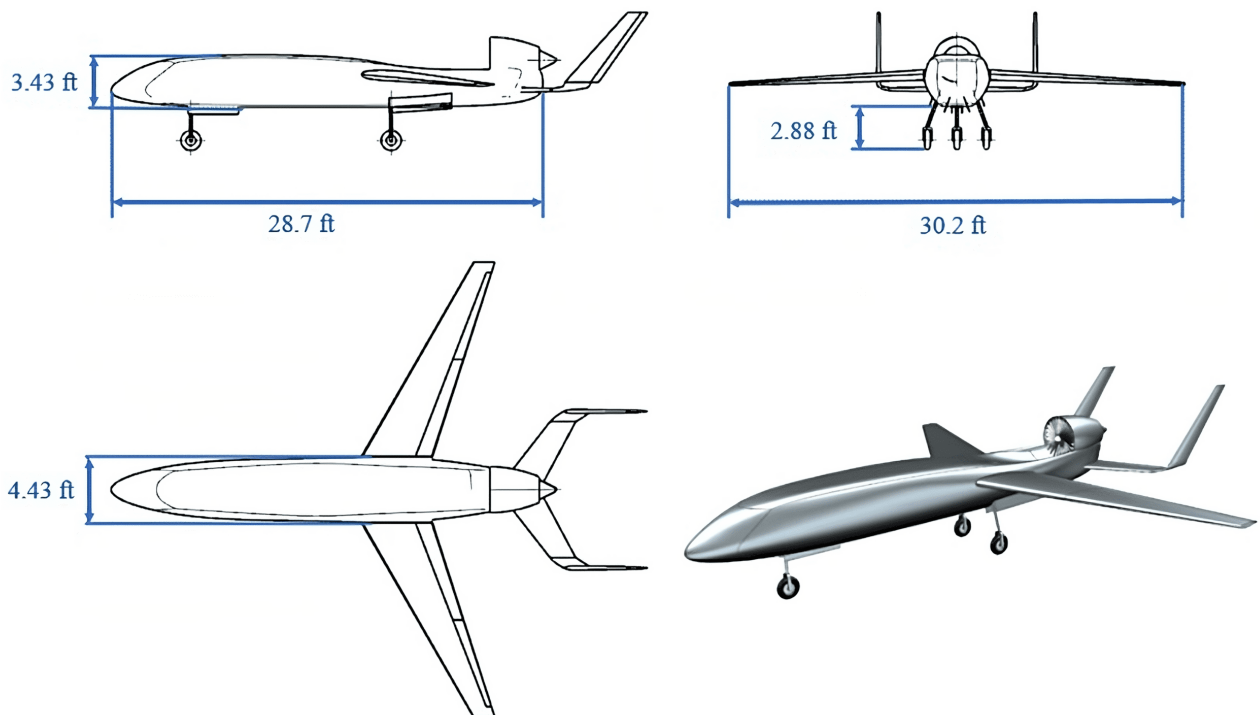
Figure 5.6: CAD 3-views model of the BeLI.

6 Component design

6.1 First estimations

The first weight estimation is the initial step of the conceptual design methodology. In order to compute it, the following equation has been used [9] (Equation 6.1):

$$W_0 = W_{\text{crew}} + W_{\text{payload}} + \left(\frac{W_f}{W_0}\right) \cdot W_0 + \left(\frac{W_e}{W_0}\right) \cdot W_0 \ , \tag{6.1}$$

where W_0 is the takeoff weight, W_{crew} the crew weight (null for an UAV), W_{payload} the payload weight (including sensors, subsystems, and mission payloads), W_f the fuel weight and W_e the empty weight.

First, the mission payload weight is given in Section 2, but sensors and subsystems' payload weights must be estimated. The first estimation then follows the initial estimations of AIAA requirements, which are $W_{\text{sensors}} = 228$ lbs and $W_{\text{subsystems}} = 222$ lbs.

Second, the fuel weight ratio is estimated with Breguet range equations for cruise and for loiter, defined hereafter [9]. For cruise segments, the relationship between the weight before cruise W_{i-1} and the weight after cruise W_i are given by:

$$\frac{W_i}{W_{i-1}} = \exp \frac{-RC}{V(L/D)} \ , \tag{6.2}$$

where R is the range, C the specific fuel consumption, V the velocity and (L/D) the lift-to-drag ratio. Concerning the loiter segment, loiter weight fractions are given by:

$$\frac{W_i}{W_{i-1}} = \exp \frac{-EC}{(L/D)} \ , \tag{6.3}$$

where E is the loiter time (sometimes called endurance time). Applying the Equation 6.2 and Equation 6.3 to the mission and combining it with some empirical assumptions for takeoff, climbing, and landing weight fractions (see Table 6.1), the first estimation of the fuel ratio is found. All remaining parameters are guessed following empirical formulas from Raymer, Chapter 3 [9].

Table 6.1: Empirical weight fractions for mission segments.

Mission segment	W_i/W_{i-1}
Warmup and takeoff	0.970
Climb	0.985
Landing	0.995

BeLi

In the end, a result convergence is performed and the first guess for the MTOW of the BeLI is **7,700 lbs**. The first guess for the fuel ratio is **35 %**. These first estimations are the basis of all components calculation.

6.2   Wing

In order to determine the wing planform, the geometric parameters of the wing are computed. For stability purposes, the wing's position (high wing) is considered fixed. Also, airfoil and high lift devices are defined with respect to the requirements. Finally, forces which are lift, drag, and pitching moment applied on the wing have been computed. If the computed data are sufficient enough to carry on the mission, the last geometrical parameters are designed by optimizing the configuration. If not, the process is iterated by modifying certain parameters until requirements are satisfied.

6.2.1   Wing planform

In order to define the general characteristics of the wing, the reference wing area is critical to be found. From the preliminary design study, according to Raymer [9], the wing area can be estimated from the wing loading. By converting the wing loadings through the mission such as takeoff, landing, cruise, sustained turn, etc., wing loadings are converted to an equivalent condition, which is called take-off weight. In order to choose the reference wing loading among different missions, the lowest wing loading is chosen because of the following reasons:

- there is less pressure on the wing because the weight of the aircraft is distributed over a bigger wing area. This increases the fuel efficiency of the aircraft by lowering the amount of lift needed to keep it in the air;

- lower wing loading also results in a lower stall speed;

- an aircraft's agility can be increased with decreased wing loading, making it simpler to control;

- lower wing loading can also result in a softer landing.

After computations, cruise and takeoff wing loading are chosen to be the limit. As a result, the wing area is estimated as 91.5 ft^2 to settle performance characteristics in cruise and take-off with the weight of the aircraft.

The average Aspect Ratio (AR) for General Aviation aircraft ranges between 6 and 11 [10]. Since having a high AR increases the balance of the aerodynamic center AC in terms of good roll response with low induced drag which reduces fuel burn and increases the gliding performance, the initial AR is taken as 10.

Following Raymer's suggestion [9], the quarter chord sweep angle of the wing must be around 30° for aircraft flying at Mach 0.86. The taper ratio is another important parameter that defines how lift is distributed along the span. Tapered wing is aerodynamically more efficient in comparison to the rectangular wing since it decreases the induced drag. But it is also more complex to manufacture. Moreover, because of the reduced mass moment of inertia about the longitudinal axis, the taper enhances the lateral control of the aircraft. By considering all, the tapered wing is preferred on the BeLI. For swept wing, the taper ratio is around 0.2-0.3. The value of 0.3 is retained since it

is the most used in aviation. Swept wing also increases lateral stability by creating a natural dihedral effect. In a spirit of comparison, 10° of sweep is creating 1° of dihedral. To avoid excessive stability, a negative dihedral of -3° is chosen to compensate for the swept wing effect on the stability.

Having a tapered wing affects the tips of the wing on stall condition first. This explains why having a twist is recommended [9]. More specifically, washout enables stalling at the root first while preserving free space around the ailerons for a controlled recovery. Although this also raises the cost of production, a geometric twist of ε = -2° is taken into consideration in this case since it is again a usual value for it [9]. Also, the wing structural weight of the wing is finally computed as 396,89 lb.

Finally, The lift coefficient that the wing must accomplish is obtained by computing the equilibrium of the aircraft. As a consequence, the root angle of attack is fixed at two degrees. Moreover, such a parameter must be designed so that the wing operates at optimal condition at cruise. It must be noted that the angle of attack of the fuselage in cruise is considered as 0° to avoid a lifting body situation which would considerably increase the difficulty of the wing planform design.

All the geometric parameters and dimensions are shown in Table 6.2 and Figure 6.1.

Table 6.2: Wing geometry parameters.

Parameter	Value
Surface area S	91.5 ft^2
Aspect ratio AR	10
Taper ratio λ	0.3
Dihedral Γ	-3°
Twist angle ε	-2°
Quarter chord sweep c/4	30°
Root angle of attack i_w	2°

6.2.2 Airfoil selection

The choice of airfoil affects both the performance of the wing including stall speed, lift and drag as well as the manufacturing costs. Therefore, it is crucial to choose the right airfoil in order to meet performance requirements. Following the objectives, the airfoil that is chosen needs to have a high stall angle in order to delay the stall. It should be noted that the latter parameter of the wing is linked to the stall angle of the airfoil. Also, in order to sustain a low-cost flight, it is vitally important to have a high lift-to-drag ratio, meaning minimizing drag while producing the maximum lift possible through the wing. For the optimum cruising balance, the pitching moment must be as close as possible to zero. Having a small pitching moment will thus improve the balance of the aircraft and reduce the balance effect needed to be produced by the tail. Finally, the lift slope and zero lift coefficient have

to be as large as possible to have a lift in the initial position of the wing (0° angle of attack).

Since the BELI flies in the transonic region, supercritical airfoils are preferred. This specific type of airfoil reduces wave drag which occurs when supersonic shocks appear on the airfoil [11].

Different supercritical airfoils, namely NACA SC 0412, 0406, 0714, 0706 and 1006, are compared in Table 6.3.

Table 6.3: Comparison between the airfoils without flaps at $Re = 7\text{x}10^6$.

Design Objective	0414	0406	0714	0706	1006
$c_{d\,min}$ [-]	0.004	0.003	0.007	0.004	0.005
c_{m0} [-]	-0.09	-0.043	-0.14	-0.11	-0.14
$c_{l\alpha}$ [-]	5.73	6.3	6.8	6.3	6.9
$(c_l/c_d)_{max}$ [-]	75	60	82	95	130
α_{stall} [°]	17	7	17	5	3
α_{L0} [°]	-2.5	-1.7	-4.7	-3	-7
Stall quality	Moderate	Docile	Moderate	Docile	Docile

Another important parameter is having a minimum drag coefficient at the root with a computed incidence angle. In the end, NACA SC 0414 is chosen because it meets all the requirements stated earlier and has also a higher thickness than the others with a maximum thickness to chord ratio of 14%. It will allow for preserving more fuel in the wing, reducing the required space for the fuel tank in the fuselage.

6.2.3 Ailerons

In order to be aerodynamically efficient and easy to manufacture, the plain aileron type is selected for use on the BELI. There are several critical design points which are:

- roll authority at a relatively low speed;

- roll authority at high speeds while having low deflections.

The wing's helix angle as the aircraft rolls at a specific airspeed determines how well the aircraft can be controlled. The Helix angle is given by

$$\text{Helix Angle} = \frac{pb}{2V} \ , \tag{6.4}$$

where p is the roll rate for complete aileron deflection in radians per second, b is the wing span in feet, and V is the airspeed in feet per second [12]. From the literature, for heavy lift aircraft, helix angles are generally $\frac{pb}{2V} > 0.07$, and for the fighter aircraft, its $\frac{pb}{2V} > 0.09$. Since the BELI is between both types, desired helix angle must be over 0.08. Firstly, in order to define the helix angle, the average value of deflection must be determined. From the literature [10], maximum up and down deflections are estimated as $\delta^{up}{}_{a_{max}} = \delta^{down}{}_{a_{max}} = 15°$. In order to account for the fact that the ailerons will stretch during flight and minimize the maximum ground deflection, the calculation of the

anticipated aileron deflection angle was done after multiplying the result by a factor of 0.75 [12]:

$$\delta_A = 0.75 \cdot 0.5(\delta^{up} + \delta^{down}) \ . \tag{6.5}$$

Secondly, the Hershey bar wing equation is used to estimate roll damping (C_{lp}).

Effectiveness is estimated as τ=0.45 [12]:

$$C_{lp} = -\frac{C_{L\alpha} + C_{D0}}{6} \ , \tag{6.6}$$

$$C_{l\delta_a} = \frac{C_{L\alpha}\tau C_R}{Sb}[(b_2^2 - b_1^2) + \frac{4(\lambda - 1)}{3b}(b_2^3 - b_1^3)] \ , \tag{6.7}$$

where $C_{L\alpha}$ is the lift slope, C_R is the root chord, b_2 is the aileron far point from the center of the wing and b_1 is the aileron's closest point from the center of the wing. After the computation, the helix angle can be calculated as followed

$$\frac{pb}{2V} = -\frac{C_{l\delta_a}}{C_{lp}}\delta_A = 0.0823 > 0.08 \ . \tag{6.8}$$

With the starting point of 9 ft to 15 ft from the center of the aircraft, the helix angle matches the condition and the sizing of the ailerons is validated and shown in Figure 6.1.
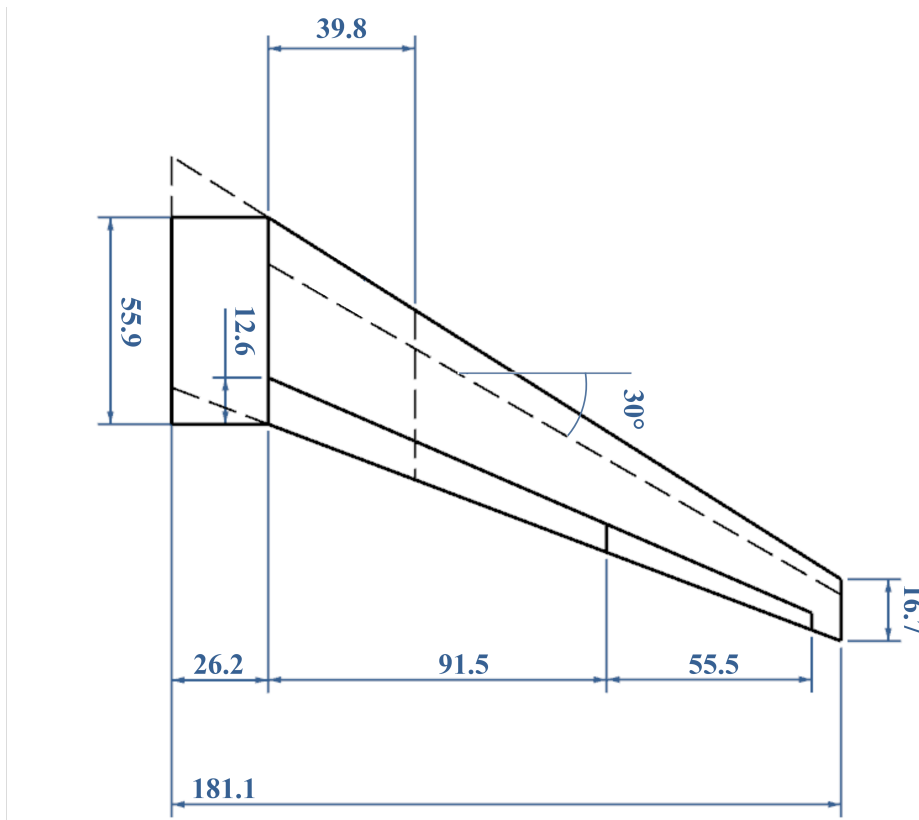
Figure 6.1: Geometric parameters of the wing, dimensions are expressed in ft.

6.2.4 Flaps

Several flaps configurations exist and can be used. For instance, it exists split, plain, single-slotted, double-slotted, or even Fowler flaps. The above order ranks the flaps by aerodynamic effectiveness but also by mechanical complexity. To design the flaps, the maximum lift coefficient of the wing without flaps must first be known.

It can be computed by [8]

$$C_{L,max,clean} = cos\Lambda_{1/4} \cdot 0.95 \cdot \frac{(C_{l,max})_{root} + (C_{l,max})_{tip}}{2} = 1.43 \ , \tag{6.9}$$

where $(C_{l,max})_{tip} = (C_{l,max})_{root} = 1.8$ since the same airfoil is used along the span. Then, the contribution for take-off and landing of the flaps in the lift coefficient can be computed using the methodology described by Pr. Dieter Scholz in his course "Aircraft design" [13].

The configuration chosen for the airplane is single-slotted flaps with a chord ratio of 25%. This configuration is a trade-off between aerodynamic efficiency and mechanical complexity. After computing the additional lift created by the flaps ($\Delta C_{L,max,f}$), the maximum lift coefficient are computed for both take-off and landing flaps configuration. The lift coefficient needed to achieve take-off and landing are respectively 1.58 and 1.76. A leading edge device is therefore not necessary here since the trailing edge flaps will provide enough lift by themselves as it can be observed in Table 6.4. Knowing the maximum lift coefficient for the two different situations, the stall velocities can also be computed.

Table 6.4: Parameters of the wing with single-slotted flaps.

Parameters	Take-off	Landing
Flaps inclination [°]	20	45
$\Delta C_{L,max,f}$ [-]	0.53	0.76
$C_{L,max}$ [-]	2	2.2
Stall velocity [knots]	97.2	60.5

6.3 Empennage

The objective of the empennage is to ensure stability, control and trim. More precisely, the horizontal tail must be capable of balancing the pitching moments such as the ones created by the wing while the fin must provide a restoring yawing moment. In addition, the tail must be designed to provide sufficient control to the aircraft in all critical conditions (e.g. lift-off, take-off, spin recovery, ...). In this section, the configuration and sizing of the tail will first be discussed. Then, particular attention will be given to the airfoil selection as well as the design of the control surfaces.

6.3.1 Configuration

The BeLI is characterized by a U-tail configuration. This choice was made due to the constraints imposed by the boundary layer ingestion implementation. In particular, the engine must be positioned as far as possible to the rear of the aircraft to ensure the BLI's effectiveness. Therefore, a conventional tail is not suitable and the U-tail seems to be the simplest solution. The latter allows not to interfere with the air ingested by the engine while still ensuring the control and stability of the aircraft as discussed previously. However, it should be noted that this configuration requires a heavier horizontal tail to support the additional load. This element will be taken into account during the empennage design.

6.3.2 Sizing methodology and planform

As stated above, one of the objectives of the empennage is to ensure the stability of the aircraft. As a consequence, the various tail parameters were optimized to guarantee both static and dynamic stability of the BeLI. More precisely, the empennage sizing process was performed so that the aircraft is in longitudinal equilibrium. In other words, both force equilibrium and pitching moment around the center of gravity equations had to be satisfied. These relationships are

$$C_L - C_{L_W} - C_{L_T} \frac{S_T}{S_W} = 0 \tag{6.10}$$

$$C_{m_0} \frac{x_{CG} - x_{AC_w}}{\bar{c}_W} + C_{m_T} - C_{L_T} \frac{S_T L_T}{\bar{c}_W S_W} = 0 \tag{6.11}$$

with x_{CG} the distance between the nose and the center of gravity of the aircraft and x_{AC_w} the distance between the nose of the aircraft and the aerodynamic center of the wing. In addition, $\bar{c}_W$ represents the mean aerodynamic chord of the wing while L_T is the lever arm between the wing and the horizontal tail. Finally, S_W and S_T are the surfaces of the wing and horizontal tail, respectively. Once these relationships were satisfied, the aircraft was considered to be in longitudinal equilibrium and the empennage parameters were assumed to be optimized.

As suggested by Raymer [9], the empennage surfaces were obtained using the vertical and horizontal tail volume coefficients, respectively c_F and c_T. These variables are defined as

$$c_F = \frac{L_F S_F}{b_W S_W} \qquad \text{and} \qquad c_T = \frac{L_T S_T}{\bar{c}_W S_W}, \tag{6.12}$$

with L_F the lever arm between the wing and the vertical fin, S_F the surface of the fin, and b_W the span of the wing. More precisely, typical values of aircraft volume coefficient that are as close as possible to the BeLI configuration were selected to compute the empennage surfaces [9]. In addition, it should be noted that the lever arms are considered as the ones that guarantee the equilibrium of the BeLI, as mentioned above. These parameters are equal to 11 ft for the horizontal tail and 15 ft for the fin. The resulting total area for the horizontal and vertical

tail is 20.3 ft^2 and 16.7 ft^2, respectively. Such values are coherent with typical wing-to-empennage area ratio range [9]. However, since the BeLI is composed of two identical fins, each of them is characterized by a surface of 8.35 ft^2, which corresponds to a half of the calculated value.

In order to perform the sizing process, some assumptions had to be made. First of all, it was decided that the root chord of the fin, taken without the rudder, should be designed to correspond to the tip chord of the horizontal tail. This choice was made to ensure the structural integrity of the U-tail configuration but also to have a rudder extending from the tip to the root of the fin. More information about this last detail is provided in Section 6.3.4. Then, using typical values from Raymer [9], aspect ratios and taper ratios were assumed. As for the taper ratios, both were set at 0.6. According to Raymer, this parameter is generally between 0.2 and 0.6. The higher value in this range was selected as a higher taper ratio tends to increase the structural strength and stiffness of the empennage. Such a characteristic is required for the BeLI, since the horizontal tail must be able to support the fin and that the whole empennage must withstand shocks when the aircraft approaches sonic conditions. On the other hand, the horizontal tail aspect ratio was set at 4. A typical range for this parameter is between 3 and 5, for aircraft with similar missions and dimensions of the BeLI [9]. As it can be observed, the middle value of this range was arbitrarily selected. As stated above, the root chord of the fin was designed to correspond to the tip chord of the horizontal tail. As a consequence, the aspect ratio could be calculated and is equal to 1.3. This value is consistent with the typical range suggested by Raymer, which is from 0.6 to 2. On the other hand, the sweep angle of the horizontal tail is set to be 35°. This parameter is usually fixed at about 5 degrees more than the one of the wing [9]. The tail is more swept, it admits a greater Mach number. Therefore, this choice avoids the loss of efficiency of the elevators due to possible shocks. In addition, the sweep angle of the fin is set to be 35°. Such a value was needed to ensure the stability of the aircraft. Furthermore, this value is coherent with the typical range for this angle, which is 35° to 55° [9]. The final geometric parameters of the horizontal and vertical tails, resulting from the previously described method, are represented in Figure 6.2.

It should be noted that the incidence angle of the horizontal tail was fixed using Raymer's approach [9]. This value was obtained using the fact that

$$i_T = \alpha_T - \alpha_f + \varepsilon \simeq -0.56°$$

with α_T the desired tail angle of attack in cruise. The latter was calculated with the help of the lifting line theory and ensures both stability and control of the aircraft since it results from the sizing methodology, as discussed above. On the other hand, α_f is the fuselage angle of attack in cruise, which is decided to be equal to 0°, as explained in detail in Section 6.2. Finally, ε represents the downwash angle. such a parameter can be computed using an approximation based on the wing configuration [14], which is

$$\varepsilon \approx \frac{d\varepsilon}{d\alpha}(\alpha_{root} - \alpha_{LO_{root}})$$

with α_{root} the wing angle of attack at its root and $\alpha_{LO_{root}}$ the wing zero-lift angle of attack at its root. On the other
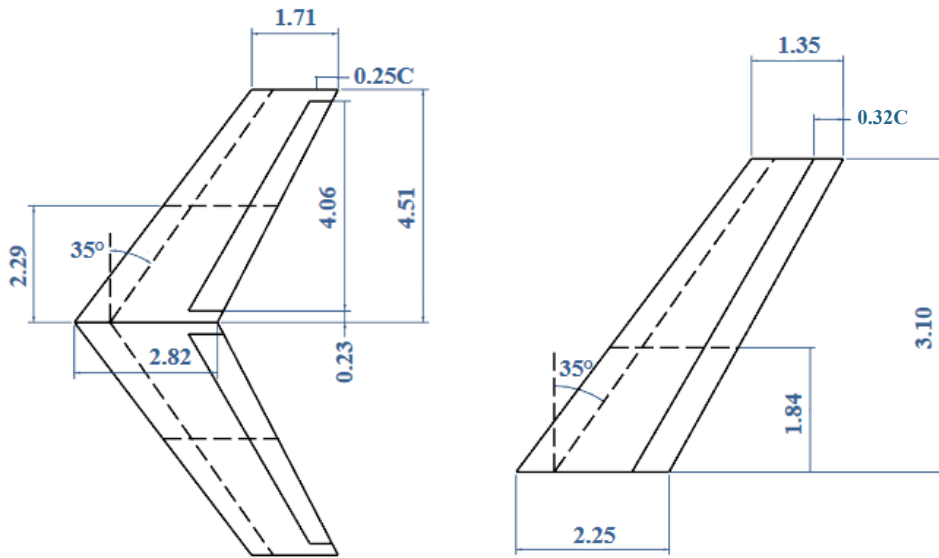
Figure 6.2: Representation of the horizontal (left) and vertical (right) tails, length dimensions are expressed in ft.

hand, the downwash gradient, $\dfrac{d\varepsilon}{d\alpha}$, was obtained using [14]. As it can be observed, the resulting incidence angle is negative. This is due to the fact that the empennage of the BELI is designed to be characterized by a negative lift in order to guarantee stability.

Finally, the tail location had to be fixed. The positioning of an aft horizontal tail, such as the one of the BELI, is crucial to the stall characteristics. If the tail is in the wake of the wing during the stall, a loss of control will result [9]. Therefore, the empennage is positioned in the part "Best location for tail", as represented in Figure 6.3. It should be noted that such a position was also selected because it allowed to improve the longitudinal stability of the aircraft by increasing the vertical distance between the wing and the tail.
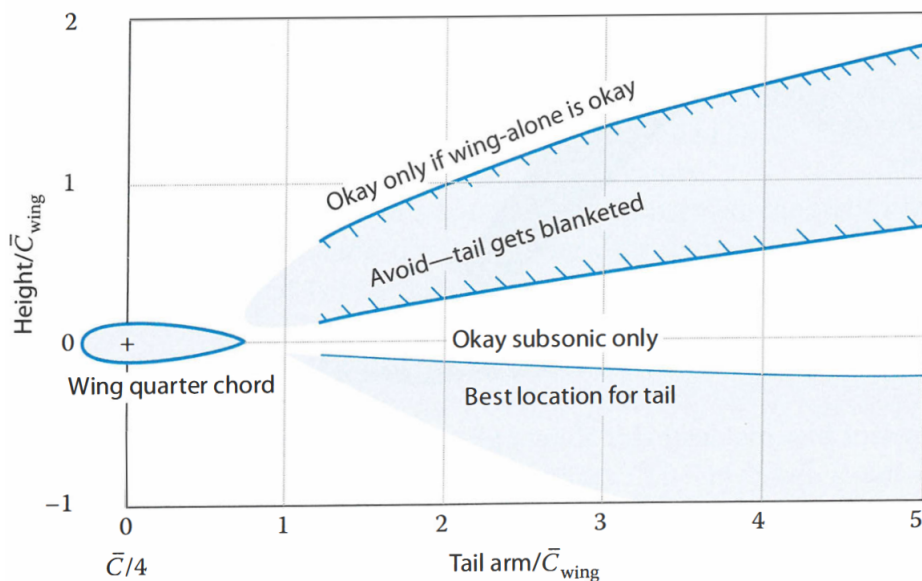
Figure 6.3: Aft tail positioning [9].

6.3.3 Airfoil selection

A symmetrical profile was chosen for both the horizontal and vertical tails of the BeLI. This choice was made because this type of airfoil tends to provide a more uniform lift distribution and provides greater stability than a cambered one. In addition, choosing a symmetrical airfoil seems to be more cost-efficient, as this shape is easier to manufacture. Moreover, it was decided that the same profile would be chosen for the whole empennage in order to eventually decrease further the costs.

On the other hand, it should be noted that the thickness of the airfoil was chosen through a trade-off. This parameter should be selected in such a way that it is large enough to guarantee the structural integrity of the BeLI but should be kept small enough to reduce the weight and the drag of the tail. In addition, selecting a sufficiently thin and swept tail tends to reduce the probability of shock occurrence whenever the BeLI approaches sonic conditions.

For all these reasons, the symmetrical supercritical airfoil N0011SC-IL was selected. Such a choice was made because the supercritical profile tends to reduce the shock appearance when the BeLI approaches sonic conditions. In other words, this choice allows the aircraft to have good overall performance and to be efficient. In addition, this airfoil is characterized by a thickness of 11%. Such a value seems to be a good compromise on the thickness of the empennage profile. Finally, it should be noted that this airfoil is a modified version of the NACA0011. The latter was not chosen because it is not well suited to the transonic regime, as it tends to increase the occurrence of shocks.

6.3.4 Control surfaces

The tail control surfaces correspond to the elevators and rudder, which are responsible for longitudinal and lateral control, respectively. Their design methodology was based on empirical correlations provided by Raymer [9] and Sadraey [10].

First of all, the elevator-to-tail chord ratio, $\dfrac{C_e}{C_T}$, is set to 25% while the rudder-to-fin chord ratio, $\dfrac{C_r}{C_T}$, is fixed at 32%. By comparing the values provided by the two authors, it can be deduced that a typical range for these ratios lies between 20 and 50%. However, the values of 25 and 32% were selected because these are typical for the category of aircraft to which the BeLI belongs.

Then, it was decided that the rudder would extend from the tip to the root of the two fins of the BeLI. In other words, the rudder-to-fin span ratio, $\dfrac{b_r}{b_F}$, was fixed to 1. This choice was made to ensure sufficient vertical control of the aircraft. On the other hand, Raymer and Sadraey state that a typical value for the elevator-to-tail span ratio, $\dfrac{b_e}{b_T}$, is between 80 and 100%. In the case of the BeLI, the average of this range was selected, which is 90%. More precisely, it was decided that the elevator should be placed in the middle of the horizontal tail. In other words, the elevator extends from the tip of the tail, starting at 5% of b_T. Such a choice was made to avoid any potential friction between the mechanical parts of the U-tail.

Finally, the maximum elevator deflection angle was set at $\pm\,20°$. According to Sadraey [10], a larger value than this could lead to a loss of elevator efficiency due to flow separation. Therefore, the maximum value of this angle was selected in order to guarantee sufficient longitudinal control. As for the maximum deflection angle of the rudder, it was fixed at $\pm\,30°$ because it corresponds to a typical value.

6.4 Propulsion systems

6.4.1 Boundary layer ingestion (BLI)

BLI concept and motivation

Over the past few years, more and more strict measures have been implemented to reduce the emission of pollutants such as CO_2 and NO_x into the atmosphere [15]. In particular, these measures concern the air traffic. Consequently, it is urgent for solutions to be found to reduce the fuel consumption of the aircraft.

In particular, this can be achieved through the use of Boundary Layer Ingestion (BLI). BLI refers to a method that aims to reduce the power consumption of an aircraft. This results subsequently in a reduction of the fuel consumption. The basic principle is that the engine must ingest an airflow with the lowest velocity possible. More precisely, the idea is to ingest the low-speed boundary layer airflow downstream of the fuselage before it reaches its rear and is lost in the wake of the aircraft. This translates into a reduction of the propulsion power required for a given thrust.

Budziszewski and Friedrichs [15] stipulate that two categories of BLI exist, the full annular BLI (BLI_{FA}) and the asymmetric BLI (BLI_{Asym}). These configurations are depicted in Figure 6.4. As it can be seen, the BeLI can be assimilated to the asymmetric category. It corresponds to a top mounted engine at the rear of the aircraft in an associated blended-body to ingest properly the boundary layer airflow. Such a choice was made mainly because of structural reasons. Putting an engine at the rear of an aircraft with its centerline aligned with the longitudinal axis of the aircraft seems more challenging and could lead to an increased manufacturing cost. In addition, with this latter configuration, the stability of the aircraft would potentially be negatively impacted with the weight of the engine more off-centered. And given the nature of the missions that the BeLI must perform the chosen configuration appears to be a good option.

Aerodynamic benefits from BLI

As previously mentioned, BLI aims at reducing the power consumption of an aircraft. In literature, different values for the power saving coefficient (PSC) can be found. This parameter is defined as the difference between the propulsive power of a thruster without BLI compared to the one with BLI in order to produce the same given thrust.
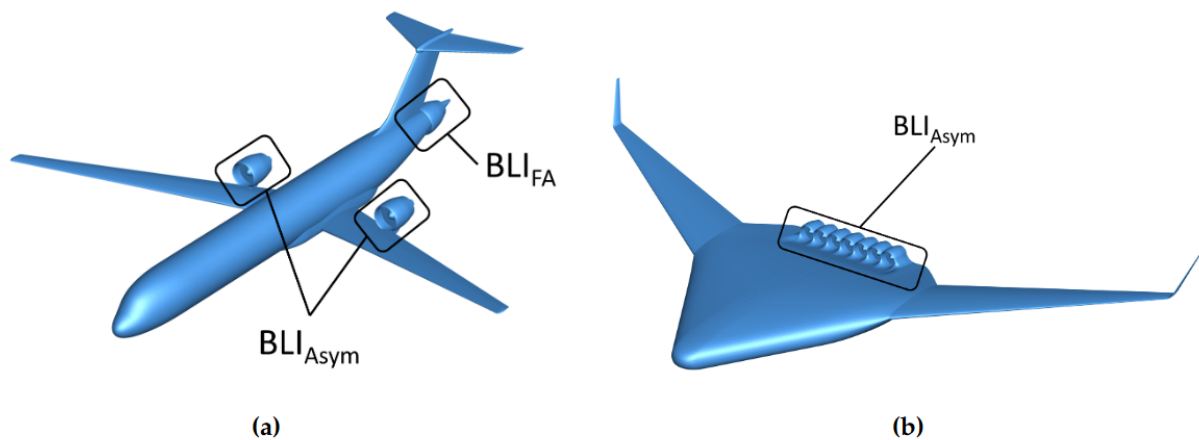
Figure 6.4: Examples of the two categories of BLI; (a) represents the full annular BLI (BLI_{FA}) while (b) represents the asymmetric BLI (BLI_{Asym}) [15].

According to Budziszewski and Friedrichs [15], studies conducted on the Aurora D8 in 2012 (*i.e.*, asymmetric BLI) have shown that a PSC of up to 5.66% can be achieved. However, the authors also stated that more recent studies have reached an even greater PSC of 8.6%. It is worth noting that such findings are confirmed in three separate studies. In a paper of 2017, [16], the authors were able to obtain a value of 8.6% but two other studies [17] [18] suggest that a PSC of 9% could be achieved under certain conditions.

On the other hand, Kaminski and Kinzel [19], achieved a PSC of 12.9% by optimizing the propulsion system in such a way that it becomes as efficient as possible. However, this result was found for an engine located at the rear of the aircraft (*i.e.*, full annular BLI). For the same category of BLI, Yildirim *et al.* [20] were able to achieve a PSC ranging from 10.8 to 12.9%. These values are dependent on the fan pressure ratio of the engine.

As it can be observed, PCS is a highly variable parameter. As a consequence, a probabilistic approach was followed to determine this parameter in the case of the BeLI. From the literature review, mean and standard deviation values can be derived and are respectively of $\mu = 9.52\%$ and $\sigma = 2.18\%$. It should be noted that this decrease in required power is implemented in the form of a reduction of the BeLI's drag to compute the BLI-enhanced performance. More details are provided in Section 7.4.

BLI efficiency parameters

As one would expect, many parameters influence the efficiency of the BLI. Budziszewski and Friedrichs [15] but also Tillman *et al.* [21] discuss the importance of the engine size. More precisely, it is the inlet aspect ratio of the engine (ratio between inlet width and inlet height) that appears to be a critical parameter. In other words, the more the engine size decreases, the more the PSC decreases for a given thrust. The authors explain this phenomenon by the fact that, for a given thrust, the exit speed must be greater for a smaller engine. Another possible explanation stated by the authors comes from the fact that the ingested boundary layer would be smaller for a smaller engine.

Budziszewski and Friedrichs [15] also suggest that altitude is a parameter influencing negatively the PSC. In other words, as the altitude increases, the PSC decreases. According to the authors, this could lie in the fact that for a given thrust, a higher exit velocity is necessary to balance the decrease of air density. However, since drag is lower at high altitudes, this negative effect could be partially balanced.

6.4.2 Engine

The propulsion system of the BeLI must allow it to reach its expected cruise Mach number and maximum Mach number respectively of 0.86 and 0.9. It must also be able to overcome the drag in the cruise of $D = 717$ lbf given in Section 7.2.3. Figure 6.5 and Figure 6.6 present different options of engine types depending on the required Mach number, the propulsion system speed limit, and the associated specific fuel consumption SFC [9].
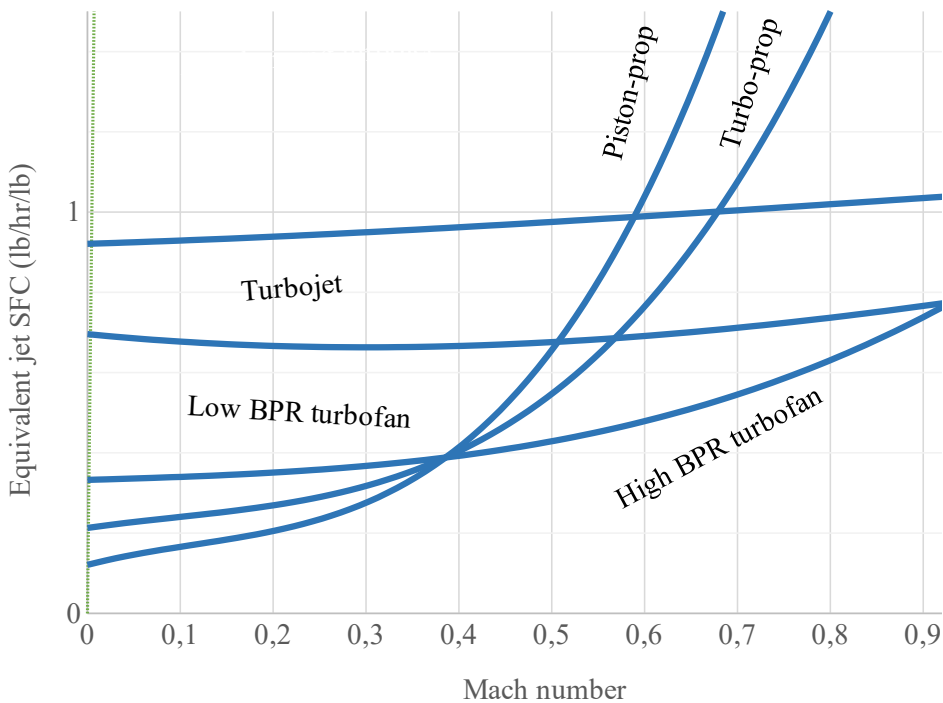
Figure 6.5: Specific fuel consumption trends at typical cruise altitudes for different propulsion systems, data retrieved from [9].

Turbofan engines are thus chosen because of their capability to reach transonic speeds and furthermore for their lowest SFC at this range of speed.

Regarding the possibility to make use of alternate energy, the use of batteries is discouraged by the long-range and the spirit of reducing as much as possible fuel consumption. Batteries are indeed essentially interesting for short flights and would just soon present dead weights for the aircraft, impacting its performance. The only option for "renewable energy" would lie in the use of biofuels as long as the performance of the engine does not change.

The propulsion systems selection is first based on an analysis of small turbofan engines for business jets currently used in the market [22]. Such types of airplanes present indeed the nearest cruise speed and range of the mission of the BeLI.
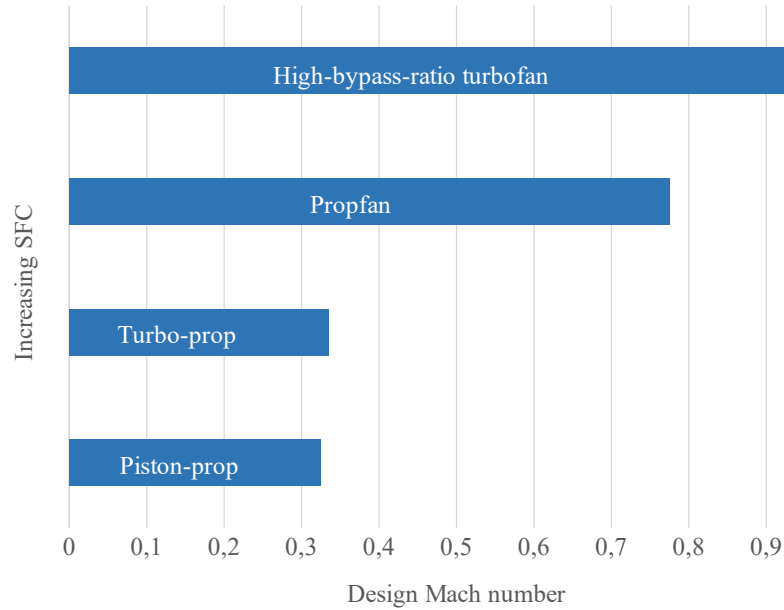
Figure 6.6: Propulsion system speed limits, data retrieved from [9].

Since the engine thrust specific fuel consumption is essentially given for take-off only or at different cruise altitude and Mach number [23] than the BeLI, Equation 6.13 allows to correct its value [24] [25]:

$$TSFC = TSFC_0 \cdot \sqrt{\theta}(1+M)^n \ ,$$

(6.13)

with θ the ratio of temperature between the cruise altitude and the sea level, $TSFC_0$ the take-off thrust, and $n = 0.8$ a statistical parameter to fit with the experimental results.

Table 6.5 compares those different engines in terms of thrust-specific fuel consumption, thrust in cruise, and at take-off. Their dimensions are also investigated.

Table 6.5: Comparison of suitable small engines regarding thrust, TSFC, and geometry.

Engine	JT15D	PW 530	PW 535A	PW 545C	TF37GE − 1
Take-off thrust [lbf]	3045	2887	3400	4119	3750
Cruise thrust [lbf]	784	656	848	892	981
Cruise TSFC [lb/hr/lbf]	0.868	0.682	0.682	0.682	0.652
Bypass ratio [-]	3.3	3.7	2.55	4.12	1.9
Length [in]	39.4	60	63.9	68.6	39.4
Diameter [in]	27.2	23	28.2	27.3	35.8
Weight [lb]	632	765	765	765	675

The TF37-GE-1 military engine is chosen for its lower values of TSFC and weight, both parameters being of crucial importance in the maximization of the range of the BeLI. Military engines are known for their high specific thrust

which leads to a compact and light engine. The secondary airflow of the TF37-GE-1 also allows to increase its efficiency with respect to a similar turbojet engine and thus presents itself as the best compromise for the engine of the BeLI.

It must be noted that the specified thrust in the aforementioned table is the uninstalled one. A reduction of around $4-8\%$ must thus be accounted for in the following computations to obtain the installed thrust [8] [9].

It is verified that the engine chosen is sufficiently powerful as the ratio of the maximum thrust and drag in cruise is

$$\frac{T}{D} = 79\%. \tag{6.14}$$

Hence, the TF37-GE-1 power enables us to perform maneuvers and provides the 24 kW of available cruise electrical power as requested in the KPPs.

6.5   Fuselage

As a first approximation of the length, the design was taken from a jet transport and a statistical relation from Raymer [9] provided a length of 29 ft. The width was chosen to achieve a good fineness ratio while keeping enough place for the engine, subsystems, and mission payload.

The internal disposition is shown in Figure 6.7. The BeLI is seen to occupy the space available efficiently.

6.6   Landing gear

The landing gear acts as the support on the ground of the aircraft and provides its braking. Hence, it must carry the static weight of the aircraft and the dynamic force encountered during braking.

A tricycle configuration is chosen because it ensures good stability on the ground, at take-off, and at landing according to Raymer [9]. Due to the high speed and the long-range required, the landing gear is also chosen retractable to reduce the drag. The schematic of the landing gear layout is provided in Figure 6.8 and in Figure 6.9.

In addition to a static load that can be easily determined from Figure 6.8 as

$$F_{NG}(x_{cg} - x_{NG}) = F_{MG}(x_{MG} - x_{cg}) \ , \tag{6.15}$$

the nose gear also needs to support a dynamic force during braking.

Due to the braking force applied by the main gear on the ground, it creates a moment that will be supported by the nose gear as shown in Figure 6.10.

The equation of moment gives

$$F_{NG}(x_{cg} - x_{NG}) = F_{MG}(x_{MG} - x_{cg}) + F_b h_{cg} + F_r \delta \ . \tag{6.16}$$
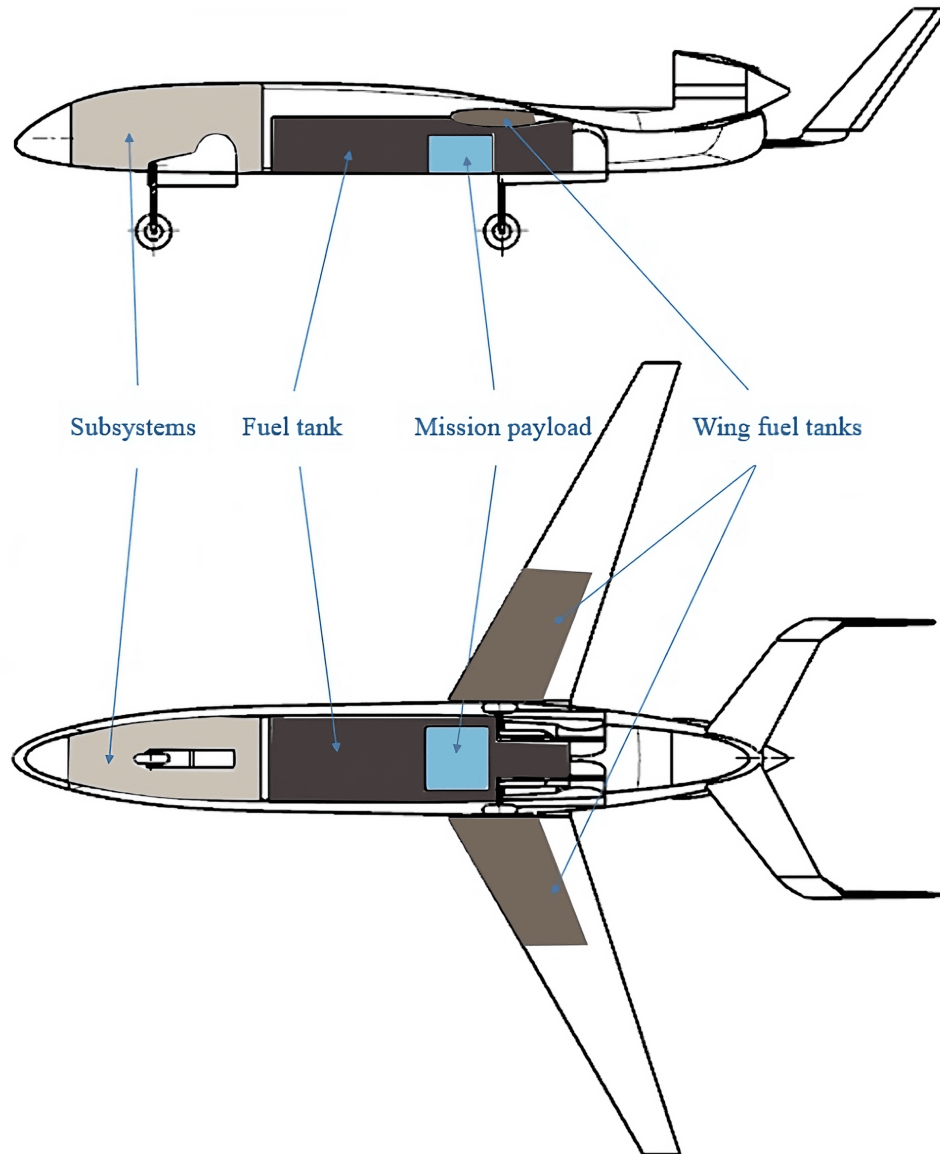
Figure 6.7: Internal configuration of the components

Coupled with the dynamic equation of forces equilibrium, $F_{NG} + F_{MG} = W - L$, and the relation $x_{cg} - x_{NG} = l_{wb} - (x_{MG} - x_{cg})$, F_{NG} can finally be calculated as

$$F_{NG} = (W - L)\frac{(x_{MG} - x_{cg})}{l_{wb}} + F_b\frac{h_{cg}}{l_{wb}} + F_r\frac{\delta}{l_{wb}} \quad . \tag{6.17}$$
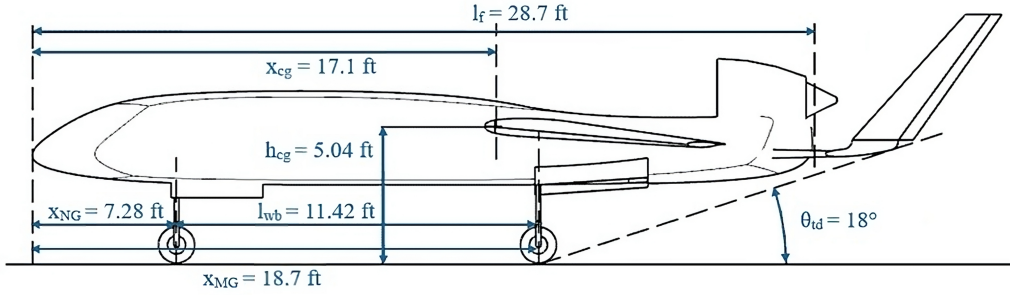
Figure 6.8: Layout of the landing gear from a profile view.
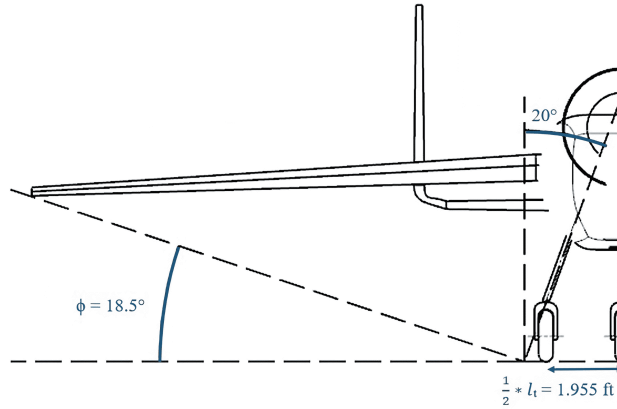
Figure 6.9: Layout of the landing gear from a front view.

For a given constant deceleration $a = \dfrac{F_b + F_r}{m}$, the worst case is encountered when $L = 0$ and $F_r = 0$:

$$F_{NG} = \frac{W}{l_{wb}}\left((x_{MG} - x_{cg}) + \frac{a}{g}h_{cg} \right) \; . \tag{6.18}$$

F_{NG} can be reduced by placing the main gear as close to the CG as possible (limited by the static stability) or by reducing the height of the aircraft (limited by the pitch angle θ_{td}).

The maximum pitch angle θ_{td} and roll angle ϕ respectively illustrated in Figure 6.8 and Figure 6.9 are indicators of the maximum deviation allowed on landing. P. Sforza [26] gives typical values for θ_{td} and $\phi°$, respectively 15° and 10°. The BeLI is supposed to land in poor conditions, so the angles must be larger to increase the acceptable landing errors. The mechanical constraints for the retraction, the height required, caused the two angles to be 18°.

The load per wheel W_w is defined as the total weight divided by the number of wheels. A trade-off has to be made between the amount and the size of the wheels. The main gear has to carry a static load of 5650 lbs, so the best gear is a two wheels configuration where each wheel must carry 2825 lbs. The type of wheel chosen is the Type VII for high landing speed. The wheel corresponding in the data [27] is 16x4.4 inches with a ply rating of 10 (quality factor). The nose gear has to carry a static load of 997 lbs and a dynamic load of 1978 lbs. The optimal wheel is 16x4.4 inches with a ply rating of 6.
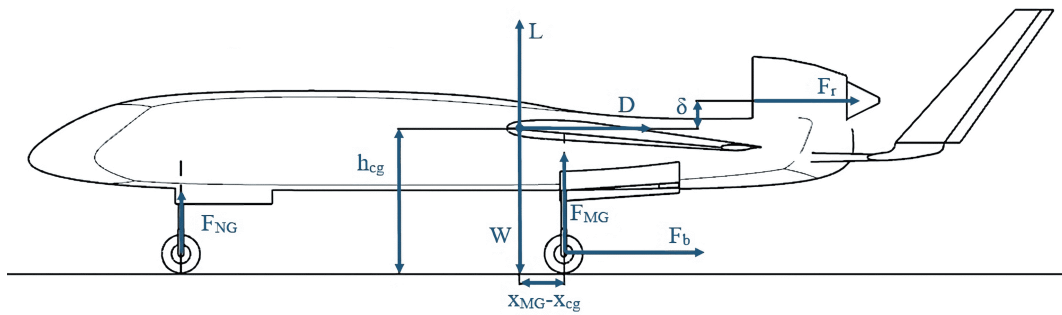
Figure 6.10: Forces acting on the landing gears.

The main landing gear has to support a landing at a vertical descent velocity $v_v = 15$ fps and maximum landing weight W_{MLW}. It means that the wheel's maximum bottoming load must be greater than the vertical force applied on the plane during the shock.

$$F \geq \frac{W_{MLW} \cdot v_v}{2h} \; ,$$ (6.19)

with h the length of the shock absorption.

The length h for this wheel is 1.45 ft. Since this value is lower than the length of the struts which are 2.31 ft long, the requirement is respected.

6.7 Payload

6.7.1 Release system

The BeLI mission's goal is to deliver supplies for the victims. Hence, an airdrop system must be designed. The drop will occur at the loiter speed, which means at Mach 0.7. Therefore, the system must be adapted to a high-speed airdrop. The accuracy of the drop must also be taken into account since the supplies must land close to the victims' location to ensure fast distribution. On the other hand, dropping the supplies too close to the victims could eventually lead to accidents.

For this mission, the Joint Precision Airdrop System (JPAS) is chosen. This system provides aircraft with precision airdrop capabilities. This ensures accurate supply delivery, allowing aircraft to drop from high altitudes but also at high speed. Based on a GPS, the active control of the cargo parachute compensates the wind disturbances based on the weather forecast and guides the cargo towards the designed target [28].

AGAS 2000 is one of those systems using commercial and relatively inexpensive autopilot and mission planners. This system has already demonstrated full compatibility with the US Air Force Precision Airdrop System (PADS), which integrates a parachute decelerator and an autonomous guidance unit [29]. The mission profile of the AGAS 2000 is shown in Figure 6.11:
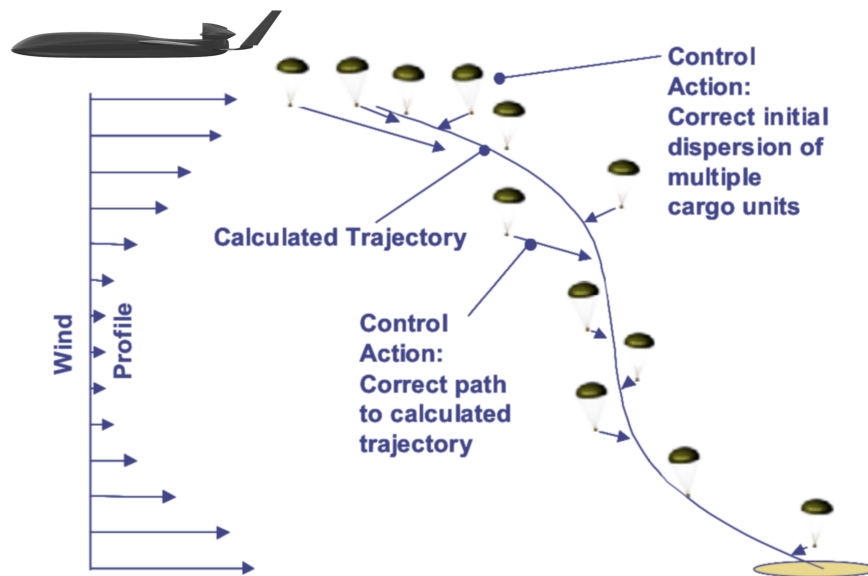
Figure 6.11: AGAS 2000 mission profile [28].

Additionally, to the relatively low price of the AGAS 2000 system, the PADS computer integrated into the aircraft weights only 1.77 lbs [28].

In terms of performance, fourteen tests were conducted using 12 h old wind forecast. Out of the fourteen test missions, a 692 ft Circular Error Probable (CEP) was estimated. After that, 25 test missions were conducted using the current wind forecast. An improved CEP of 124 ft was estimated [28]. This last performance is considered representative of the performance that the AGAS 2000 system is expected to achieve.

6.7.2 Mission payload

The number of people to be rescued has been left free. However, the mission requirements specify that the allowed mission payload must be at least 300 lbs to reach the objective. The requirements also specify that the rescued people are up to two at the same place. The payload is thus divided is several smaller boxes, each of them equipped with a parachute with the Drop Delivery System (DDS).

One box contains the survival materials for two people, allowing flexibility in the use of the box and potentially saving a higher overall amount of people. The box therefore contains:

- water;

- a satellite communication radio;

- a first aid kit;

- the parachute (equipped with the DDS).

A schematic is shown in Figure 6.12.
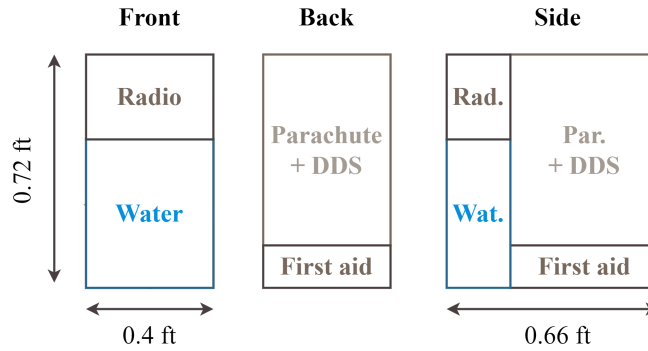
Figure 6.12: Composition of a box.

The quantity of water per person can be calculated from requirements, considering that victims are in immediate need of drinking and must survive for at least 6 hours until help arrives. According to the Centers for Disease Control and Prevention (CDC) [30], a person needs almost 0.5 gallon of water per day in average. To only survive, this quantity can be reduced to 0.25 gallon [31]. Hence, a quantity equivalent to a bottle of 8 fluid ounces per person must be provided for the mission. If the person is alone, there will be enough water in one box to survive 12 hours, 6 hours if two people are present.

The box is also completed by a communication radio. As land-based facilities are expected to be destroyed within a 1000 nm distance around the disaster zone, the communication radio is relying on satellites. A potential communication radio which can be used is the IC-SAT100. Such a device provides worldwide coverage and has an autonomy of 14 hours [32].

Finally, a typical first aid kit is added. The kit includes all types of plasters and bandages, scissors, alcohol-free cleaning wipes, tape, gloves, distilled water, an emergency blanket, a compress, and tweezers.

An estimation of the weight and dimensions of the mission payload is shown in Table 6.6.

Table 6.6: Summary of mission payload composition.

	Weight [lbs]	Dimensions [ft] (H x W x L)
First aid kit	1.76	0.13 x 0.4 x 0.45
Radios (2 units)	1.98	0.26 x 0.4 x 0.2
Water (2 bottles)	1.10	0.46 x 0.4 x 0.2
Parachute & DDS	5.00	0.59 x 0.4 x 0.45
Total (one box)	9.85	0.72 x 0.4 x 0.66
Total (36 boxes)	355	2.16 x 2.4 x 1.32

The computation was based on analogous solutions design. The mission payload available space permits to carry a quantity of 36 boxes. Therefore, the potential number of victims which can be rescued for one mission varies from 36 to 72 people.

The payload composition can vary depending on the type of disaster for which the BeLI is operating. For flood or disasters occurring in the ocean, it might be relevant to provide life jackets to victims. In case of fire, the payload could also be adjusted to provide more water to victims and a fire mask.

6.8   Materials selection

Material selection is a critical point in the design of aircraft components, as it strongly influences their performance and cost. It is indeed necessary to choose a material that guarantees the physical integrity of the structure by withstanding the various loads that are applied to it while being sufficiently light to minimize the power needed to fly. In addition, since the different parts of the aircraft are characterized by different requirements, different materials must be selected. For the BeLI, two materials are retained. One for the landing gear and the other for the remaining components such as the wing, tail, and fuselage.

6.8.1   Main components

A selection process must be performed for the wing, tail and fuselage of the aircraft because the physical integrity and performance of these components is essential to ensure the success of the mission. This selection is even more important since the structure of the BeLI must be able to sustain small shocks as the aircraft approaches sonic conditions in some cases.

For this reason, a study with the Granta Edupack software [33] was conducted. The objective of this analysis was to find a material with the highest strength-to-weight ratio, the lowest possible cost and a high fatigue resistance. Also, a material characterized by high fracture toughness must be selected to avoid the rapid propagation of any cracks and consequently, sudden failure of the structure.

The results of this study show that 7075 T6 aluminum alloy is the most suitable to meet the previously mentioned criteria. Its main mechanical properties are presented in Table 6.7. It should also be noted that this material is widely used in the aerospace industry. In addition, aluminum is one of the most recycled materials in the world. Therefore, once the BeLI has completed the required number of flights, the material composing its fuselage, wing, and tail can be recycled to significantly reduce the cost of producing new aluminum products. This constitutes another advantage to selecting this material. Finally, it is worth noting that composites were not regarded in this analysis. This choice is explained by the fact that this type of material is generally more expensive than an aluminum alloy for a given mass. This characteristic had to be taken into account as the BeLI is expected to perform very few flights, making cost a driving concern. In addition, it is proven in Section 7.3 that the choice of the Al 7075 T6 alloy is sufficient to resist the different loads during the flight.

Table 6.7: Mechanical properties of 7075 T6 Al alloy [33].

Property	Value
Density ρ	0.102 lb/in^3
Elasticity modulus E	10400 ksi
Tensile strength σ_f^0	83 ksi
Yield strength σ_y^0	73 ksi
Shear strength $\tau_{strength}$	48 ksi

6.8.2 Landing gear

The material selection for the landing gear is crucial since this component must be able to support the weight of the aircraft on the ground but also to resist the stresses and strains undergone during take-off or landing. For this reason, a material characterized by high yield strength and high maximum acceptable stress must be selected. Also, a material with high toughness and ductility should be considered in order to ensure good resistance to shocks. Moreover, a low density should be looked for to ensure good overall performance of the aircraft. Finally, a cost-effective material must be chosen. This last criterion is particularly important since the number of flights that the BeLI must accomplish is very low compared to other aircraft of the same type.

The selection process was conducted using the Granta Edupack software [33] to select the most suitable material for all the previously mentioned criteria. The results of this study show that AISI 4340 alloy steel is the most appropriate one for the landing gear. It should be noted that this alloy is commonly used for this kind of application in the aerospace industry. Its main mechanical properties are presented in Table 6.8.

Table 6.8: Mechanical properties of AISI 4340 steel alloy [33].

Property	Value
Density ρ	0.284 lb/in^3
Elasticity modulus E	30458 ksi
Tensile Strength σ_f^0	180 ksi
Yield Strength σ_y^0	150 ksi
Shear strength $\tau_{strength}$	63 ksi

6.9   Weights and center of gravity computation

Some of the aircraft geometric parameters are complicated to determine. The airplane is indeed composed of solid materials and liquid (fuel) and the geometric configuration (wing and tail position, fuel tanks, and payload distribution) varies from one aircraft to another. In this section, in order to determine important parameters of the BeLI such as its Center of Gravity (CG), the airplane is divided componentwise for the sake of simplicity.

6.9.1 Weights computation

Fuselage and landing gears

The fuselage weight can be approximated by a statistical method provided by Raymer [9]

$$W_{fuselage} = 0.3280 \cdot K_{door} \cdot K_{Lg} \cdot (W_{dg} N_z)^{0.5} \cdot L^{0.25} \cdot S_f^{0.302} \cdot (1 + K_{ws})^{0.04} \cdot (L/D)^{0.10} \tag{6.20}$$

with $K_{door} = 1$ (no door), $K_{Lg} = 1.12$ (fuselage-mounted landing gear), $W_{dg} = 0.55 \cdot W_{fuel}$, $N_z =$ the ultimate load factor (see Section 7.3), the fuselage length L, the fuselage wetted area S_f, the wing sweep factor K_{ws} and finally the fuselage structural depth D. In the end, $W_{fuselage} = 835$ lbs.

The landing gear weight is linked to the zero-fuel weight by the empirical relation given by P. Sforza [26] as $\frac{W_{LG}}{ZFW} = 0.043$ and thus $W_{LG} = 130$ lbs.

Wing

In order to determine the weight of the wing, empirical correlations were used [8]. It should be noted that these relationships use geometric parameters of the wing such as span, area, sweep angle, taper ratio, and chord. In addition, the maximum load factor that the aircraft must be able to support was taken into account. Finally, the maximum ratio between the chord and the airfoil thickness was considered to perform the calculations. The latter being 14%, as stated in Section 6.2.2.

The resulting weight of the wing is 397 lb. It should be noted that this weight is assumed to allow the aircraft to withstand the various shocks and loads encountered during flight.

Empennage

As it was the case for the wing, empirical correlations were used to calculate the weight of both horizontal and vertical tails. These relationships can be found in [8]. More precisely, it should be noted that these equations use the geometrical parameters of the tail such as the span, surface, sweep angle, and chord. In addition, the maximum load factor was taken into account once again. Finally, the maximum ratio between the chord and the empennage airfoil thicknesses was considered to perform the calculations. Such a value was fixed at 12%, as explained in Section 6.3.3.

The resulting weights are 121 lb for the horizontal tail and 75 lb for the fin. Such values seem to be consistent with the dimensions of the aircraft. It seems important to recall that the horizontal tail was designed to support the additional weight due to the U-shaped configuration.

Engine

Since the TF37-GE-1 engine of the BELI is an off-the-shelf engine, its weight of 675 lb is directly retrieved from the manufacturer or aircraft database [22].

Fuel

The total fuel weight is determined by using the same process as the first weight estimation, which also provides the fuel ratio (Section 6.1).

Payload, subsystems and sensors

The weight of the subsystems and sensor is given in the requirements respectively as 222 and 228 lbs.

6.9.2 Center of gravity computation

The CG of each component can be determined based on their parameters. The methodology used here is the same as the one used in [34]. For the fuselage, its CG is located at 45% of its length. The one of a half wing is at 30% chord at wing MAC, 30% chord at 35% semi-span for the fin and tail CG. 50% of the engine length for its CG. Finally, the fuel tanks and payloads CG location depends on their geometry.

At this point, all the component CGs are determined in their own system of reference. They still have to be expressed in the system of reference of the airplane. The last parameter to know is the BELI's configuration: the position of each component. The latter is imposed on the one hand by practical constraints and, on the other hand, by stability constraints (the stability of the BELI is developed in Section 7). The engine must indeed be far enough back to benefit from the BLI effect and, in order to balance this counterweight, the fixed payloads (sensors and subsystems) are placed in the nose of the airplane. A fuel tank is present in each half-wing and the CG of these is considered to be located on that of the half-wing. The tank in the fuselage is placed in order to compensate the fuel tanks in the wing to have the overall fuel tanks CG corresponding to the BELI's CG (in x direction). Moreover, the position of the mission payload has to be in the lower part of the aircraft since it will be dropped during the mission and its CG is actually made so that it corresponds to the actual CG of the BELI in the longitudinal direction. That means that the x position of the BELI's CG will stay unchanged during all the mission if the same percentage of fuel in every fuel tank is kept and this is done using pumps. Also, the wing and tail position will govern the stability of the BELI.

With both weight and CG of every component known, the aircraft's CG can be determined. All the CGs of the components, as well as the CG of the BELI are represented in Figure 6.13. Once again, the geometry is simplified in order to ease visualization. In Figure 6.13, the BELI's CG for the MTOW case is represented by the red dot.
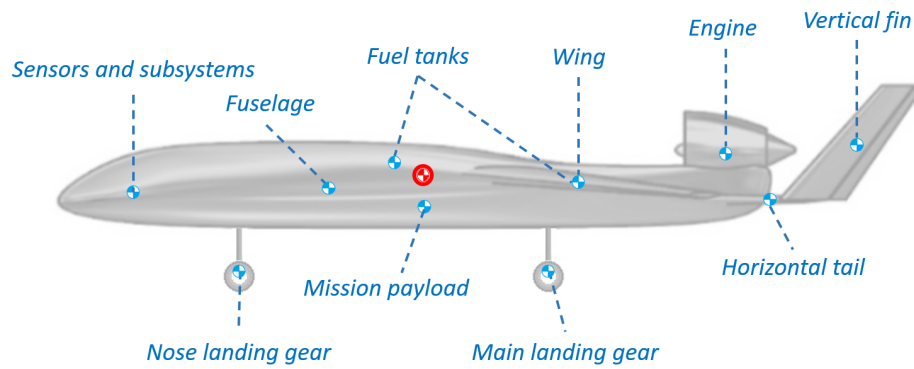
Figure 6.13: Representation of each component CG (blue dots) and the BeLI CG (red dot).

All components weight and CG coordinates are listed in Table 6.9 using the X-axis pointing from tail to nose, the Y-axis aligned with the wing span and symmetric, and the Z-axis pointing up. The origin of this base corresponds to the center of the fuselage at the BeLI's tail. The coordinates of the aircraft CG for MTOW case are given in Table 6.9. These will be important for the stability determination in Section 7.

Table 6.9: Summary of the CG position of each component, the BeLI CG position, the weight of each component, the MTOW, the ZFW, the OEW and the fuel ratio of the BeLI.

Component	Weight [lb]	CG (X-axis) [ft]	CG (Y-axis) [ft]	CG (Z-axis) [ft]
Fuselage	835	15.7	0	0
Main landing gear	87	10	0	-4.67
Nose landing gear	43	21.42	0	-4.67
Half-wing	199	7.95	$\pm$ 6.59	0.51
Half-fin	38	-2.45	$\pm$ 6.56	1.11
Half-tail	60	0.85	$\pm$ 3.63	-0.51
Engine	675	2.23	0	1.48
Fuselage fuel	2895	12.47	0	0.97
Wing fuel	741	7.95	0	0.51
Payload mission	355	11.55	0	-0.67
Subsystems and sensors	447	25.61	0	-0.11
BeLI (MTOW)	6670	11.55	0	0.53
BeLI (ZFW)	3035	11.55	0	0.11
BeLI (OEW)	2680	11.55	0	0.21

The Maximum Take Off Weight (MTOW) is the sum of all the component weights. This means that this MTOW is the real weight of the BeLI and no longer an approximation. The Zero Fuel Weight (ZFW) is the MTOW without all the fuel weight and the Operational Empty Weight (OEW) is the ZFW without the mission payload weight. The BeLI's fuel ratio is 55%.

7 Aircraft analysis

7.1 Stability

Stability deals with the ability to keep an aircraft in the air in the chosen attitude. Stability is not considered as a design criterion; it is a concept that needs to be assessed after having designed the aircraft for certain performance. Two types of stability are assessed in this section: static and dynamic. Together, they allow the aircraft to maintain uniform flight conditions, recover from disturbances and minimize pilot workload.

7.1.1 Static stability

Static stability can be divided into longitudinal and directional stability. Static stability implies that all the forces and moments around the center of gravity (CG) at a fixed flight condition and attitude are balanced. Moreover, after any small perturbation in flight attitude, the aircraft should return to its equilibrium position.

Longitudinal stability

The steady level flight is assumed, meaning that the thrust balances the drag and they both pass by the CG. The aircraft is said to be statically stable if the pitching moment in the flight conditions is zero and if the first derivative of this moment with respect to the lift is negative. The static margin K_n can thus be introduced as an evaluation of the latter derivative. The static margin is defined as the distance between the center of gravity of the aircraft and the neutral point normalized by the mean aerodynamic chord:

$$K_n = -\frac{\partial C_m}{\partial C_{Lw}} = h_n - h \ .$$ (7.1)

The center of gravity is found in Section 6.9. The neutral point, equivalent to the aerodynamic center of the entire aircraft, is found by taking into account the contribution of the fuselage, the wing, and the tail [34].

Using this definition, a positive value for the static margin corresponds to a stable configuration. Lower values indicate that the aircraft is very maneuverable while higher values indicate a rather stable aircraft. According to the Federal Aviation Administration [3], it must be ensured that at any moment of the flight, K_n must have a value between 5% and 20%. This enables enough maneuverability while being sufficiently stable. To enforce this criterion, the margin has been computed for two different flight conditions: MTOW and ZFW. The first case is inevitably encountered while the second one is an "emergency" case. The associated centers of gravity were defined in Section 6.9 and are located at the same position along the fuselage. This means that the static margin is the same for both configurations and is equal to 10%. The CG, the neutral point, and the static margin range is represented in Figure 7.1. The static margin range represents the minimal and maximal value that the CG can take while respecting the FAA requirement aforementioned.
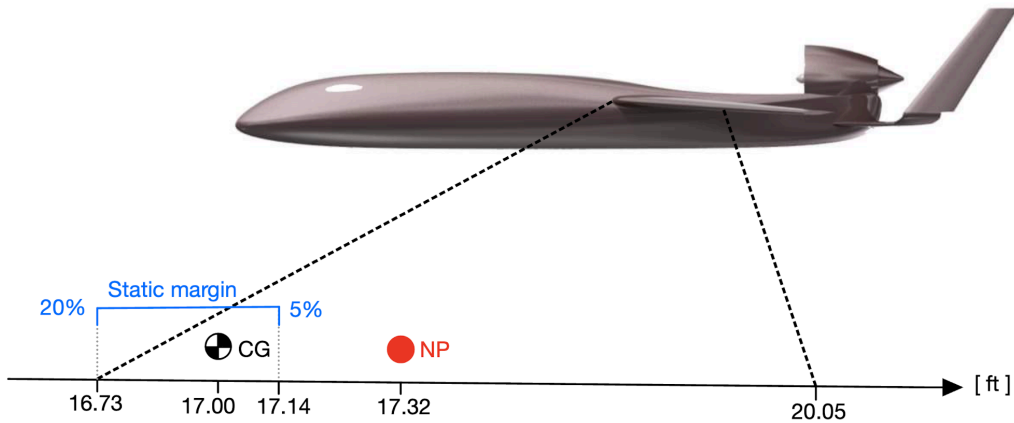
Figure 7.1: Static margin range, neutral point, and center of gravity along the longitudinal direction.

The distances are measured from the nose of the aircraft.

The margin of 10% indicates that there is a good trade-off between maneuverability and stability. However, the CG will move during the flight while fuel is burned. That is why the fuel tanks are equipped with a fuel pump. By emptying the tanks from the fuselage and the wing simultaneously, one can ensure that the CG will stay close to the same location along the fuselage during the whole flight (with a [+10%; -5%] margin in stability). An additional pump is included for redundancy.

Lateral stability

Lateral stability is the tendency of the aircraft to return to its original direction with respect to the freestream after a sideslip perturbation. This criterion is less severe than the longitudinal stability one. The derivative of the yaw coefficient C_N with respect to the sideslip angle β must be computed [34]. This takes the effect of the fuselage, the fin, and the wing into account. In high-mounted wing configuration, the only stabilizing moment against a sideslip perturbation comes from the fin contribution [14].

The requirement is:

$$C_{N\beta} = \frac{\partial C_N}{\partial \beta} > 0 \, , \tag{7.2}$$

with

$$C_{N\beta} = C_{N\beta,w} + C_{N\beta,fus} + C_{N\beta,fin} \, . \tag{7.3}$$

In the latter equation, $C_{N\beta,w}$ = -0.017 (destabilizing effect of the high-mounted wing), $C_{N\beta,fus}$ = -0.007 (destabilizing effect of the fuselage) and $C_{N\beta,fin}$ = 0.096 (highly stabilizing effect of the fin). In the end, $\dfrac{\partial C_N}{\partial \beta}$ is equal to 0.073.

7.1.2 Dynamic stability

Once the static stability has been assessed, the dynamic stability has to be determined. Aircraft flight is indeed a dynamic phenomenon. Any control input or external excitation results in a dynamic response that can be oscillatory. That response needs to be damped in order to be dynamically stable. To model the response, the full linearized equations of motion of the aircraft must be derived. These can be written in a state-space formulation as:

$$\dot{\mathbf{x}} = \mathbf{A}\mathbf{x} + \mathbf{B}\mathbf{u} \quad , \tag{7.4}$$

where $\mathbf{x} = [u\,v\,w\,p\,q\,r\,\phi\,\theta\,\psi]^T$ is the vector containing the state variables, velocity perturbations, and angular perturbations. The system which is considered here is the aircraft with the origin of the axes at the CG. The vector $\mathbf{u} = [\xi\,\eta\,\zeta\,\tau]^T$ contains the system input, namely, the deflection of the primary control surfaces (ailerons, elevator, and rudder) and the thrust perturbation with respect to the trim positions. The matrix $\mathbf{A}$ contains the stability derivatives and the moments of inertia. The matrix $\mathbf{B}$ contains the control derivatives. The stability derivatives are computed using the USAF DATCOM [35]. This compendium includes empirical correlations which can be used to estimate the stability and control derivatives of conventional subsonic airplanes.

As it was done for the static stability, the pitch stability can often be decoupled from roll and yaw stability in the dynamic analysis. Once the stability derivatives are computed in cruise configuration, the eigenvalues of $\mathbf{A}$ are studied. The latter are indicators of dynamic stability and describe the different natural modes.

Table 7.1 and Table 7.2 provide a summary of these stability derivatives. The eigenvalues associated with both systems are gathered in Table 7.3. If each of those values has a negative real part, the system is dynamically stable. In the case of the BeLI, the only positive real part corresponds to the spiral mode which will be discussed later.

Table 7.3: Eigenvalues of $\mathbf{A}$ for longitudinal and lateral modes.

Longitudinal eigenvalues	Lateral eigenvalues
-2.767 + 2.929i	-10.895 + 0.000i
-2.767 - 2.929i	-0.044 + 3.029i
-0.004 + 0.180i	-0.044 - 3.029i
-0.004 - 0.180i	0.007 + 0.000i

Longitudinal modes

An aircraft can undergo two kinds of longitudinal modes of vibration: the *phugoid* mode and the *short period oscillations*. They are defined by a frequency (or pulsation in [rad/s]) and a damping ratio. They are represented

Table 7.1: Longitudinal stability derivatives (USAF DATCOM).

Derivative	Datcom value
$C_{L\alpha}$	6.165
$C_{D\alpha}$	0.108
$C_{M\alpha}$	-0.340
C_{Lu}	0.700
C_{Du}	0.030
C_{Mu}	0.308
C_{Lq}	4.013
C_{Dq}	0
C_{Mq}	-21.065
$C_{L\dot{\alpha}}$	-21.251
$C_{D\dot{\alpha}}$	0
$C_{M\dot{\alpha}}$	-9.340

Table 7.2: Lateral stability derivatives (USAF DATCOM).

Derivative	Datcom value
Y_v	-1.322
Y_p	-0.146
Y_r	0.146
L_v	-0.098
L_p	-0.685
L_r	0.154
N_v	0.050
N_p	0.034
N_r	-0.178

in Table 7.4. For the cruise configuration, the frequency and damping ratio indicate the level of flying qualities. A level 1 indicates that the flying qualities are clearly adequate for the cruise phase. A level 3 means degraded flying qualities but with more pilot workload, the aircraft can still be controlled [36]. Phugoids have a much larger period than short-period oscillations. The phugoids have in this case relatively low damping ($\zeta_{phugoid} > 0.04$ for level 1 of flying qualities, level 2 for the BeLI) but, because it is very slow, those kinds of vibrations can be neutralized by re-trimming the aircraft. The damping ratio of the short period oscillations correspond to a level 1 ($0.3 < \zeta_{shortperiod} < 2$). Upper and lower values for phugoid and short period oscillation frequencies are not quantified. However, it is recommended that they are well separated ($\omega_{phugoid}/\omega_{shortperiod} > 0.1$). This ratio is about 22 for the BeLI.

Table 7.4: Natural frequencies and damping ratios of the longitudinal modes.

Mode	Frequency ω [rad/s]	Damping ratio ζ [-]
Short period oscillations	4.029	0.687
Phugoid	0.180	0.021

Lateral modes

There exist three kinds of lateral modes: the *spiral* and *roll subsidence* which are non-oscillatory modes and the *dutch roll* mode, which is oscillatory. The dutch roll has a relatively low damping ratio ($\zeta_{dutchroll} > 0.02$ for level 2, level 3 for the BeLI) which could potentially be increased by using a yaw-damper [10]. The roll subsidence mode

has a frequency corresponding to a level 1. The spiral mode is unstable. It is the case of many aircraft, even civil ones. However, this does not present any problem because of its large time constant (corresponds to level 1). The spiral movement can be stopped by a corrective control input. These results are shown in Table 7.5.

Table 7.5: Natural frequencies, damping ratios, and time constants of the lateral modes.

Mode	Frequency ω [rad/s]	Damping ratio ζ [-]	Time constant τ [s]
Spiral	0.007	1	-143.670
Dutch roll	3.029	0.015	-
Roll subsidence	10.895	1	0.092

7.2 Aerodynamics

During the conceptual design stage of the BeLI, the aerodynamics has been computed based on empirical correlations. The purpose of this section is to verify and improve these previous empirical results.

On one hand, the numerical model is performed by DARTFLO[2], for Discrete Adjoint for Rapid Transonic Flows, which is an open-source C++/python full potential solver using finite elements[3]. This solver has been developed by Adrien Crovato at the University of Liège [37]. Although DARTFLO can be used over the whole aircraft, the study is limited to the wing, which is the main lifting body of the aircraft.

On the other hand, the drag of the entire plane is studied in more detail by considering all components. This drag study is achieved by following Torenbeek [14] and Gudmundsson [12] methodology.

7.2.1 Lift analysis

The lift of the wing is analyzed for the cruise and the loiter. Even if only the speed changes, it is relevant to study these two conditions separately as the cruise is done in a transonic flow (Mach 0.86) and the loiter in a high subsonic flow (Mach 0.7).

Cruise and Loiter

It has to be noted that DARTFLO assumes an inviscid flow, so the boundary layer is not modeled. Hence, the shocks are not occurring at the same place, and the flow is different than in reality for the same angle of attack. The lift, drag and moment coefficients are therefore also different. In order to get more accurate lift results, a post process "correction" is made by changing the simulation angle of attack. In the next graphs, "corrected" and "uncorrected" results are both shown, in order to see how the correction affected the numerical results. However, this "correction" for lift leads to inaccurate drag and moment coefficients, so no post-process "correction" is made for

---

[2]https://gitlab.uliege.be/am-dept/dartflo
[3]Provided results have been subjected to a convergence study of the mesh.

them. As a perspective, to complete and validate the numerical results, the use of a viscous solver could be relevant. The comparison between numerical and empirical results for both conditions is shown hereafter in Figure 7.2. This graph highlights the fact that the empirical results of the conceptual design slightly underestimate the slope of the lift coefficient, this is due to the non-linearity and the presence of shocks in the transonic flow. Therefore, the performance and the stability derivatives are computed by using these new values from the DARTFLO solver. A summary is shown in Table 7.6.

(a) Cruise. (b) Loiter.
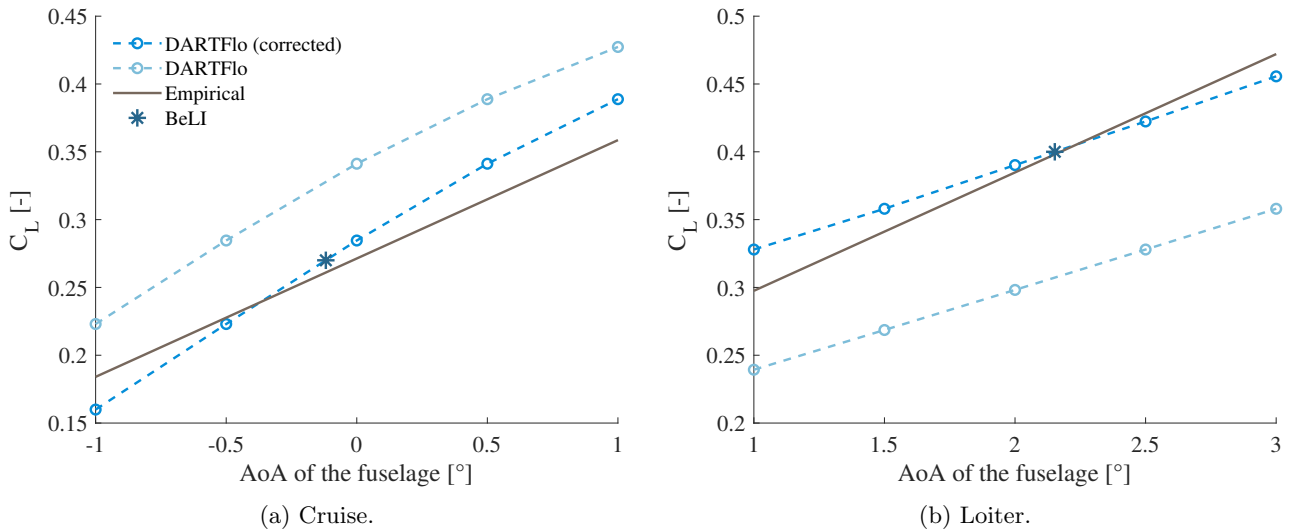
Figure 7.2: Wing lift coefficient with respect to the angle of attack of the fuselage for cruise and loiter conditions.

Table 7.6: Comparison between empirical and numerical results for lift coefficient characteristics (final values highlighted in blue).

	Cruise		Loiter	
	Emp.	DARTFLO	Emp.	DARTFLO
Lift coefficient slope [1/rad]	5	**5.93**	5	**3.43**
Zero Lift AoA [°]	-4.61	**-2.29**	-4.61	**-4.63**
Wing Lift coefficient [-]	0.27	**0.27**	0.4	**0.4**
Fuselage AoA [°]	0	**-0.12**	2.2	**2.15**

7.2.2 Aerodynamic center

The position of the aerodynamic center and its corresponding moment are estimated by using empirical relations of Torenbeek [14] and are given in Table 7.7.

Table 7.7: Aerodynamic center coordinates and moment.

MAC	X_{AC} (from nose)	Y_{AC} (from root)	c_m at AC
3.314 ft	17.835 ft	3.609 ft	-0.09

The value of the pitching moment at the aerodynamic chord is verified with DARTFLO as shown in Figure 7.3. The first estimation seems to be enough accurate and is then kept.
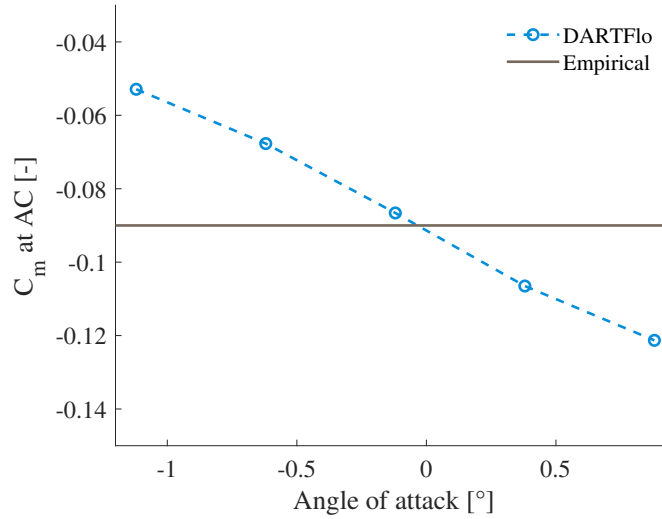
Figure 7.3: Variation of the moment coefficient at the aerodynamic center with respect to the angle of attack.

7.2.3 Drag study

In this section, the total drag of the aircraft will be computed using the component drag build-up method presented by Torenbeek [14] and Gudmundsson [12]. These two books are followed for the entire drag study. The aim of this method is to analyze the different types of drag appearing during the flight, and gather the drag coefficient for the different parts of the aircraft. Finally, by summing the lift-induced drag and the zero-lift drag (also called minimum drag), the total drag coefficient of the aircraft is obtained to compute the drag force that it undergoes during the mission. The scheme of the component drag build-up method is represented in Figure 7.4:
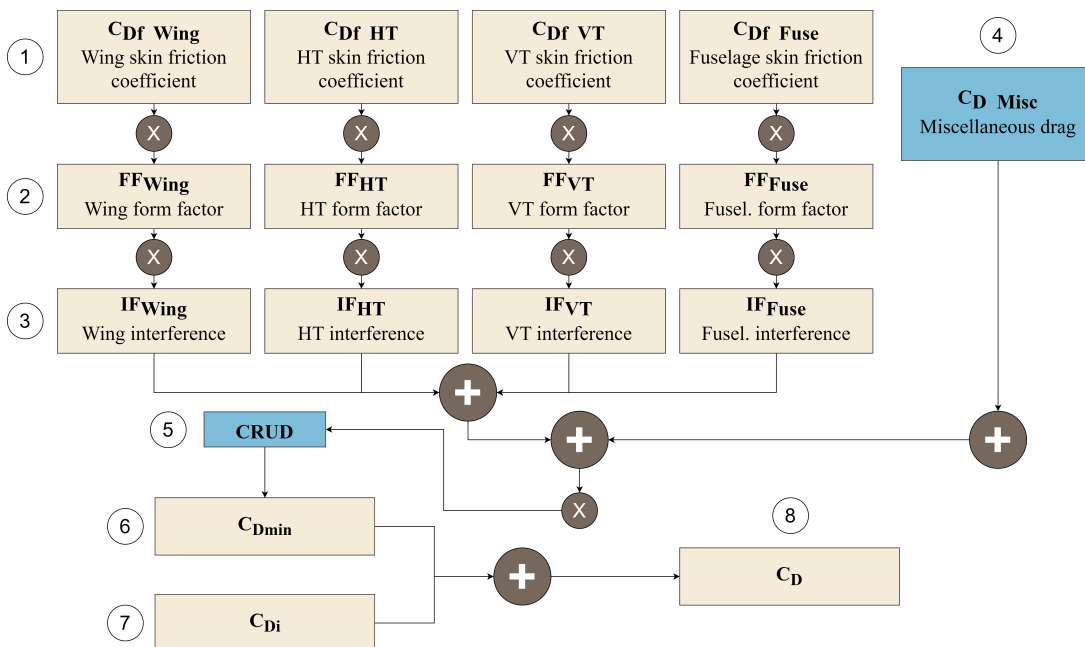
Figure 7.4: Component drag build-up method scheme [12]

The total drag coefficient will be computed for different phases of the mission. It will also be computed in emergency cases such as the situation where the engine fails.

Form and interference factors

The first step in computing the total drag coefficients of the different parts of the aircraft is to compute the skin friction coefficient. As shown in Figure 7.4, the skin friction coefficients must be multiplied by two factors which are the form (FF) and interference (IF) factors. The FF is considering the geometry of the volume analyzed and the effect of viscous separation whereas the IF is taking into account the drag due to interference between the different structures. Form factors and Interference factors are gathered in Table 7.8 for the different structures of the aircraft.

Table 7.8: Form and interference factors for different aircraft's structure.

	FF [-]	IF [-]
Wing	1.58	1
Horizontal tail	1.55	1.05
Vertical tail	1.55	1.05
Fuselage	1.19	1
Engine	1.35	1.5

Skin friction coefficients

Skin friction coefficients are varying depending on the state of the flow. Therefore, a certain amount of laminar and turbulent flow is estimated for each part of the aircraft. As advised by Torenbeek [14], for the wing and the tail, 10% of laminar flow will be considered and only 5% for the rest of the aircraft. The skin friction coefficients are then computed as:

$$C_{f_{lam}} = \frac{1.328}{\sqrt{Re}} \quad , \tag{7.5}$$

$$C_{f_{turb}} = \frac{0.455}{\log_{10} Re^{2.58}(1+0.144M^2)^{0.65}} \quad . \tag{7.6}$$

Miscellaneous drag coefficients

Miscellaneous drag is caused by small contributions that are often not taken into account but altogether have a non-negligible effect on the total drag of the plane. These contributions come from small inlets and outlets, access panels, fuel caps, etc. In this section, the trim drag, fuselage up-sweep drag, and washout drag are also computed. The miscellaneous drag coefficient for the above components is gathered in Table 7.9.

Table 7.9: Miscellaneous drag.

	$C_{D_{misc}}$ [-]
Trim	0.0017
Up-sweep	$3.47 \cdot 10^{-4}$
Washout	$4 \cdot 10^{-5}$

The sum of all these contributions gives the total miscellaneous drag coefficients. But an increase of 2% of the total coefficients is considered here to represent the leakage and protuberance drag. This drag is very difficult to predict by any method. "Leakage drag is due to the tendency of the aircraft to inhale through holes and gaps in high-pressure zone and exhale into the low-pressure zone", Raymer [9]. Protuberance drag is due to antennas, lights, actuator fairings, and other manufacturing defects.

Finally, the total miscellaneous drag coefficients have a value of 0.002.

Minimum drag coefficients

The minimum drag coefficient is gathering the skin friction coefficients and the miscellaneous drag coefficients to obtain the non-lift drag coefficient (C_{D_0}). It is computed as:

$$C_{D_0} = C_{D_f} + C_{D_{misc}} = \sum_i \frac{C_{f_i} \cdot FF_i \cdot IF_i \cdot S_{wetted,i}}{S_{ref}} + C_{D_{misc}} \tag{7.7}$$

where i is the different parts of the plane, C_{f_i} are the skin friction coefficients.

All the terms are known and the wetted surfaces of the different parts of the plane are gathered in Table 7.10.

Table 7.10: Wetted surfaces.

	S_{wetted} [ft^2]
Wing	161.46
Horizontal tail	32.3
Vertical tail	21.53
Fuselage	269.1
Engine	10.76
Nose landing gear	10.76
Main landing gear	21.52

The minimum drag coefficient is then computed for different phases of the mission. In particular, C_{D_0} is evaluated for cruise, loiter, landing, and take-off. For the landing and take-off phases, the additional drag coefficients due to

the deployment of the flaps have been added here in the minimum drag coefficient. The additional drag coefficients due to flaps are gathered in Table 7.11.

Table 7.11: Additional drag coefficients due to flaps.

	$C_{D_{flaps}}$ [-]
Landing	0.0229
Take-off	0.0012

Table 7.12 resumes the different minimum drag coefficients for these phases of the mission.

Table 7.12: Minimum drag coefficients for different phases of the mission.

	C_{D_0} [-]
Cruise	0.016
Loiter	0.0183
Landing	0.0609
Take-off	0.0387

Induced drag coefficients

Induced drag is caused by the production of lift. When a wing is lifting, the higher pressure air from the pressure side of the wing is escaping to the upper surface of it at the tip creating tip vortices and therefore drag but also reducing the lift. Since wing and tail are creating lift on a plane, the induced drag of these two components will be analyzed for different phases of the mission (cruise, loiter, take-off, landing). The induced drag coefficient is computed as:

$$C_{D_i} = \frac{C_L^2}{\pi \cdot AR \cdot (1 + \delta)} \ , \tag{7.8}$$

where δ is the drag factor which is estimated at 0.019 for a taper ratio of 0.3 following Gudmundsson [12]. Table 7.13 resumes the induced drag coefficients for the different phases of the mission.

Table 7.13: Induced drag coefficients for different phases of the mission.

	C_{D_i} [-]
Cruise	0.0039
Loiter	0.0074
Landing	0.073
Take-off	0.0673

Total drag coefficients

The total drag coefficient is computed by summing the minimum drag coefficient and the induced drag coefficient. As advised by Torenbeek [14] and Gudmundsson [12], the minimum drag coefficient must be multiplied by the CRUD factor (Cumulative Result of Undesirable Drag) which accounts for contributions that are practically impossible to account for otherwise. The CRUD factor is estimated at 15% ($CRUD = 1.15$).

The total drag coefficient is therefore computed as:

$$C_D = C_{D_0} \cdot CRUD + C_{D_i} \tag{7.9}$$

Table 7.14 resumes the total drag coefficients for the different phases of the mission.

Table 7.14: Total drag coefficients for different phases of the mission.

	C_D [-]
Cruise	0.0223
Loiter	0.0284
Landing	0.1651
Take-off	0.1321

Failure scenario

A failure scenario that might happen and must be taken into account is the situation where the engine is windmilling or completely stopped. It can occur due to a mechanical failure of the engine. Typically for the windmilling jet engine, the additional drag coefficient can be estimated at 0.196 at Mach 0.86 following NASA's jet engine research [38]. If the mechanical failure seizes the rotor, the additional drag coefficient will considerably increase. Following Torenbeek's book, the additional drag coefficient due to the stopped engine is 0.51.

Lift to drag ratio

Knowing the drag and lift coefficient values for the different phases of the mission, the lift-to-drag ratio can be computed. Table 7.15 summarizes the lift and drag coefficients and the lift-to-drag ratio that results from it. Figure 7.5 graphically shows the effect of a change of lift coefficient on the polar and the lift-to-drag ratio.

Table 7.15: Lift to drag ratio for different phases of the mission.

	C_D [-]	C_L [-]	L/D [-]
Cruise	0.022	0.224	10.05
Loiter	0.028	0.346	12.2
Landing	0.165	1.58	9.6
Take-off	0.132	1.5	11.3

In all phases, the lift-to-drag ratio is optimized to get the most performance out of the lifting devices of the aircraft. In addition, Boundary Layer Ingestion (BLI) will increase the lift-to-drag ratio by reducing the minimum drag component (C_{D_0}) from the total drag coefficient (further details in Section 7.4).
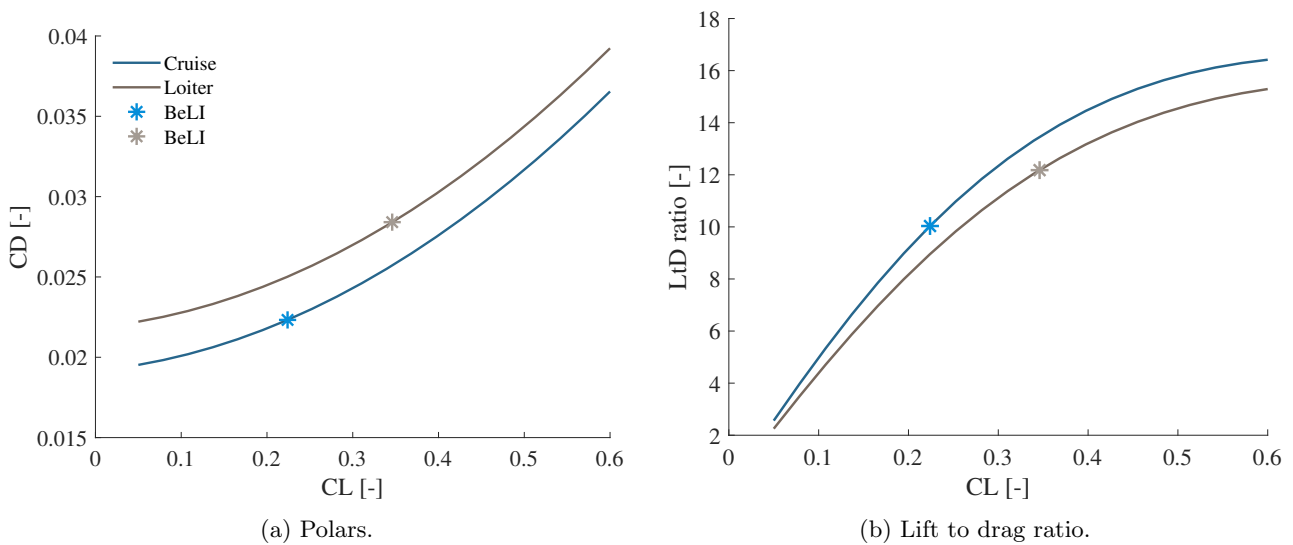

(a) Polars. (b) Lift to drag ratio.

Figure 7.5: Final polars and lift-to-drag ratio variations with respect to the lift coefficient of the BeLI for cruise and loiter conditions.

Comparison with DARTFlo

It is interesting to compare numerical results with those obtained with the drag study. More specifically, the induced drag of the wing is compared to the drag obtained with DARTFlo. Once again, cruise and loiter are studied and highlighted in Figure 7.6. For cruise, Figure 7.6a clearly shows that DARTFlo results are significantly higher than the drag study. On one hand, a possible cause can be the fact that the drag study does not take into account the wave drag. This effect is still present for loiter, and illustrated in Figure 7.6b, but because the speed is lower, the wave drag is much less noticeable. On the other hand, DARTFlo tends to overestimate shocks at high speeds, and is not as accurate as a viscous solver. Hence, the choice is made to keep on the results obtained with the drag study for the preliminary design. Nevertheless, the best way to get accurate results is, as said before, to use a viscous solver. A study with such a solver need to be performed in the following design steps to complete and validate the aerodynamics loads.
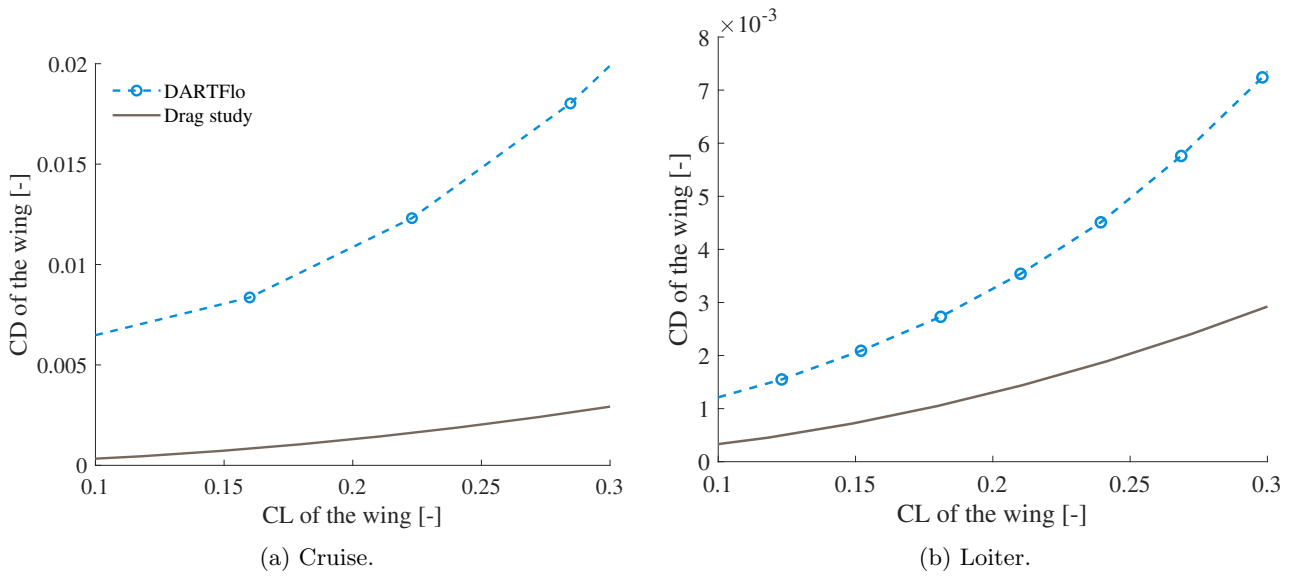
(a) Cruise.

(b) Loiter.

Figure 7.6: Comparison of the between the drag study polars and DARTFLO polars (wing).

7.3 Structure

7.3.1 Placard diagram

The Placard diagram of the BELI depicted in Figure 7.7 describes its velocity-altitude dependency in flight conditions.
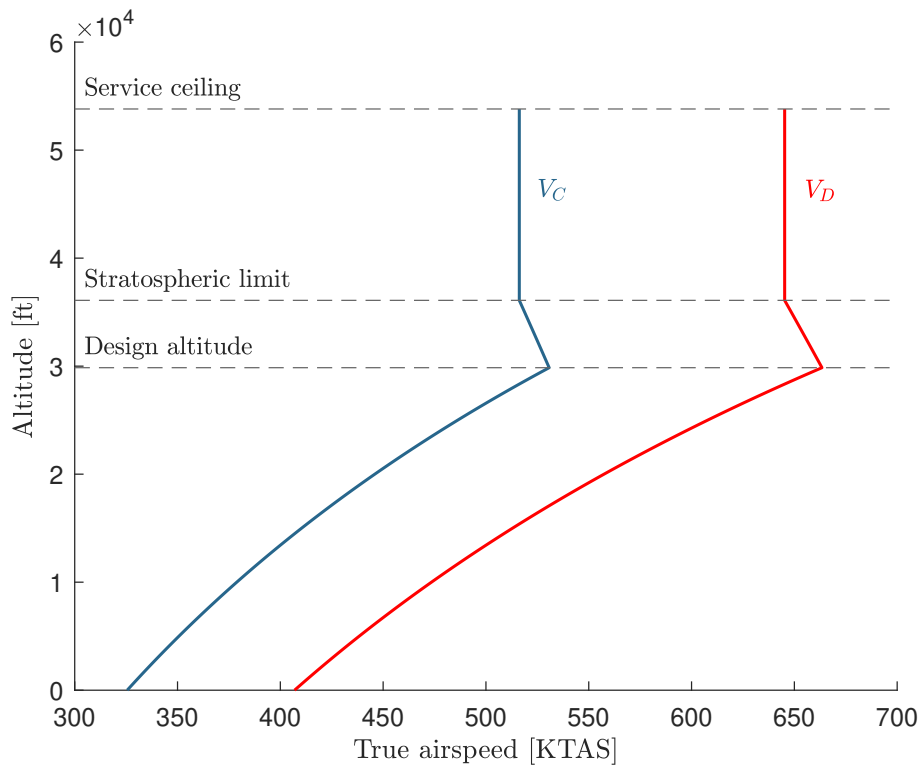

Figure 7.7: Placard diagram of the BELI.

The design cruise velocity V_C is defined as the one achieved when the maximum thrust of the propulsion system is applied. At design cruise altitude, it represents the dash speed of the aircraft. On the other hand, the design dive velocity is expressed by the former as $V_D = 1.25 \cdot V_C$ (Federal Aviation Regulation FAR definition)[3]. In order not to reach sonic conditions and tackle with compressibility effects, the Mach number is kept constant for higher altitude than the stratospheric limit. The service ceiling altitude and dash speed are both computed in Section 7.4. It can be seen from Figure 7.7 that the design cruise altitude of 30000 ft lies under the stratospheric limit.

7.3.2 Flight envelope

The flight envelope of an aircraft—V-n diagram—describes the evolution of the load factor n with respect to the equivalent airspeed V_e. It provides the different configurations that the BeLI can reach and withstand in a structural point of view. Figure 7.8 represents the flight envelope of the BeLI.
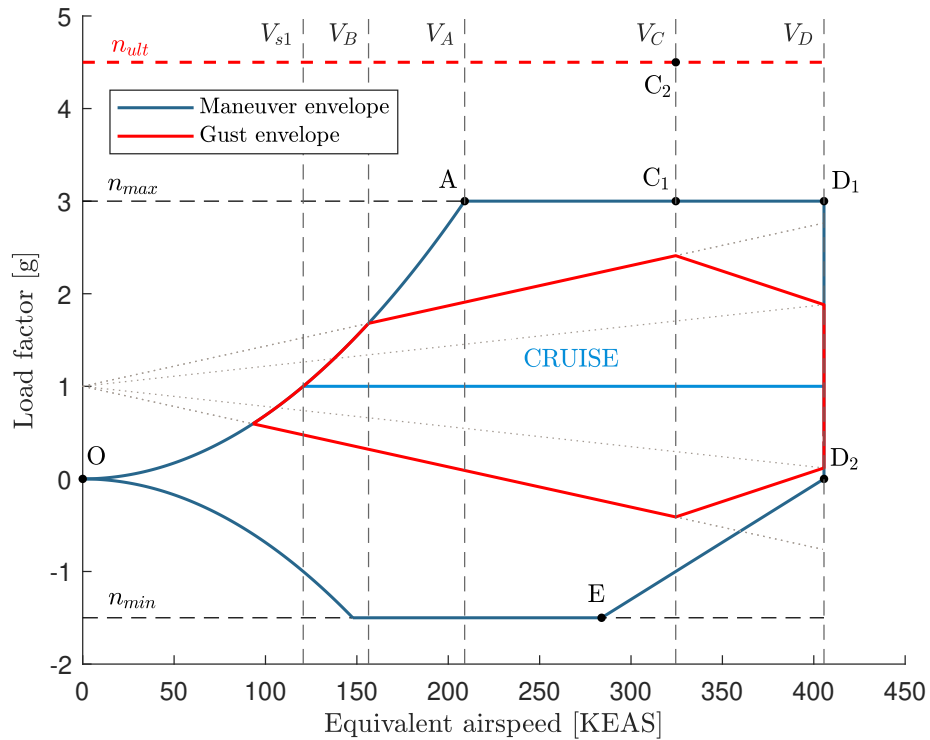
Figure 7.8: Maneuver and gust envelopes.

The KPPs limit the maneuver envelope load factors with $n_{min} = -1.5$ and $n_{max} = 3$. The design cruise and maximum velocities V_C and V_D are shown. The BeLI is nonetheless neither expected nor designed to operate in supersonic regions. Moreover, only a pull-out is meaningful when diving: a linear interpolation is performed between $n = 0$ and n_{min}. The stall curves (O-A and O-F in Figure 7.8) are given by

$$n = \frac{L}{W} = \frac{\rho_0 V_e^2 S C_{Lmax}}{2W}. \tag{7.10}$$

The stall velocity V_{s1} corresponds to the minimum velocity required in order to sustain steady-level flight for flaps-up configuration. The maximum velocity at which the total deflection of the control surfaces is still authorized is expressed by the design maneuverability speed V_A. As requested by the FAR, the following relation is respected:

$$V_A > V_{s1} \cdot n_{max}^{0.5} \Leftrightarrow 209 \text{ KEAS} > 208.8 \text{ KEAS.}$$ (7.11)

The gust envelope is then drawn similarly with the gust-induced load factor n_g given by

$$n_g = 1 + \frac{FC_{L\alpha}U_e V_e S}{498W}$$ (7.12)

with

$$F = \frac{0.88\mu}{5.3 + \mu}$$ (7.13)

and

$$\mu = \frac{2W}{\rho C_{L\alpha}cgS}.$$ (7.14)

The equivalent gust velocity U_e at a cruise altitude of 30000 ft can be interpolated from data of FAR as in [12]. Results are summarized in Table 7.16 hereunder.

Table 7.16: Gust equivalent velocities for critical velocities of the flight envelope.

Altitude [ft]	$U_e(V_B, V_C)$ [ft/s]	$U_e(V_D)$ [ft/s]
30000	± 36.29	± 18.14

The minimum speed V_B to enter a gust region is then located at the intersection of the upper stall curve and the gust load factor relation defined previously. To ensure a sufficient safety zone for the aircraft to fly, V_C has to be large enough to respect the following relation according to the FAR:

$$V_C > V_B + 1.32 \cdot U_e(V_B) \Leftrightarrow 324.5 \text{ KEAS} > 204.3 \text{ KEAS.}$$ (7.15)

Finally, two specific load factors are represented. First, the maximum load factor that the BeLI could undergo in flight is given by n_{lim}. Since the gust envelope of the BeLI remains inside the maneuver one, it is simply $n_{lim} = n_{max} = 3$. Secondly, the ultimate load factor, which has to withstand for a minimum of three seconds without failure, is defined as

$$n_{ult} = 1.5 \cdot n_{lim} = 4.5.$$ (7.16)

BeLI

Table 7.17 summarizes the different characteristic velocities of the flight envelope while the relevant points in Figure 7.8 will be discussed in Section 7.3.3 for a structural analysis.

Table 7.17: Relevant equivalent velocities of the flight envelope in KEAS.

V_{s1}	V_A	V_B	V_C	V_D
120.6	209	156.4	324.5	405.6

7.3.3 Loads

The purpose of this section is to analyze the loads acting on the BELI. Several flight conditions will be considered following the relevant points of the flight envelope determined in Section 7.3.2.

Aerodynamic loads

Considering the BELI geometry and forces acting on it represented in Figure 7.9, vertical forces equilibrium and moments equilibrium around the center of gravity can be written as

$$L + P = nW + T\sin(\alpha - \alpha_w) \tag{7.17}$$

and

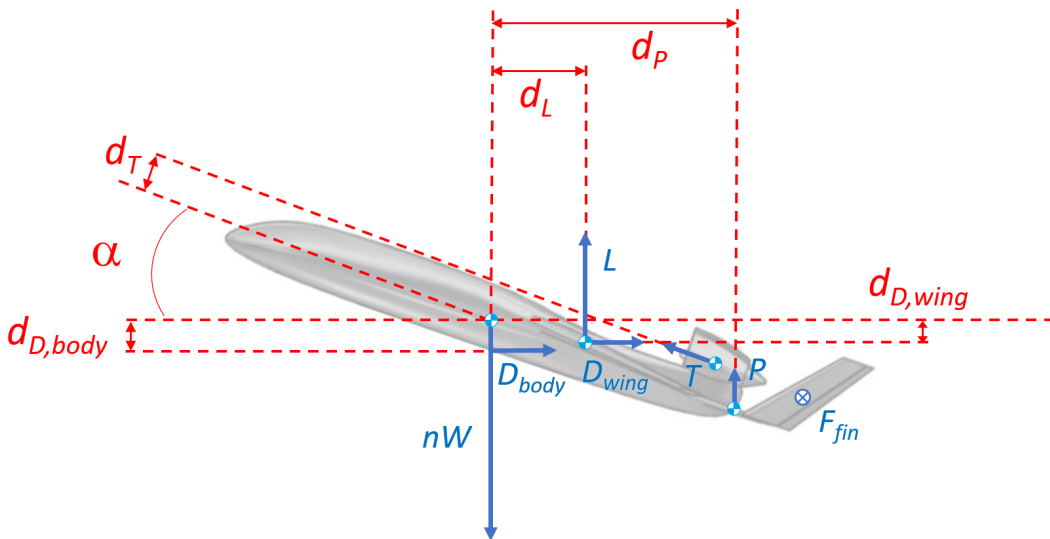$$I_\theta \ddot{\theta} = M - d_L L - d_P P - d_{D,body}D_{body} - d_{D,wing}D_{wing} - d_T T \quad . \tag{7.18}$$

Figure 7.9: Aerodynamic loads acting on the BELI.

The forces shown in Figure 7.9 are the BELI's apparent weight nW, the wing lift L, the tail lift P, the engine thrust T, the wing drag D_{wing}, the body drag D_{body} and the applied force on the fin F_{fin}. Moment arms associated with each force are also depicted in Figure 7.9. In Equation 7.17, α_w is the angle of attack of the wing at the root and α is the angle of attack of the BELI. In Equation 7.18, M is the pitching moment of the aircraft due to the one of the wing and due to yaw, I_θ is the pitching moment of inertia about the center of gravity that can be determined using the BELI's CAD and $\ddot{\theta}$ is the pitching acceleration with a $60°/s^2$ maximum value considered [39].

L, P and α can be determined using an iterative process for some relevant points of the flight envelope defined in Figure 7.8. These aerodynamic loads are given in Table 7.18 for each relevant flight condition where V_e is the equivalent air speed and n is the load factor. These parameters were determined in Section 7.3.2. Note that the angle of attack α for point A is fixed by the stall angle of the BELI at 209 KEAS. M_{fus} is the moment acting on the fuselage due to F_{fin} defined by

$$F_{fin} = \frac{1}{2}\rho V^2 S_{fin} a_{fin} \psi \ , \tag{7.19}$$

where S_{fin} is the fin surface, a_{fin} is the lift-curve slope and ψ is the maximum yaw angle allowed with a 15° value considered for this parameter [39].

Table 7.18: Aerodynamic loads acting on the BELI.

Points	V_e [KEAS]	n [g]	α [°]	L [lbf]	P [lbf]	M_{fus} [lbf·ft]
A	209	3	12.0	21885	-2249	1200
C_1	324.5	3	8.5	22712	-2996	2893
C_2	324.5	4.5	13.7	33190	-3658	2893
D_1	405.6	3	4.7	23577	-3819	4520
D_2	405.6	0	-2.0	2702	-2590	4520
E	283.9	-1.5	-8.8	-8962	-805	2214

Rear fuselage loads

From the aerodynamic loads given in Table 7.18, critical parts of the BELI can be analyzed. The first is the rear of the fuselage, the beginning of which is defined just after the wing trailing edge. The analysis of this specific part is important because it has to sustain its own weight, all the loads acting on the tailplane, and the engine thrust and weight. The weight of the rear of the fuselage is 135 lbs. The tail, fin, and engine weights are given in Table 6.9. The tail lifts P and fuselage moment M_{fus} are given in Table 7.18.

Knowing all these loads, the reaction forces and moments at the section just after the wing trailing edge are given in Table 7.19. They are calculated by balancing the forces and moments at this section and taking the origin as

the centroid of the section. The *X*-axis is pointing from nose to tail, the *Y*-axis is aligned with the wing span and is symmetric and the *Z*-axis is pointing up.

Table 7.19: Reaction forces and moments acting on the section at the beginning of the rear fuselage.

Points	T_y [lbf]	T_z [lbf]	M_x [lbf·ft]	M_y [lbf·ft]	M_z [lbf·ft]
A	-2008	-5165	-1200	35039	18022
C_1	-4840	-6774	-2893	42274	43445
C_2	-4840	-9169	-2893	55001	43445
D_1	-7561	-7660	-4520	49966	67874
D_2	-7561	-2641	-4520	23238	67874
E	-3705	1063	-2214	-691	33254

Wing loads

The second important component to analyze is the wing. It has to sustain the lift and drag it creates for all relevant points of the flight envelope, its own weight, the weight of the fuel stored in it, and the weight of the fuel tank. All these weights are summarized in Table 6.9 and the wing lift *L* is given in Table 7.18. The wing drag D_{wing} is calculated for all considered points of the flight envelope during the iterative process.

Similarly to the rear of the fuselage analysis, an equilibrium of the forces and moments at the wing root is carried out in order to get the reaction forces and moments at this section. The results are summarized in Table 7.20 using the same reference frame as in the rear fuselage section with the centroid of the root as the origin. It must be noted that for this analysis, only half a wing will be considered thereby dividing by two the loads applied.

Table 7.20: Reaction forces and moments acting on the wing root.

Points	T_x [lbf]	T_z [lbf]	M_x [lbf·ft]	M_y [lbf·ft]	M_z [lbf·ft]
A	-1909	10603	38108	-22924	6857
C_1	-843	11179	40186	-24127	3020
C_2	-3080	16062	57730	-34701	11059
D_1	313	11679	41989	-25168	-1141
D_2	1315	1306	4713	-2699	-4746
E	-60	-4437	-15934	9681	208

7.3.4 Structural design

In this section, the structure of the rear of the fuselage and the wing will be designed to sustain the loads determined in Section 7.3.3.

BeLi

Material properties and safety factor

Both rear fuselage and wing will be made of 7075 T6 aluminum alloy. The material properties are given in Table 6.7. In order to take into account a safety factor of $s = 1.3$, the structure should not undergo more than maximum direct stress σ_{max} or maximum shear stress τ_{max} of $\sigma_{max} = \sigma_y^0/s = 56$ ksi and $\tau_{max} = \tau_{strength}/s = 37$ ksi.

Rear fuselage structure

The rear fuselage section geometry is represented in Figure 7.10. It is symmetric and is made of 30 stringers all along the skin. The upper curved shape of the section is due to the presence of the engine at the back of the fuselage.
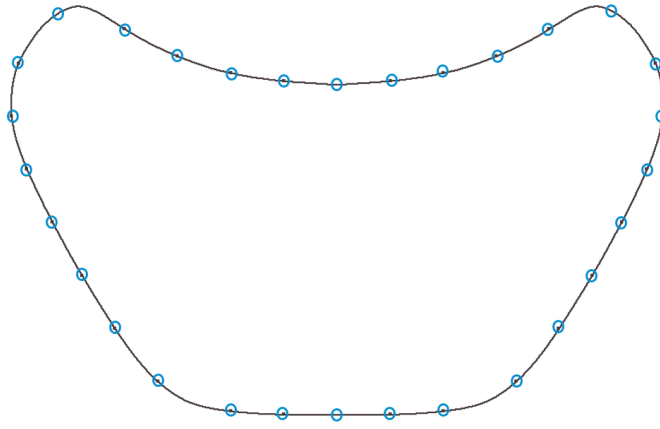

Figure 7.10: Rear fuselage section structure.

In order to determine the minimum cross-section area of the stringers $B_{i,min}$, the direct stress along each stringer i has to be calculated using the following formula [40]

$$\sigma_{xx,i} = \frac{(I_{zz}M_y + I_{yz}M_z)z_i - (I_{yz}M_y + I_{yy}M_z)y_i}{I_{yy}I_{zz} - I_{yz}^2} \ , \tag{7.20}$$

where $I_{ab} = \sum_i B_i a_i b_i$ with $a, b = \{x, y, z\}$ are the second-moment area of the section using stringers with a cross-section area B_i. Due to the symmetry of the section depicted in Figure 7.10, $I_{yz} = 0$ and Equation 7.20 simplifies to

$$\sigma_{xx,i} = \frac{M_y}{I_{yy}} z_i - \frac{M_z}{I_{zz}} y_i \ , \tag{7.21}$$

where M_y and M_z are given in Table 7.19. From Equation 7.21, the minimum stringer area $B_{i,min}$ is obtained by imposing $\sigma_{xx,i} \leq \sigma_{max}$ for each stringer i. This leads to $B_{i,min} = 0{,}094$ in^2, which seems consistent for a fuselage stringer.

The minimum skin thickness can be determined by computing the shear flows q^i and q_T passing through each panel i due to the shear loads T_y and T_z and the moment M_x. The formulas to calculate this shear flow are given by

$$q^{i+1} = q^i - \frac{T_z}{I_{yy}} z_i B_i - \frac{T_y}{I_{zz}} y_i B_i \qquad (7.22)$$

and

$$q_T = \frac{M_x}{2A} \ , \qquad (7.23)$$

where T_y, T_z, M_x are given in Table 7.19 and A is the section area determined using the BeLI's CAD. The minimum skin thickness t_{min} is restricted by $(q^i_{max} + q_T)/t \leq \tau_{max}$ for every panel. In other words, $t_{min} = (q^i_{max} + q_T)/\tau_{max} = 0.06$ in.

At the rear fuselage, 6 frames are used to support the engine and prevent buckling. By the calculated area of the stringers for the rear fuselage, the dimensions of the stringers are shown in Figure 7.11.
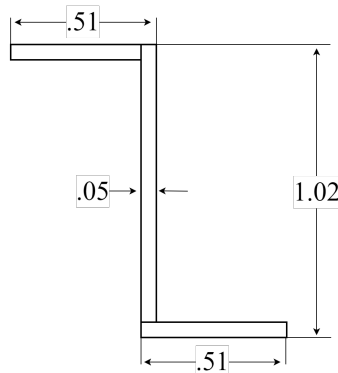
Figure 7.11: Geometry of the fuselage stringers [in].

Wing structure

The wing root geometry is shown in Figure 7.12. Due to the NACA SC 0414 airfoil profile determined in Section 6.2.2, it is not symmetric and is made of 36 stringers. Note that the flaps and ailerons are not represented here.
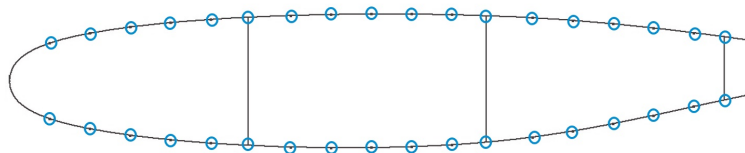
Figure 7.12: Wing root structure.

Similarly to the minimum cross-section of the rear fuselage stringers determination, one of the wing can be calculated with the direct stress in each stringer i:

$$\sigma_{yy,i} = \frac{(I_{zz}M_x + I_{xz}M_z)z_i - (I_{xz}M_z + I_{zz}M_x)x_i}{I_{xx}I_{zz} - I_{xz}^2}, \tag{7.24}$$

where I_{xz} is no more zero due to the asymmetric profile of the wing and Equation 7.24 can not be simplified. M_x and M_z are given in Table 7.20. By imposing $\sigma_{yy,i} \leq \sigma_{max}$ for each stringer i, it leads to $B_{i,min} = 0.037$ in^2.

The wing is composed of three cells. For each cell j, the skin has to sustain the shear flow passing through each panel i due to the shear loads T_x and T_z and the moment M_y (given in Table 7.20). The shear flow $q_{M,j}$ due to the moment M_y is governed by [40]

$$M_y = \sum_j 2A_j q_{M,j} \tag{7.25}$$

and

$$\left(\frac{d\theta}{dy}\right)_j = \frac{1}{2A_j G} \oint_j \frac{q_{M,j}}{t_i} ds, \tag{7.26}$$

where A_j is the cell area and $\left(\frac{d\theta}{dy}\right)_j$ is its twist rate. G is the shear modulus and t_i is the panel thickness. Taking into account the taper of the wing, web shear can be defined as [40]

$$T_x^{web} = T_x - \sum_i \sigma_{yy,i} B_i \frac{\delta x_i}{\delta y} \tag{7.27}$$

and

$$T_z^{web} = T_z - \sum_i \sigma_{yy,i} B_i \frac{\delta z_i}{\delta y}, \tag{7.28}$$

where $\frac{\delta x_i}{\delta y}$ and $\frac{\delta z_i}{\delta y}$ quantify the x and z taper of the wing along the y-direction. The open shear flow q^c produced by T_x^{web} and T_z^{web} is [40]

$$q_j^c = -\left(\frac{T_x^{web}I_{xx} - T_z^{web}I_{xz}}{I_{xx}I_{zz} - I_{xz}^2}\right)\sum_i B_i x_i - \left(\frac{T_z^{web}I_{zz} - T_x^{web}I_{xz}}{I_{xx}I_{zz} - I_{xz}^2}\right)\sum_i B_i z_i. \tag{7.29}$$

Finally, a balance between each twist rate of adjacent cells gives the initial shear flow $q_{0,j}^c$ at the cut from where the open shear flow q_j^c is defined. The total shear flow in each panel j is $q_j = q_{M,j} + q_j^c + q_{0,j}^c$. The skin thickness t has to verify $q_{j,max}/t \leq \tau_{max}$ and leads to a minimum skin thickness of $t_{min} = 0.06$ in.

In order to prevent the wing from buckling 11 ribs are used for each side of the wing. From the previous findings, spar thickness is set to 0.275 in, and ribs thickness is set to 0.118 in. By the calculated stringer area, stringer dimensions for the wing are shown in Figure 7.13.
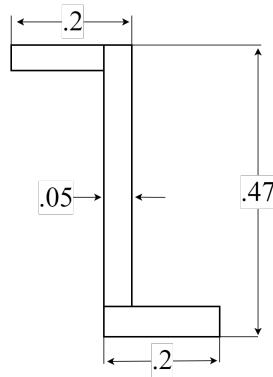
Figure 7.13: Geometry of the wing stringers [in].

7.3.5 Finite element analysis of the rear fuselage

Model

The rear fuselage is analyzed after the wing trailing edge, which means 6ft of the rear of the fuselage is taken into the simulation. Prepared model of the rear fuselage shown in Figure 7.14. From Figure 7.14, skin is shown in white, frames are shown in blue, and stringers are shown in black. Also, in order to simplify the model, each stringer is modeled as a bar while keeping the same length and area. In other words, only thickness is changed while keeping the same area.
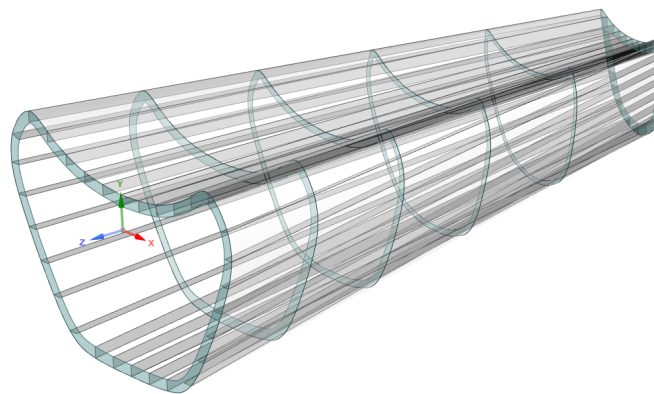

Figure 7.14: Rear fuselage model.

Meshing and boundary conditions

Again, the model is prepared by shell surfaces to decrease the computation time and easy application of the Quad elements. In order to define optimum mesh size, again mesh convergence study has been done and the final meshed model is shown in Figure 7.15.
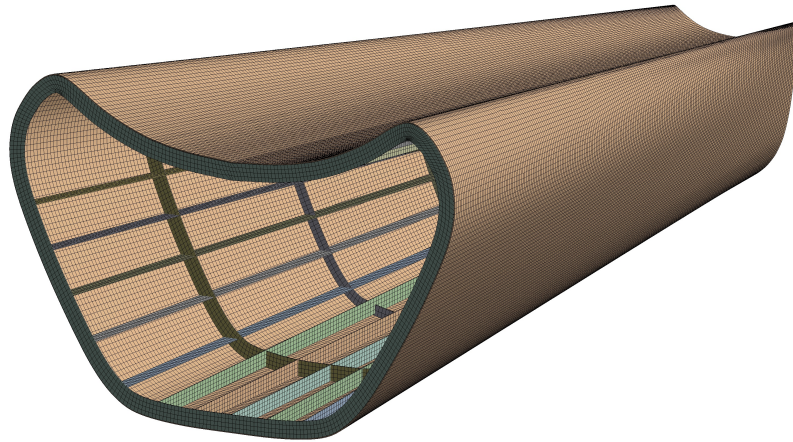
Figure 7.15: Rear fuselage mesh.

In order to simulate the connection of the tail and fuselage, the front of the rear fuselage (point G in Figure 7.16) is assigned as fixed support. Also, multiple loads are applied to the structure as shown in Figure 7.16. These are:

- (A) moment caused by the fin applied directly to the end of the rear fuselage;

- (B) weight of the empennage applied as a remote force which enables to apply of a force on the structure from a remote point that takes into account the moment caused by force;

- (C) weight of the engine applied from the center of gravity of the engine;

- (D) weight of the rear fuselage applied from the center of gravity of the rear fuselage;

- (E) aerodynamic force caused by the horizontal stabilizer;

- (F) thrust of the engine.

Figure 7.16: Boundary conditions of the rear fuselage.

Results and discussion

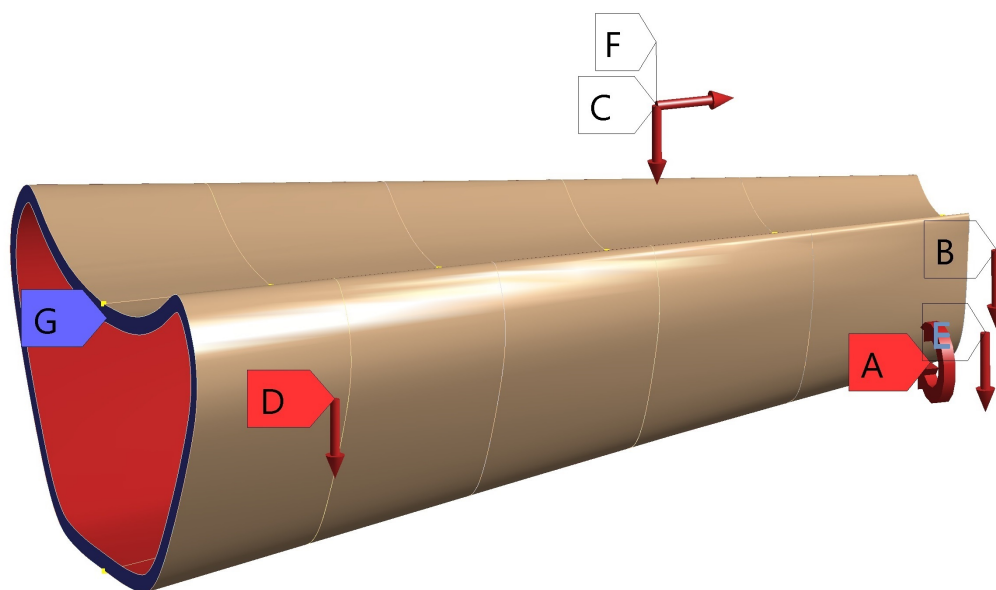Since the front of the rear fuselage is assigned as fixed support, most of the deformation is expected to occur at the end of the fuselage. From Figure 7.17, it can be seen that because of the moment applied on the fuselage, maximum deformation is on the side of the structure. Also, the stress distribution is concentrated on the end of the fuselage and the right-top side of the frame faced the maximum stress of 50659 psi.

A: Static Structural
Equivalent Stress
Type: Equivalent (von-Mises) Stress
Unit: psi
Time: 1

50659 Max
13152
12056
10960
9863,8
8767,8
7671,9
6575,9
5479,9
4383,9
3287,9
2192
1096
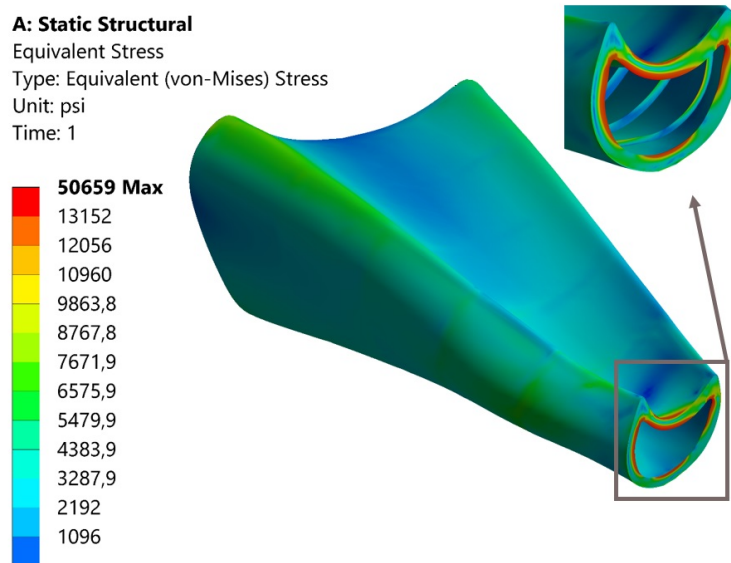
Figure 7.17: The von Mises equivalent stress on the fuselage [psi].

The displacement of the rear fuselage is shown in Figure 7.18. The displacements' magnitude is relatively small. The explanation is that loads move in the direction of the greatest inertia. Actually, lift acts in the direction of the end of the fuselage's upper surface, and applied moment acts in the same direction and that is why one side of the rear fuselage faces displacement more.

A: Static Structural
Total Deformation
Type: Total Deformation
Unit: in
Time: 1

0,30578 Max
0,12639
0,10833
0,090277
0,072221
0,054166
0,036111
0,018055
0 Min
0
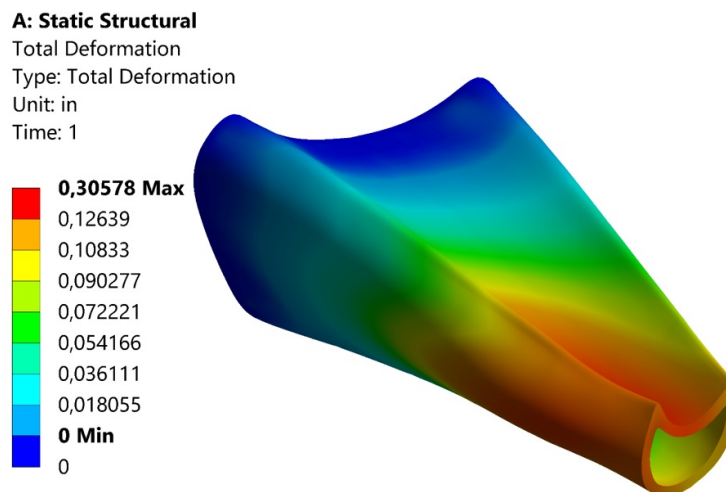
Figure 7.18: Rear fuselage displacements [in].

By the result of the equivalent von Mises stress and displacement, shear distribution is expected to occur on the same section as well. However, shear stress is concentrated on the left-top side of the end of the fuselage as shown in Figure 7.19. This is because of the moment of the fuselage applied on the section since it is applied on the *x*-axis.
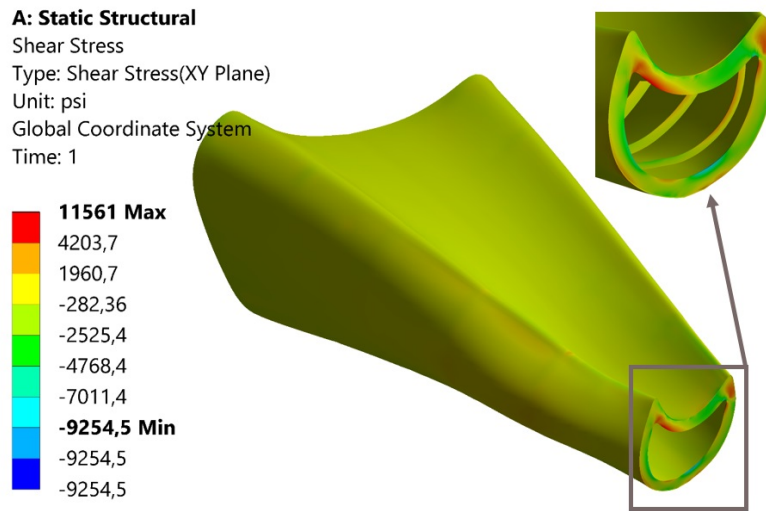
Figure 7.19: Shear stress of the rear fuselage [psi].

In order to validate the safety of the structure on the rear fuselage, the factor of safety for equivalent von Mises stress needs to be considered and is shown in Figure 7.20.
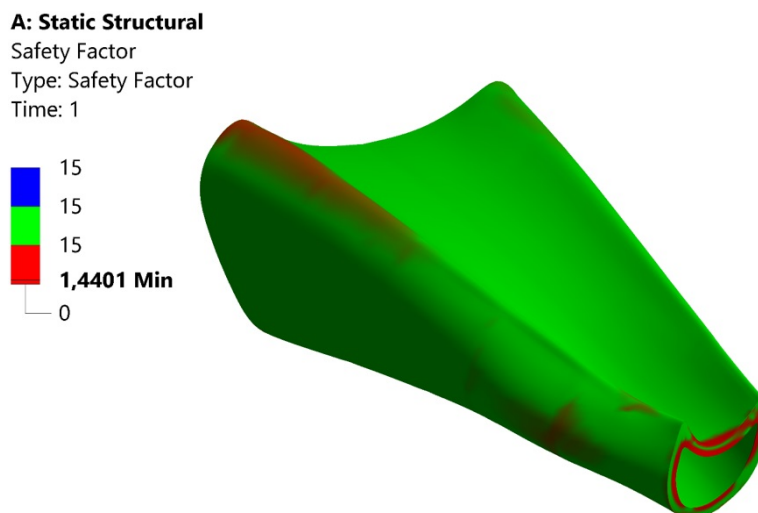
Figure 7.20: Factor of Safety of the rear fuselage.

Since from the requirements minimum factor of safety is determined as 1.3, the rear fuselage is able to carry the loads by a factor of safety of 1.44.

Conclusion

Using the loads that have been calculated in the analytical section, the finite element analysis has been carried out on a high-quality mesh. Table 7.21 provides an overview of significant findings from simulation and analytical.

Table 7.21: Results of the Finite Element Method for the rear fuselage.

Parameter	Simulation	Analytical
Maximum displacement [in]	0.3	-
Maximum shear stress [psi]	11561	36923
Maximum von Mises' stress [psi]	50659	53254
Factor of Safety [-]	1.44	1.3

By comparison, it appears that the calculations done in the analytical do not exactly match the result of the simulation. It is expected since in the analytical calculations, loads are applied to the exact locations as in the simulation but the reactions of the loads are summarized only at the front section of the rear fuselage in the analytical solution. Moreover, in the analytical study, skin and frames are considered to carry only shear stresses and no direct stresses, but simulation shows that they do carry both. Finally, in the finite element approach, skin and frames also carry some direct loads in addition to stringers, which are analytically considered to carry all direct stresses and no shear stress. As a result, in the simulation, a greater load factor value of 1.44 is achieved even though in the analytical study the factor of safety is taken as 1.3. In other words, structural stability is achieved and it can be observed that the loads are within the capacity of the materials specified in Table 6.7, meaning that the fuselage is able to support the structural and aerodynamic loads of the tail, even for $n = 4.5$. Hence, the BELI is able to perform all flight conditions defined in Figure 7.8 under KPPs.

7.3.6 Finite element analysis of the wing

In order to validate the assumptions made in the analytical part, a static structural analysis will be performed for the wing.

Model

In modeling by considering the decrease of the computation time, only half of the wing which means the span of 13 ft is taken into simulation from the root chord since its symmetric. Also, the wing model is prepared from shell elements to decrease the computation time by comparing to three-dimensional simulation and from Figure 7.21 inner structure can be seen while spars are shown in purple, ribs are shown in pink, skin shown in white, and stringers are shown as black. A similar approach that of the rear fuselage stringers is applied for the wing. Stringers are simplified to bars so that their lengths and area are kept the same except for the thickness in order to keep the same area.
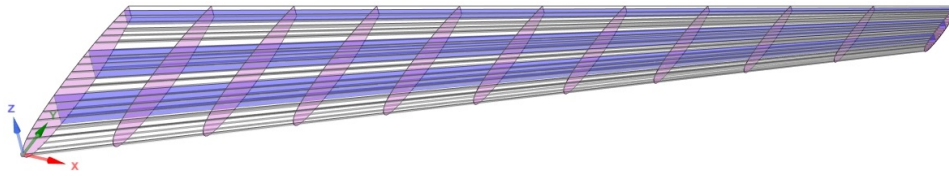
Figure 7.21: Representation of the wing.

Meshing and boundary conditions

By modeling the geometry from sheets, it enabled to use of Quadrilateral elements more easily. Quad elements are chosen since when expressing the local geometry of a surface, quad meshes naturally have an advantage over triangle meshes. Furthermore, in order to define the optimal mesh size, mesh convergence has been performed, and final meshed wing geometry is shown in Figure 7.22.
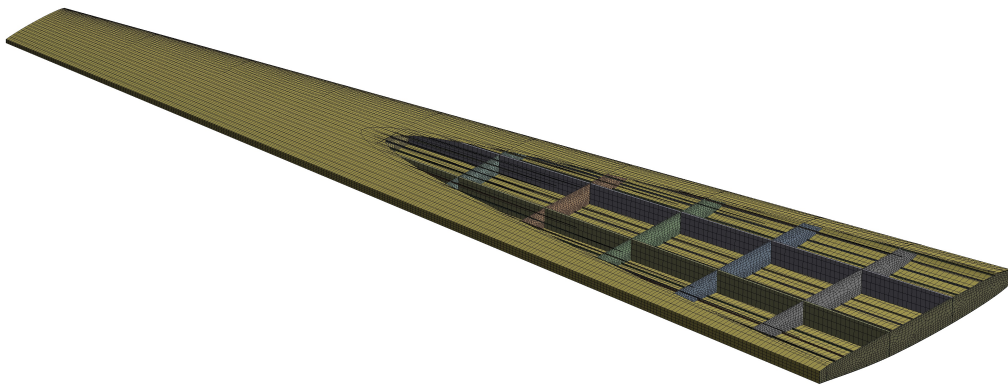
Figure 7.22: Wing mesh.

For the boundary conditions, multiple loads are considered, such as wing structural weight and aerodynamic loads that apply to the wing, imported from CFD resulting in line pressure directly applying on the surface along the span. For the simulation maximum loading case which is $n = 4.5$ from Figure 7.8 is taken into account to ensure the structural stability of the wing. In addition, the root chord of the wing is assigned as fixed support.

Result and discussion

Since the wing's root is assigned as fixed support and forces acting on the wing are normal to the surface, wing displacement can be observed upward in Figure 7.23.

B: Static Structural
Total Deformation
Type: Total Deformation
Unit: in
Time: 1

9,907 Max
8,8062
7,7054
6,6046
5,5039
4,4031
3,3023
2,2015
1,1008
0 Min

Figure 7.23: Wing displacement [in].

From Figure 7.23, it can be seen that maximum displacement is at the tip of the wing as 9.09 in. Although the displacement of the wing is quite large, the maximum equivalent von Mises' stress is calculated as 49978 psi in Figure 7.24.

B: Static Structural
Equivalent Stress
Type: Equivalent (von-Mises) Stress
Unit: psi
Time: 1

49978 Max
32985
28273
23561
18849
14137
9424,4
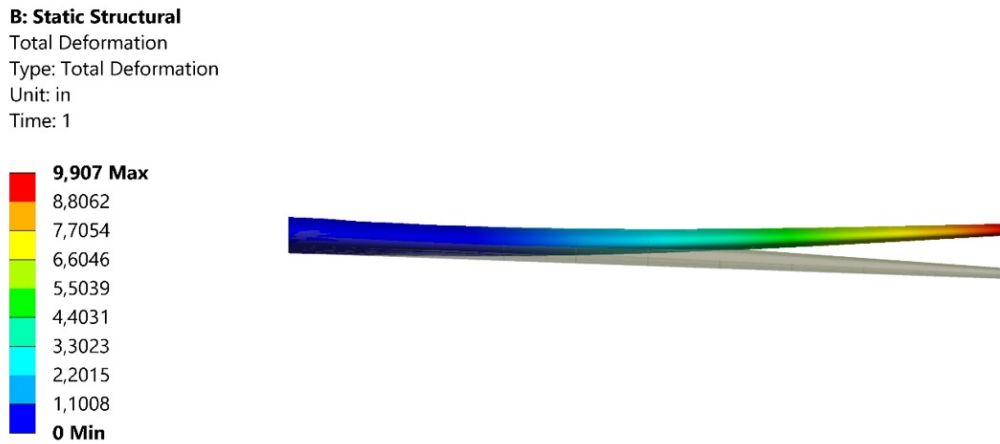4712,2
0 Min
0
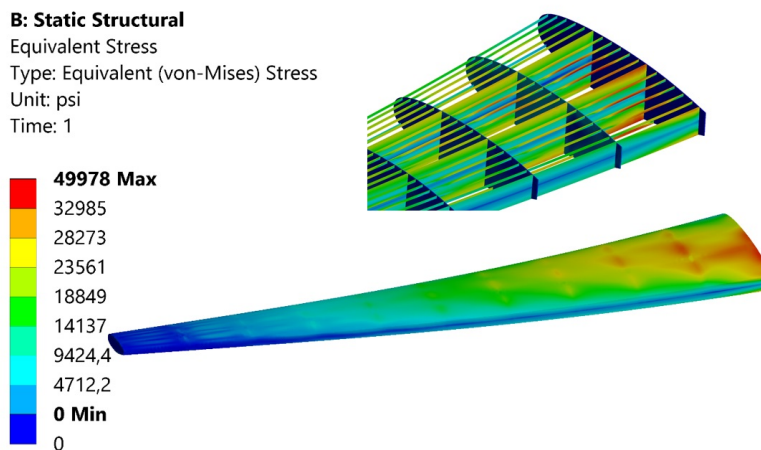
Figure 7.24: The von Mises equivalent stress on the skin and inner components [psi].

From Figure 7.24, it can be seen that most of the stress is concentrated on the root side. the result seems logical since the loading structure on the root side faces most of the tension and compression and decreases over the span. Also, because of the Lift distribution over the span, the root side faces most of the force as well. In other words, the stress distribution is parallel to the distribution of the loads. In addition, it is clear that, with the exception of stringers, the heaviest loaded place also experiences the greatest shear pressures. That leads to the conclusion that stringers carry almost all direct stresses, which is consistent with the theory put forward in the analytical study. Furthermore, from the Figure 7.25, it can be seen that shear stress loads on skin and spars instead of stringers, due to the loading there is a surface deformation on the skin when the effect of the result is increased.

B: Static Structural
Shear Stress
Type: Shear Stress(XY Plane)
Unit: psi
Global Coordinate System
Time: 1

	16570 Max
	6729,3
	3574,9
	420,52
	-2733,9
	-5888,3
	-9042,7
	-12197
	-15352
	-19432 Min
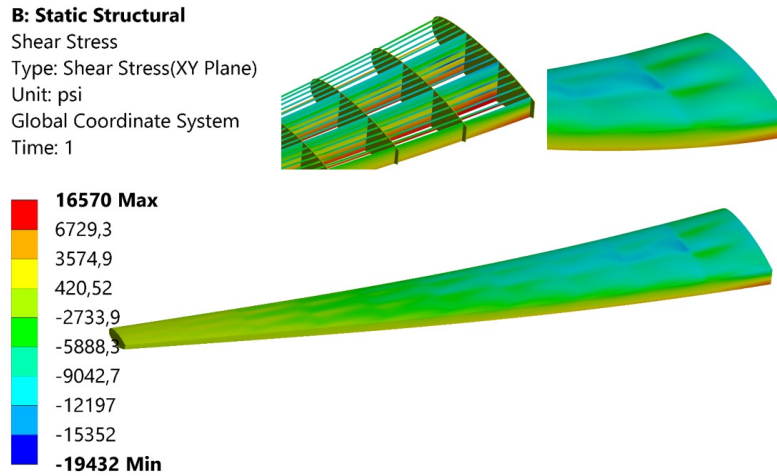
Figure 7.25: Shear stress on the skin [psi].

Finally, in order to provide the threshold determined for the maximum loading of the wing, the factor of safety of the wing is evaluated in Figure 7.26 and calculated as 1.4. Since it is over the minimum requirement of 1.3, the wing can perform the mission profile safely.

B: Static Structural
Safety Factor
Type: Safety Factor
Time: 1

	15
	15
	5
	1,4597 Min
	0

Figure 7.26: Factor of safety of the wing.

Conclusion

Finite element analysis of the wing is performed by the precise data provided by DARTflo with fine mesh. Since the wingtip deflection value is in the range of 1% of the span, it is acceptable. Table Table 7.22, provides a summary of the findings which were found in the finite element method and analytical part.

Table 7.22: Results of the Finite element method for the half wing.

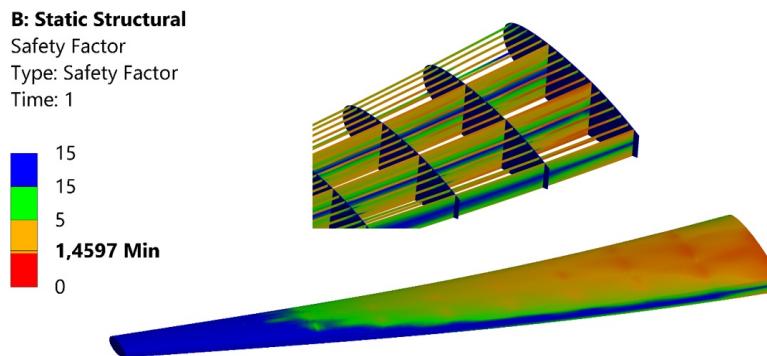| Parameter	Simulation	Analytical
Maximum displacement [in]	9.9	-
Maximum shear stress [psi]	16570	35810
Maximum von Mises' stress [psi]	49978	56154
Factor of Safety [-]	1.46	1.3

The finite element study supports the analytical findings with respect to the maximum shear stress since the same order of magnitude is retrieved. There is nevertheless nearly a factor of 1.1 difference for the von Mises' stress. Multiple assumptions can be made to explain this difference:

- in the finite element analysis, the lift is applied on the surface as pressure where values are taken from CFD along the entire span, whereas in equilibrium equations, the lift is applied to the wing as a consequent acting on one point which is the aerodynamic center;

- in analytical computations it is assumed that shear stress is carried by the spars and skin panels without direct stresses; however, in the simulation, it is observed that they carry both of the stresses;

- in the analytical study, stringers are assumed to carry only direct stresses, but simulation shows that they also carry both stresses.

The substantial difference between the maximum von Mises stresses which are determined analytically and by the simulation can be explained by these assumptions. As a result, in the simulation, a greater load factor value of 1.46 is achieved even though in the analytical study the factor of safety is taken as 1.3. Therefore, the wing is able to handle the structural and aerodynamic loads in both situations since the loads are within the limits of the materials specified in Table 6.7, even for $n = 4.5$. The BeLI is able to perform all flight conditions defined in Figure 7.8 under KPPs.

7.4   Performance

In this section, performance of the BeLI is first computed as if BLI did not occur (*cf.* "General considerations"). Then, an enhanced performance due to the reduction of the drag thanks to the BLI is investigated (*cf.* "BLI enhanced performance"), as discussed in Section 1. A mean reduction of the drag is expected to be $\mu = 9.52\%$ with a standard deviation of $\sigma = 2.18\%$, as stated in Section 6.4.1. This is applied to the zero drag coefficient since it is the major part of the drag reduced by ingesting the boundary layer of the fuselage.

7.4.1 Take-off

General considerations

The BELI is expected to take off within a 1500 to 4000 ft runway length while considering a clearance height h_{ob} of 30 ft. The take-off is performed in successive stages as described in Figure 7.27.
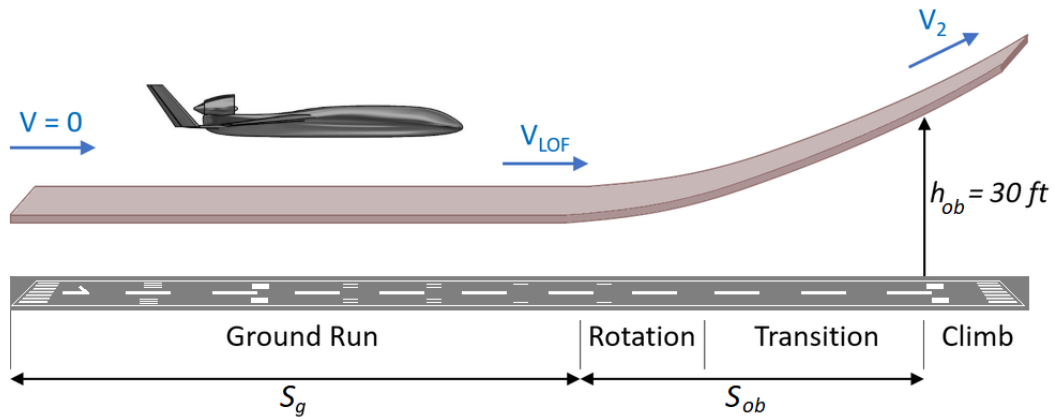
Figure 7.27: Take-off stages retrieved from [12].

The methodology followed is the one of the Gudmundsson [12]. The ground run corresponds to distance S_g for the aircraft to accelerate from usually zero velocity to the lift-off velocity V_{LOF}, computed as followed:

$$V_{LOF} = 1.556 \cdot \left(\frac{W}{\rho_0 S C_{Lmax}} \right)^{0.5} . \tag{7.30}$$

The ground run distance can then be approximated as

$$S_g = \frac{V_{LOF}^2}{2a} , \tag{7.31}$$

with

$$a = \frac{g}{W} [T - D - \mu(W - L)] , \tag{7.32}$$

where the friction coefficient is denoted by μ. Afterward, the air run distance S_{ob} consists in clearing a height of $h = 30$ ft. Depending on the value of the transition height,

$$h_{tr} = R \cdot (1 - \cos\theta) \tag{7.33}$$

with

$$R = 0.2156 \cdot V_{stall}^2 \tag{7.34}$$

and

$$\theta = \sin^{-1}(\frac{T}{W} - \frac{C_D}{C_L}) \ , \tag{7.35}$$

two cases can be encountered. All previously defined relations are computed at the transition speed $V_{tr} = 1.15 \cdot V_{stall}$ depending on the stall velocity. If the transition height is greater than the clearance height, then

$$S_{ob} = (R^2 - (R - h_{ob})^2)^{0.5} \ . \tag{7.36}$$

On the other hand, the air distance is composed of the transition distance and a short climb distance to reach the clearance height:

$$S_{ob} = S_{tr} + S_{climb} \tag{7.37}$$

with

$$S_{tr} = 0.2156 \cdot V_{stall}^2(\frac{T}{W} - \frac{C_D}{C_L}) \ , \tag{7.38}$$

$$S_{climb} = \frac{h_{ob} - h_{tr}}{\tan\theta} \ . \tag{7.39}$$

The total take-off distance is thus defined as the sum of the ground run and the air run [12].

Said take-off distances can be computed for both dry and wet conditions, respectively $\mu = 0.02$ and $\mu = 0.04$ [9], and for different altitudes. The evolution of the take-off length of the BeLI is depicted in Figure 7.28 while relevant characteristics of the take-off phase are summarized in Table 7.23.

Table 7.23: Summary of take-off distances for both dry and wet runway conditions for sea level and 5000 ft altitude, computed without BLI.

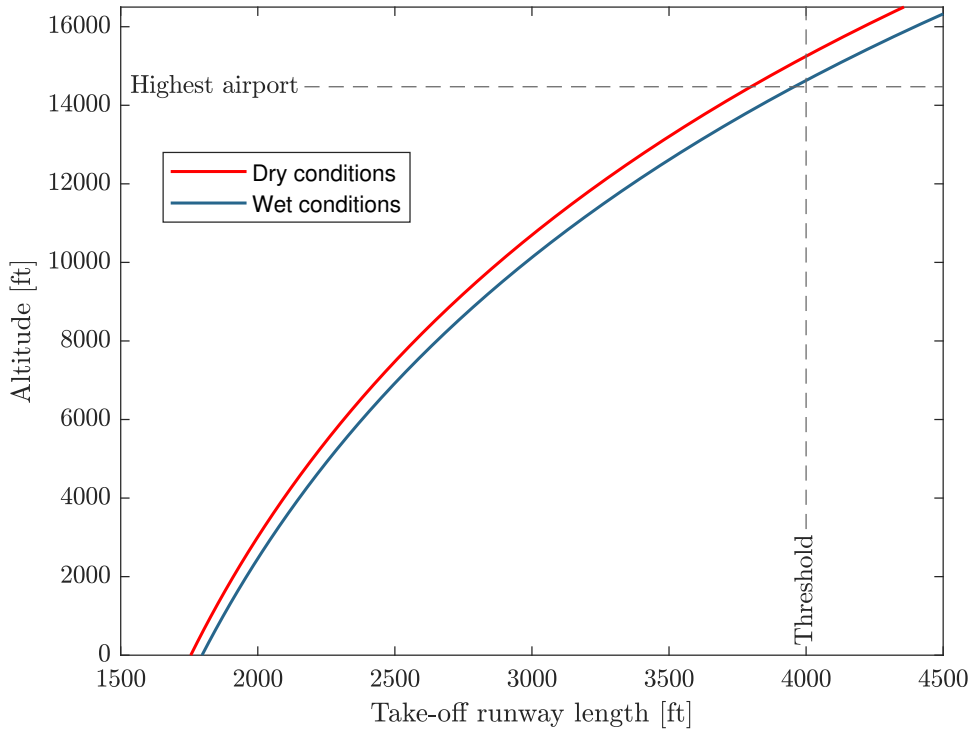| Runway condition	Take-off distance (sea level) [ft]	Take-off distance (5000 ft) [ft]
Dry	1755	2199
Wet	1797	2261

BeLI

Figure 7.28: Evolution of the take-off distance with respect to altitude for both dry and wet conditions, computed without BLI.

It is retrieved from Figure 7.28 that the maximum altitude at which the BELI can take off in wet conditions (14630 ft) to respect the threshold is greater than the altitude of the highest airport, namely Daocheng Yading Airport (14472 ft) [41]. The BELI, therefore, respects the runway length threshold of 4000 ft in any circumstances. Moreover, since the take-off distance can be considered as only the ground roll distance, the BELI respects the objective at sea level with said distance of 1471 ft in wet conditions.

BLI enhanced performance

Table 7.24 presents improvements of the take-off performance of the BELI due to BLI. The take-off distance is considered to be for wet conditions. As it can be observed, BLI allows the aircraft to take-off more rapidly and extend its maximum take-off altitude.

Table 7.24: Summary of take-off performance of the BELI considering different drag reduction due to BLI in terms of mean μ and standard deviation σ values. New values and absolutes changes (%) are both provided.

Percentage of drag reduction thanks to BLI [%]	$\mu - \sigma$ 7.34	μ 9.52	$\mu + \sigma$ 11.7	$\mu + 2\sigma$ 13.88
Take-off distance (sea level) [ft]	1785 (-0.7%)	1782 (-0.8%)	1779 (-1%)	1776 (-1.2%)
Maximum take-off altitude [ft]	14790 (+1.1%)	14840 (+1.4%)	14880 (+1.7%)	14930 (+2.1%)

7.4.2 Climb

General considerations

After take-off, the BeLI is expected to climb to a cruise altitude of 30000 ft. The climb diagram representing this phase is described in Figure 7.29.

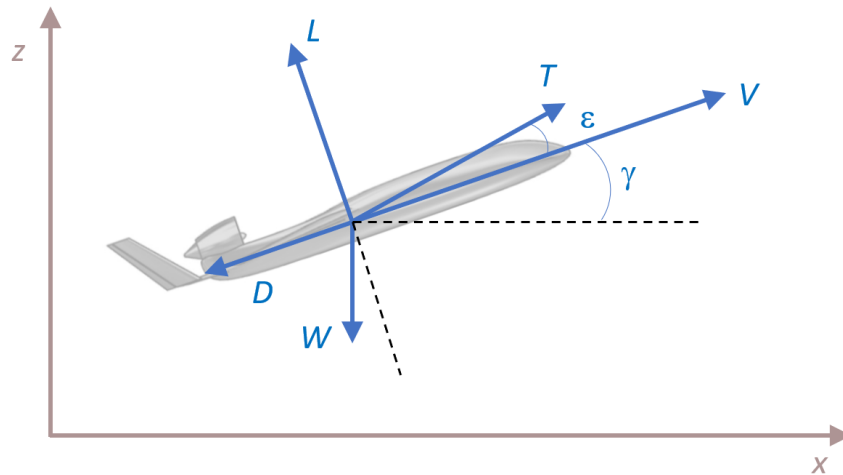Figure 7.29: Climb diagram.

It is assumed that the velocity V is aligned with the thrust T, hence $\varepsilon = 0$.

The climb phase is governed by the two following equations [12]:

$$T = 0.5\rho C_D V^2 S + W\sin\gamma \; ; \tag{7.40}$$

$$W\cos\gamma = 0.5\rho C_L V^2 S \; . \tag{7.41}$$

A few assumptions are taken:

- the climb angle γ remains small;

- the drag is considered parabolic;

- the maximum thrust available is taken in order to quantify BeLI performance.

The rate of climb ROC is then defined as

$$ROC = \frac{TV - 0.5\rho C_D V^3 S}{W}. \tag{7.42}$$

By solving both equations for different speeds and altitudes, the evolution of the climb rate with respect to the altitude and equivalent airspeed can be computed. Results are shown in Figure 7.30 for the rate of climb ROC and in Figure 7.31 for the angle of climb AOC.
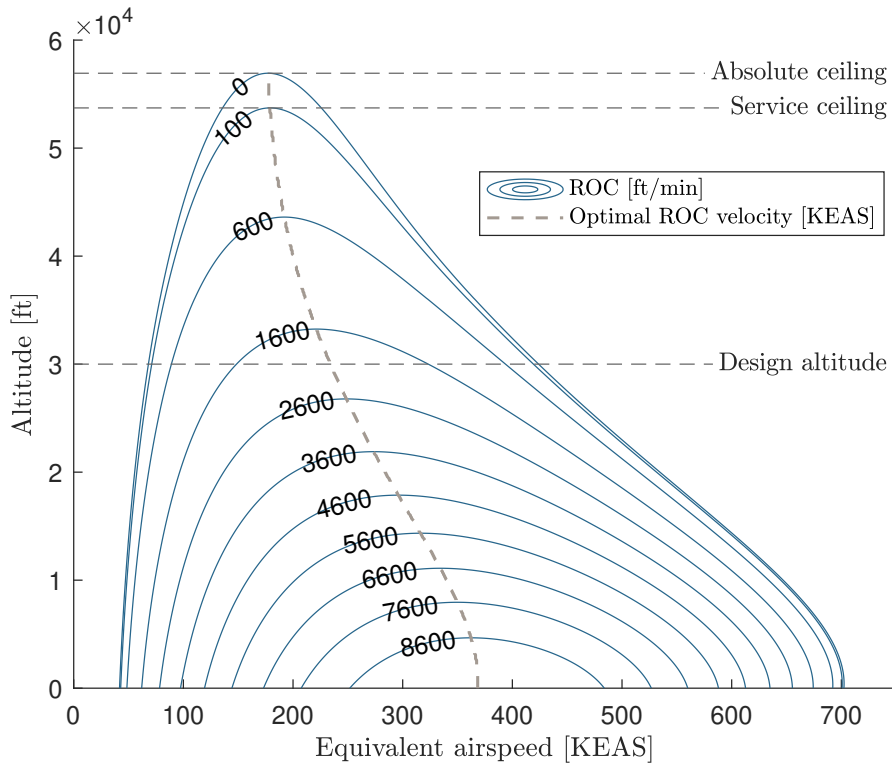
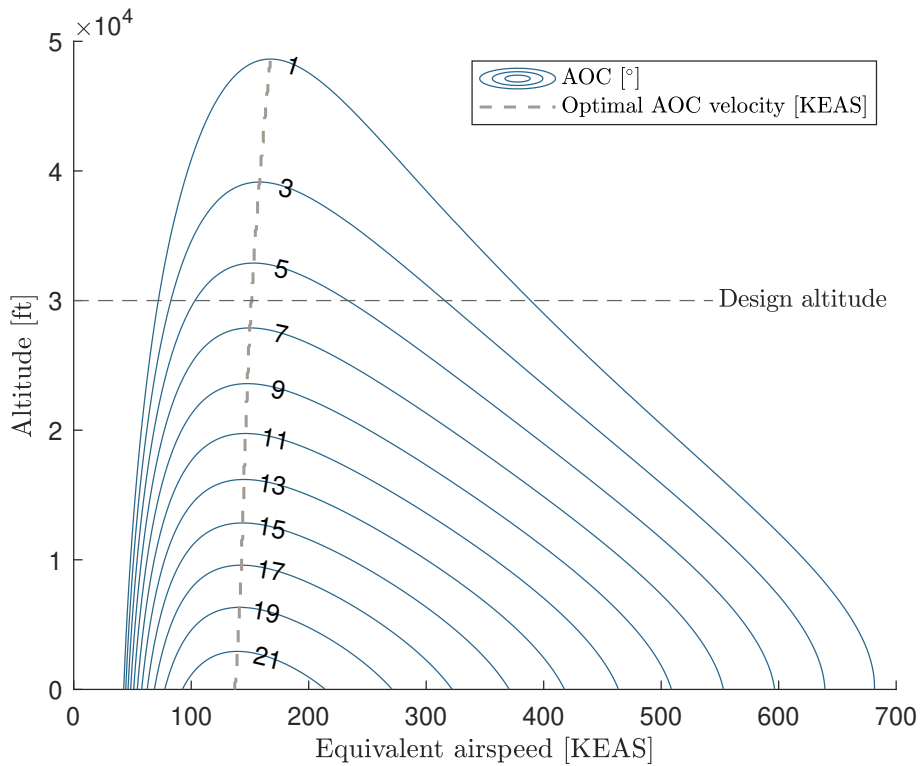Figure 7.30: Isocurves of the achievable rate of climb of the BeLI and ceilings altitude, computed without BLI.

Figure 7.31: Isocurves of achievable climb angle of the BeLI, computed without BLI.

Ceiling altitudes can be retrieved from Figure 7.30. The absolute and service ceiling altitudes of 56930 ft and 53720 ft are respectively defined as the highest altitude for a climb rate of 0 and 100 ft/min. The maximum rate of climb $ROC_{max} = 9176$ ft/min and associated velocity $V_Y = 368.4$ KEAS and angle of climb $\gamma_Y = 15.1°$ are also derived from Figure 7.30. Similarly, the maximum angle of climb $\gamma_{max} = 22.6°$ and associated velocity $V_X = 137.1$ KEAS and rate of climb $ROC_X = 5325$ ft/min are retrieved from Figure 7.31. The maximum rate and angle of climb are both achieved at sea level.

The time required to climb to cruise altitude and the associated horizontal distance covered can be computed from previous results as follow:

$$t_{climb} = \int_0^h \frac{dh}{ROC(h)}; \tag{7.43}$$

$$x_{climb} = \int_0^{t_{climb}} \frac{ROC(h)}{tan(\gamma)} dt. \tag{7.44}$$

Two approaches are then taken. One consists in climbing at constant velocity V_Y while the second option is to climb at the optimal ROC velocity regarding the climb rate as expressed in Figure 7.30. The latter allows to determine the lower bound for the time and distance of the climb phase. Results are summarized in Table 7.25.

Table 7.25: Time to climb to design cruise altitude and distance covered, computed without BLI.

	Optimal ROC velocity	V_Y
t_{climb} [min]	6.6	8.4
x_{climb} [nm]	31.5	51.0

BLI enhanced performance

Table 7.26 presents improvements of the climb performance of the BELI due to BLI. The time to climb considered is the one for which the optimal speed is assumed. As it can be seen, BLI allows the aircraft to climb more rapidly and reach higher maximum rate and angle of climb.

Table 7.26: Summary of climb performance of the BELI considering different drag reduction due to BLI in terms of mean μ and standard deviation σ values. New values and absolute changes (%) are both provided.

Percentage of drag reduction thanks to BLI [%]	$\mu - \sigma$ 7.34	μ 9.52	$\mu + \sigma$ 11.7	$\mu + 2\sigma$ 13.88
ROC_{max} [ft/min]	10009 (+3%)	10103 (+4%)	10201 (+5%)	10302 (+6%)
t_{climb} [min]	6.4 (-3.1%)	6.3 (-4.5%)	6.27 (-5%)	6.2 (-6.1%)
γ_{max} [min]	22.63 (+0.1%)	22.65 (+0.2%)	22.67 (+0.3%)	22.69 (+0.4%)

BeLI

7.4.3 Turn

General considerations

The turn diagram is described in Figure 7.32.
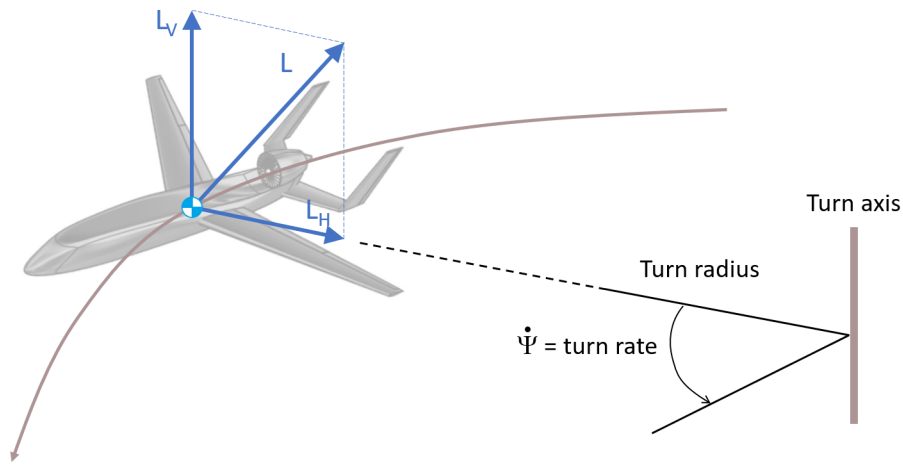
Figure 7.32: Turn diagram.

In order to withstand the turn, the load factor due to the centripetal force has to remain below the maximum load factor $n_{max} = 3$. Moreover, the maximum thrust available and the stall condition limit the performance of the turn phase.

The energy-maneuverability diagram of the BeLI, represented in Figure 7.33, allows to describe the relationship between the turn rate $\dot{\psi}$ and the equivalent airspeed [12].

Figure 7.33: Energy-maneuverability diagram of the BeLI (turn performance), computed without BLI.

The constant radii turn curves are expressed as

$$\dot{\psi} = \frac{V}{R} \tag{7.45}$$

while on the other hand, the constant load factor turns are given by

$$\dot{\psi} = \frac{g\sqrt{n^2 - \cos\gamma}}{V}. \tag{7.46}$$

For level turn, it simplifies thanks to $cos(\gamma) = 1$. As stated previously, the turn rates are limited by the maximum load factor, the maximum thrust available but also the stall limit as
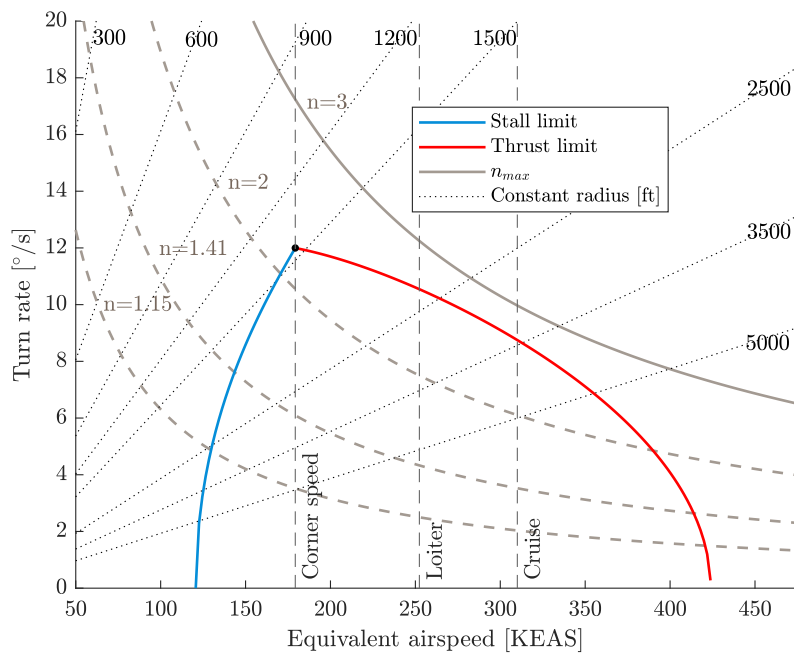
$$\dot{\psi} = \frac{g\sqrt{(\frac{\rho S C_{Lmax} V^2}{2mg})^2 - 1}}{V}. \tag{7.47}$$

The maximum turnrate $\dot{\psi}_{max}$, bank angle ϕ_{max}, load factor n_{max} and minimum radius R_{min} achievable in cruise and loiter conditions are summarized in Table 7.27.

Table 7.27: Relevant quantities of the turn phase, computed without BLI.

	Loiter	Cruise
$\dot{\psi}_{max}$ [°/s]	10.6	8.8
ϕ_{max} [°]	22.3	21.9
n_{max} [g]	2.63	2.68
R_{min} [ft]	2315	3425

Finally, the minimum radius and maximum turn rate are achieved at a corner speed of 179.3 KEAS. Their values are respectively 1445 ft and 12°.

BLI enhanced performance

Table 7.28 presents improvements in the turn performance of the BELI due to BLI for the main relevant quantities. Said quantities are expressed for loiter conditions for which turn performance has the most significance. BLI enables tighter turns to be taken with an increased load factor which nonetheless remains lower than the maximal value admissible.

Table 7.28: Summary of turn performance of the BeLI considering different drag reduction due to BLI in terms of mean μ and standard deviation σ values. New values and absolute changes (%) are both provided.

Percentage of drag reduction thanks to BLI [%]	$\mu - \sigma$ 7.34	μ 9.52	$\mu + \sigma$ 11.7	$\mu + 2\sigma$ 13.88
$\dot{\psi}_{max}$ [°/s]	10.8 (+1.9%)	10.8 (+1.9%)	10.9 (+2.8%)	11.0 (+3.8%)
n_{max} [g]	2.67 (+1.5%)	2.69 (+2.3%)	2.70 (+2.7%)	2.72 (+3.4%)
R_{min} [ft]	2266 (-2.1%)	2252 (-2.7%)	2239 (-3.3%)	2225 (-3.9%)

7.4.4 Dash speed

General considerations

The dash speed of an aircraft is achieved when using the maximum thrust permitted by the propulsion system. This is computed at the cruise level. Dash speed is not sustainable and is only expected to be used for a short time, if not used at all. The objective is to achieve an M=0.9 dash Mach number for the BeLI.

Starting from the relation between the drag and the thrust at cruise level:

$$D = 0.5\rho_\infty V_\infty^2 S C_D = T_{max}(M) \tag{7.48}$$

the dash speed V_∞ can be computed thanks to the maximum thrust applied T_{max}. This is however not straightforward since said maximum thrust depends on the speed itself [25]. The system is thus solved iteratively and a dash speed corresponding to **M = 0.99** is finally obtained, hence verifying the objective. Even though compressibility effects are neglected (C_D is considered as a constant), the difference is such that the objective of dash speed is sure to be achieved. In a spirit of consistency, the dash speed of the BeLI is taken as **M = 0.9** to be more realistic for future computations.

BLI enhanced performance

The dash speed of the BeLI is obviously greater when drag is decreased and BLI therefore allows to increase its value. However, as stated previously, giving a precise value would not be realistic and consistent since compressibility effects are not considered in Equation 7.48. BLI is nonetheless expected to increase the dash speed to an extent.

7.4.5 Range analysis

General considerations

Payload-range diagrams—elbow charts—express the trade-off inherent between payload and range for an aircraft.

Figure 7.34 and Figure 7.35 describe the payload-range diagram of the BELI respectively for cruise and loiter conditions.
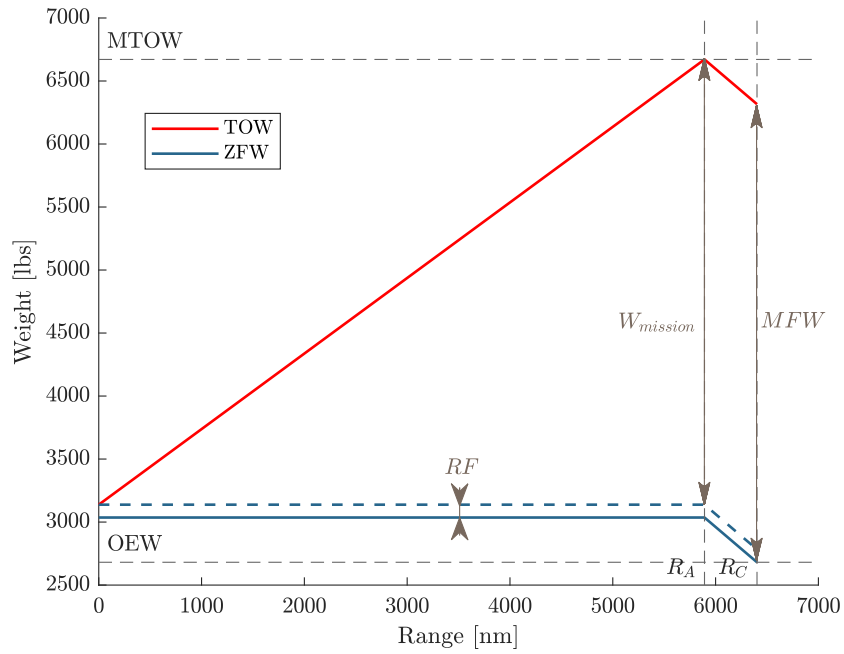

Figure 7.34: Payload-range diagram of the BELI in cruise condition, computed without BLI.
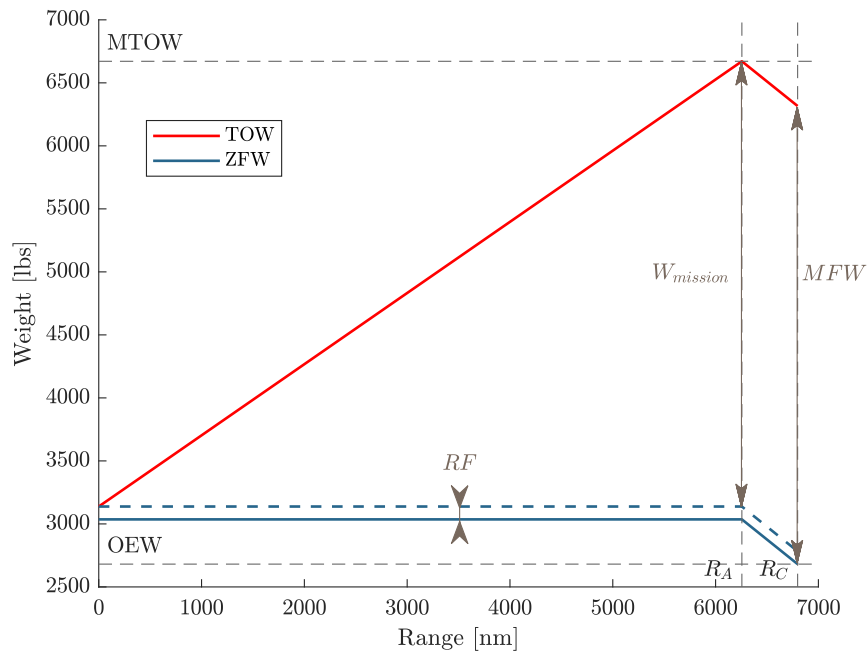

Figure 7.35: Payload-range diagram of the BELI in loiter condition, computed without BLI.

Since it is more meaningful to express loiter in terms of hours, the loiter ranges R_A and R_C in Figure 7.35 correspond respectively of loiter times of 15.2 h and 16.5 h.

The top black dotted horizontal line represents the maximum take-off weight MTOW. On the other hand, the bottom black dotted horizontal line represents the operational empty weight OEW. The maximum transported payload is the difference between the maximum zero-fuel weight MZFW, the blue line, and OEW. The reserve fuel RF is also represented. By going from left to right, the maximum payload is seen to stay constant as the range increases. Hence, more fuel needs to be added for more range as described by the take-off weight TOW curve.

The first dotted vertical line represents the range R_A at which the sum of the operational empty weight, maximum payload, and required fuel reaches the maximum take-off weight of the aircraft. Making use of Breguet equation [9], it is found that

$$R_A = \frac{V}{TSFC}\frac{C_L}{C_D}\log(\frac{MTOW}{OEW+MPL+RF}) \ . \tag{7.49}$$

If the range is desired to be increased above that point, the payload has to be sacrificed in return for more fuel. The maximum range R_C corresponds thus to

$$R_C = \frac{V}{TSFC}\frac{C_L}{C_D}\log(\frac{OEW+FW}{OEW+RF}) \ . \tag{7.50}$$

It must be noted that the maximum fuel capacity of the BeLI has been designed to be exactly equal to the fuel required to perform the maximum range mission (including reserve fuel).

Those results also provide in a sense the achievable ranges for the secondary missions consisting respectively of only cruise and only loiter flights.

Regarding the maximum range achievable by the BeLI for the primary mission, the Breguet equation is once more applied for each phase of the mission.

Table 7.29 shows the maximum ranges expected of the BeLI for the different phases of its primary mission.

Table 7.29: BeLI primary mission ranges, computed without BLI.

Ingress cruise	Loiter	Egress cruise
850 nm	5 h	2000 nm

Each objective is seen to be achieved by the BeLI even without BLI influence. This is not unexpected since the BeLI was designed in order to verify them in the case where BLI would not have any beneficial effect.

BLI enhanced performance

Ranges R_A and R_C of the previous payload-range diagram are computed again for cruise and loiter with the influence of the BLI. It is assumed that the reduction of drag due to BLI followed a Gaussian distribution of previously defined

mean μ and standard deviation σ. The probabilistic distribution of the ranges in cruise and loiter are respectively shown in Figure 7.36 and Figure 7.37.
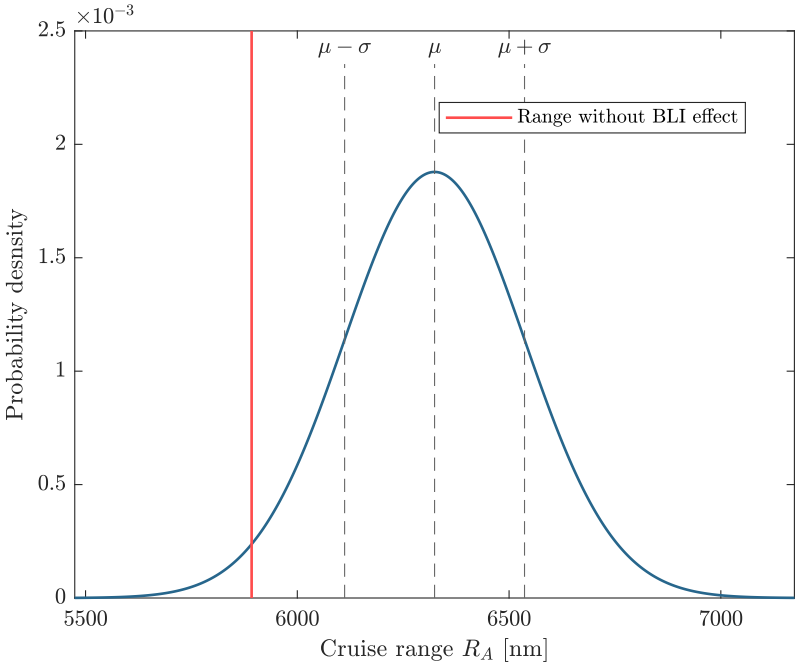
Figure 7.36: Gaussian distribution of the range of the BELI in cruise associated to a normal distribution of drag reduction due to BLI.
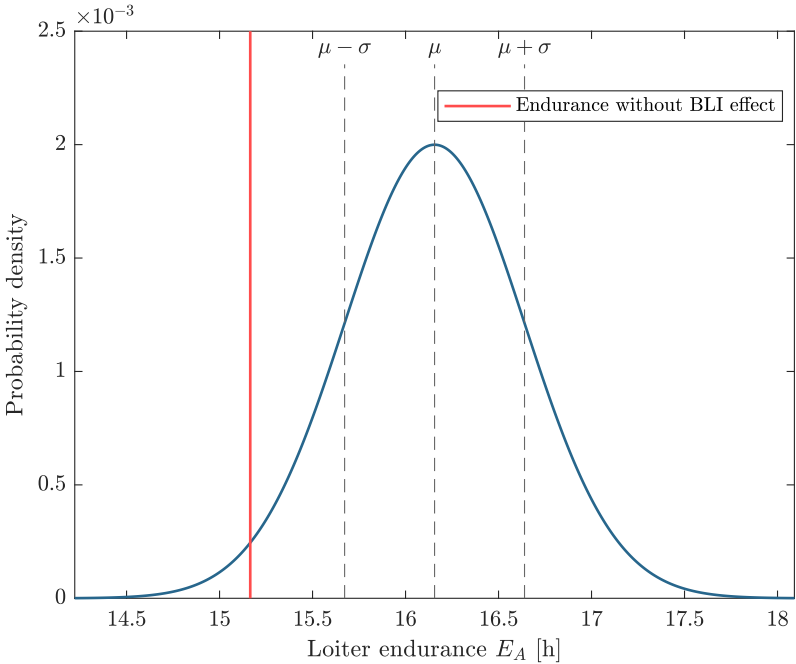
Figure 7.37: Gaussian distribution of the endurance of the BELI in loiter associated to a normal distribution of drag reduction due to BLI.

Finally, ranges performance of the BELI for the primary mission are computed again and shown in Table 7.30 by considering the mean drag reduction expected due to BLI.

Table 7.30: BELI primary mission ranges considering mean reduction of drag thanks to BLI compared to the objectives.

Ingress cruise [nm]	Loiter [h]	Egress cruise [nm]
960 > 850	5.3 > 5	2110 > 2000

By considering that all the saved fuel is used in order to increase the time of loiter over the objective site, the loiter time can go up to 6 hours. From another perspective, fuel savings due to BLI, if the BELI does not go beyond the objectives, correspond to 105 lbs. The BELI is therefore seen to be more ecological and versatile than the competition, being able to expand its boundaries to cover more land and reach more people.

7.4.6 Descent

Since the BELI is an unmanned vehicle, a great rate of descent can be considered. It is assumed that the descent is first achieved with a 5000 ft/min rate of descent at the beginning of the phase. It is assumed to consider this high rate of descent until 3000 ft since landing gears are usually lowered largely before the landing to prevent any issues. Then, the rate of descent is chosen to match landing conditions (angle of descent and velocity). Using relations similar to the climb phase, the time of descent is thus expected to be around 12 min with a distance covered of 31 nm.

7.4.7 Glide

Due to the high attritability of the mission, the glide performance of the BELI is of high interest. The methodology followed is expressed hereunder [9].

The best glide velocity is given by

$$V_{BG} = \sqrt{\frac{2W}{\rho S} \sqrt{\frac{1}{C_{D0} e \pi AR}}}. \tag{7.51}$$

With the maximum lift-to-drag ratio given by

$$\left(\frac{L}{D}\right)_{max} = \left(\sqrt{\frac{4C_{D0}}{e \pi AR}}\right)^{-1}, \tag{7.52}$$

the glide distance can be computed as

$$R_{glide} = h \cdot \left(\frac{L}{D}\right)_{max}. \tag{7.53}$$

The rate of descent ROD can finally be expressed as

$$ROD = V_{BG} \cdot \sin\left(\text{atan}\left(\frac{h}{R_{glide}}\right)\right). \tag{7.54}$$

Table 7.31 summarizes glide performance of the BELI.

Table 7.31: Glide performance of the BELI, computed without BLI.

V_{BG}	$(\frac{L}{D})_{max}$	R_{glide}	ROD
244.4 ft/s	4.58	22.6 nm	3142 fpm

The assessment of glide performance is of great significance since the harsh environment might cause engine failure of the BELI. This glide distance value would therefore make it possible to get further away from inhabited areas.

7.4.8 Landing

Similarly to the take-off, the BELI is expected to land within a 1500 to 4000 ft runway length, still considering a clearance height of 30 ft. The landing is performed in successive stages as described in Figure 7.38
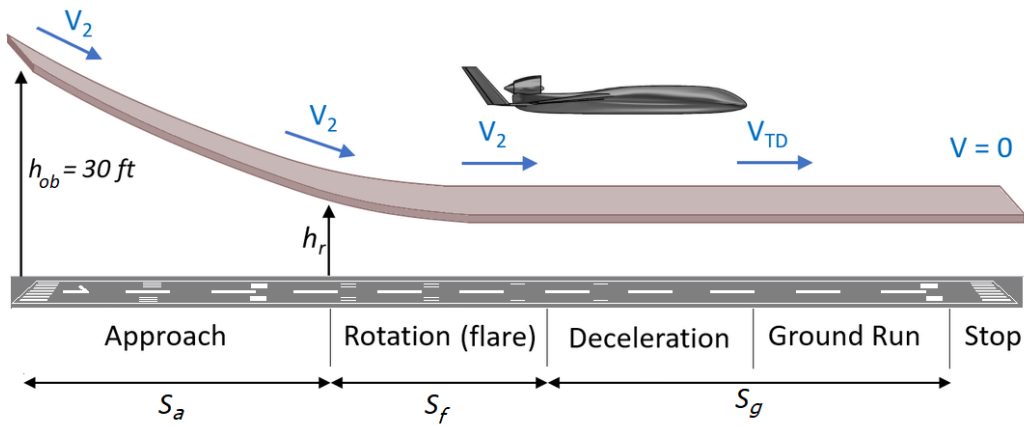
Figure 7.38: Landing stages retrieved from [12].

The methodology followed is the one of the Gudmundsson [12]. First, the approach distance S_a from the clearance height of 30 ft to the flare rotation at an angle γ is computed,

$$S_a = \frac{h_{ob} - h_r}{\tan\gamma} \ , \tag{7.55}$$

with

$$h_r = 0.1512 \cdot V_2^2 (1 - \cos\gamma) \ . \tag{7.56}$$

The angle of approach γ is assumed to be 3 degrees [9] [12]. This approach is performed at a constant velocity V_2 of

$$V_2 = 1.3 \cdot V_{stall} \ , \tag{7.57}$$

where it must be noted that this stall velocity is different from the take-off configuration with the deflection of the flaps. The rotation or flare stage then describes a circular arc motion.

The flare distance S_f can be approximated by [12]

$$S_f = V_2^2 \cdot \sin\gamma \cdot 0.1512 \ . \tag{7.58}$$

Finally, the ground run distance S_g consists in decelerating from V_2 to 0:

$$S_g = \frac{V_2^2}{2\overline{a}} \ . \tag{7.59}$$

The overall deceleration for small aircraft with simple brakes can be statistically estimated as $0.35 \cdot g$ [8]. The total landing distance is the sum of the approach, flare, and ground distances and thus equals **1421 ft**, which respects the objective on the landing distance.

7.4.9   Fuel analysis
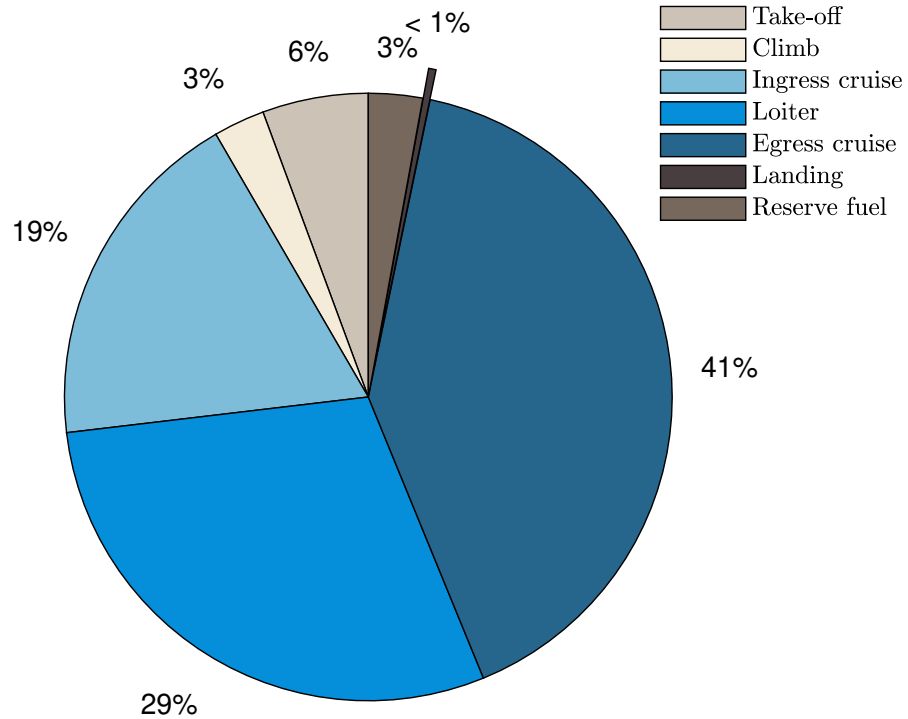
The fuel partition of the BeLI is depicted in Figure 7.39.

Figure 7.39: Fuel partition of the BeLI for the primary mission.

The fuel required for the take-off (W_{to}), climb (W_{climb}) and landing (W_{la}) phases are approximated by the following relations [9]:

$$W_{to} = 0.03 \cdot MTOW \ ; \tag{7.60}$$

$$W_{climb} = 0.015 \cdot (MTOW - W_{to}) \ ; \tag{7.61}$$

$$W_{la} = 0.005 \cdot \frac{(OEW + RF)}{0.995} \ . \tag{7.62}$$

The fuel consumed during the descent phase is neglected [9].

From the total fuel volume $V_f = 549.5$ gal (including reserve fuel), the time t required to refuel totally the BELI can be derived by considering a classic refuel mass flow rate $\dot{m}_f$ of 634 gallons per minute [42]:

$$t = \frac{V_f}{\dot{m}} = \frac{m_f}{\rho \dot{m}} = 52 \ \text{s} \tag{7.63}$$

with the fuel mass $m_f = 3635$ lbs and the density of the fuel $\rho = 6.68$ lbs/gal. A classical JET A fuel is considered. The objective is therefore respected (KPPs).

Finally, the engine nacelle is easily accessible from the back of the aircraft and an access hatch can be installed in order to replenish engine start consumables within five minutes (KPPs).

BeLI

8 Cost analysis

The objective of this section is to provide an estimation of the different costs associated with the development, production and operations of the BeLI. For this purpose, a modified version of the DAPCA-IV method for general aviation was implemented. This method establishes different cost estimating relationships (CERs) to predict the aircraft acquisition costs using information such as the empty weight and the maximum airspeed. A detailed description of this approach provided by Gudmundsson [12] was used to perform this analysis. However, a fudge factor was taken into account due to the BLI implementation. It should also be noted that all the costs presented in this section were established following the FAA 4 CFR Part 23 certification, as previously mentioned.

In order to estimate the different costs, the production rate must first be determined. It is assumed that 8 aircraft per month will be manufactured. In other words, approximately 500 aircraft will need to be produced over a five-year period. This number seems reasonable considering that a year is composed of about 250 working days.

Finally, it should be noted that the DAPCA-IV method takes into account the cost of living using the consumer price index (CPI). However, the different CERs presented by Gudmundsson [12] are based on the year 2012. Therefore, the relationships must be adjusted to the year 2028, when the BeLI is expected to be operational. For this purpose, the CPI data from the Bureau of Labor Statistics [43] from 2012 to 2023 were first collected. To obtain an approximate value for the CPI in 2028, a linear interpolation on the data from 2012 to the December 2019 was then performed. The economic situation due to the COVID-19 crisis have caused the inflation to skyrocket in the last few years, leading to a significant increase in the CPI. However, some experts agree that these effects are only transitory and that a pre-pandemic situation could be restored in the long term [44][45][46]. Hence, it seems reasonable to ignore the years from 2020 to 2023 in order to obtain a relevant price for 2028. The results are presented in Figure 8.1. As it can be observed, the ratio between CPI of 2028 and 2012 is about 1.4 ($= \dfrac{CPI_{2028}}{CPI_{2012}}$). As a consequence, each CER are multiplied by this factor.
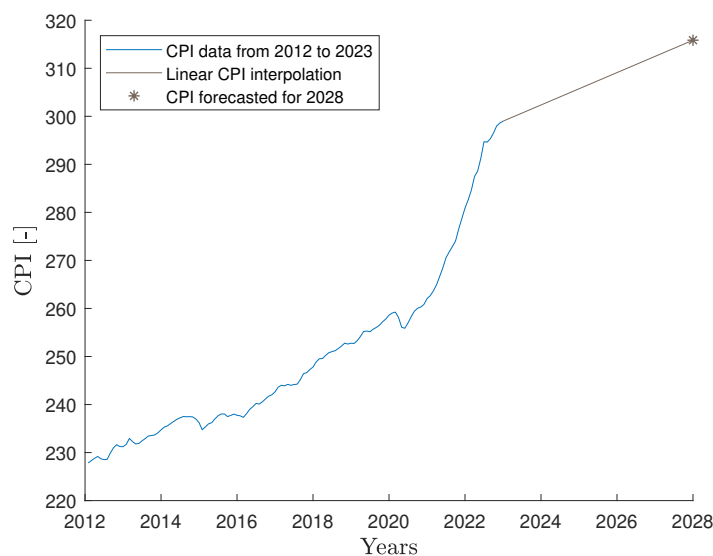

Figure 8.1: Consumer price index (CPI) evolution and linear interpolation [43]

8.1   Non-recurring costs

The non-recurring development costs correspond to the total fixed costs required to develop and produce the BELI. More precisely, these costs are related to the engineering, tooling, development support and flight test operations. Their distribution per aircraft is represented in Figure 8.2. It should be noted that the costs of development support and flight test operations are listed under the name "others" in order to make Figure 8.2 more readable. These are worth $24,676 and $5,169 per aircraft, respectively.
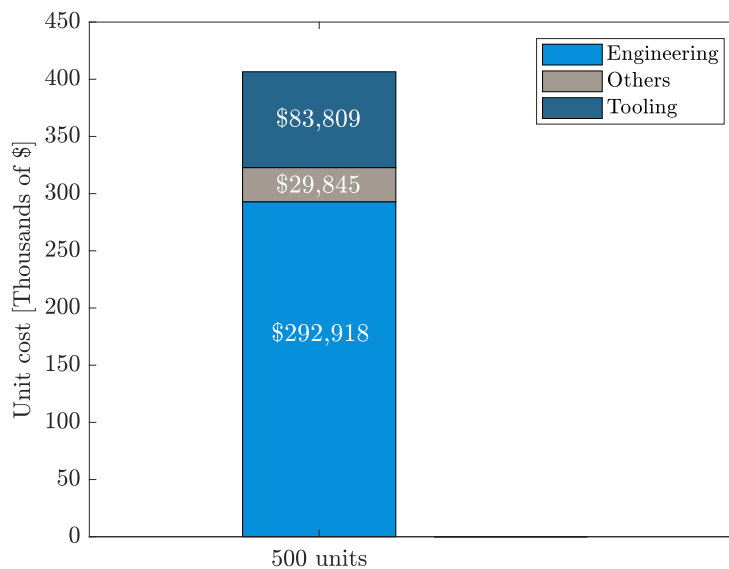

Figure 8.2: Unit non recurring costs of the BELI in thousands of dollars.

In order to compute the non-recurring costs, the engineering and tooling wage per hour had to be considered. These were fixed at $92 and $61 per hour, respectively. Such values were chosen to match typical 2012 salaries for these fields in the United States [12]. However, these values still need to be adjusted by the CPI factor to correspond to the year 2028, as stated above. In addition, the DAPCA-IV method requires fixing a certain number of prototypes. The choice of this number is quite arbitrary as it depends on many factors such as the timeline, budget, risk management,...

Therefore, it was decided arbitrarily that five models of the BELI would be produced. This choice should neither increase excessively the cost, nor delay the commissioning of the aircraft but should guarantee that it will be able to effectively fulfill its mission when it is put into operation. It must be noted that, as mentioned above, parameters corresponding to the design and performance of the aircraft were also considered to enable the implementation of the DAPCA-IV method.

8.2 Fly away costs

The fly away costs correspond to the production costs required for each additional aircraft. These include manufacturing efforts, quality control, materials/equipment, engine and avionics costs. Their distribution per aircraft is shown in Figure 8.3. It should be noted that the costs of quality control and avionics are listed under the name "others" in order to make Figure 8.3 more readable. These are worth $64,476 and $25,254 per aircraft, respectively.
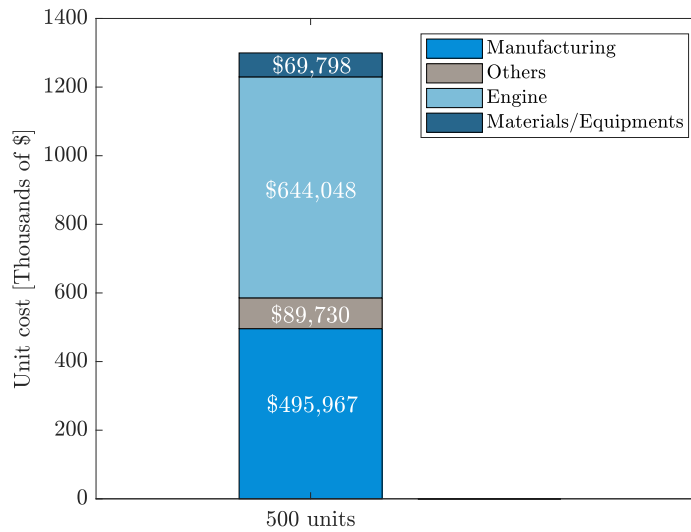

Figure 8.3: Unit fly-away costs of the BELI in thousands of dollars.

In order to calculate the flyaway costs, the manufacturing wage per hour had first to be considered. This was set to $53 per hour. As before, such a value was chosen to correspond to a typical 2012 salary for this field in the United States [12]. However, this value still needs to be adjusted by the CPI factor to correspond to the year 2028, as stated above. Then, the avionics cost was fixed at $40,000 per aircraft. It is worth noting that this value is higher than the one recommended by Gudmundsson (*i.e.*, $15,000) [12]. The BELI being an unmanned aircraft, it seems important to take into account the additional costs related to the remote control flight systems. Also, as it was the case for the non-recurring costs, parameters corresponding to the design and performance of the aircraft were considered to enable the implementation of the DAPCA-IV method. Finally, it should be noted that the cost of the engine was decreased by a factor of 10%. Such a choice was made to take into account the economies of scale due to the possible large orders that will be made to the manufacturer. In addition, it is reasonable to assume that the engine does not have to be characterized by the highest reliability, as is the case for commercial aircraft, since the BELI is expected to make very few flights (*i.e.*, 50) and that it does not transport any passengers. In other words, the probability of an accident occurring is much lower than with a conventional aircraft. However, given that the BELI must be able to fly in less than ideal conditions, reducing the cost by a factor greater than 10% does not seem realistic.

As suggested by the employed cost analysis method, a quantity discount factor (QDF) was applied to the avionics and engine costs. This parameter allows to take into account the efficiency gains as well as the economies of scale achieved throughout the production process. This variable being defined as

$$QDF = F_{EXP}^{1.4427 \cdot \log(N)},$$

with N the number of produced unit in a five-year period and F_{EXP} the experience effectiveness adjustment factor. The latter was set at 95% to correspond as closely as possible to actual aircraft production as it was suggested by Gudmundsson [12].

8.3 Break-even analysis

The objective of this section is to perform a break-even analysis in order to determine the number of units to produce so that the total revenue equals the total incurred cost. In other words, once this number of units is produced, the company can expect to start making a profit. Using the standard cost-volume-profit-analysis, the expression of the break-even point can be determined as

$$N_{BE} = \frac{\text{Total fixed costs}}{\text{Unit selling price - Unit fly-away cost}}.$$

Since the costs have been determined in the previous two sections, all that remains is to establish the unit selling price. For this purpose, a liability insurance of 12% of the total cost was first considered. According to Gudmundsson [12], a typical value for this parameter lies between 12 and 17%. Since the BELI is expected to perform very few flights (*i.e.*, 50), the risk of an accident or other problematic event is low. Therefore, it does not seem necessary to make an excessive provision. However, given that the BELI must be able to fly in less than ideal conditions, going below 12% does not seem prudent. Then, a margin of 10% on the cost obtained with the liability insurance was considered to obtain the selling price. Such a value seems low for a commercial company since a typical value would be at least 15%. However, given that the purpose of the BELI is to rescue people and consequently to save lives, it seems that the company has a duty to embrace a more humanistic approach by taking only a 10% margin to contribute in a positive way to this world.

The resulting unit price, obtained with these values, is computed as **$2.1 million** for 500 units produced in a five-year period. As a consequence, the break-even point is reached when 340 units are produced. A representation of this analysis is presented in Figure 8.4.
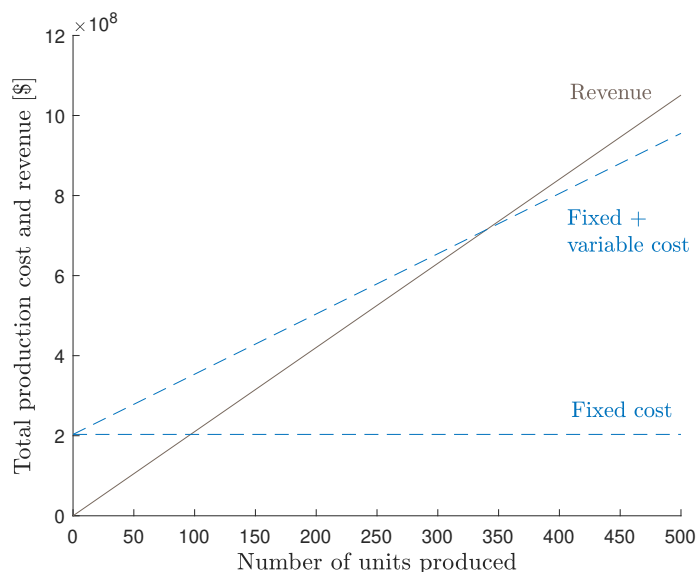
Figure 8.4: Break-even analysis of the BeLI.

8.4 Operating costs

The calculation of the operating costs is a crucial part of the analysis because these determine how economically viable it is to buy the aircraft. These include maintenance, storage, fuel, insurance and annual inspection costs. Their distribution is shown in Figure 8.5. It should be noted that the costs of storage and annual inspection are listed under the name "others" in order to make Figure 8.5 more readable. These are worth to $3000 and $750, respectively.

In order to calculate the operating costs, the number of flight hours per aircraft had first to be determined. This was set at about 500 hours. Such a value was calculated by assuming an extreme case where the BeLI would have to perform each of these 50 flights with a maximum range (*i.e.*, 5250 nmi). Taking into account the typical cruise speed of this aircraft, it is reasonable to suppose that this kind of mission takes about 10 hours. Therefore, by multiplying the 50 flights by 10 hours, this value can be approximated by 500 hours. It should be noted that this assumption is also consistent with the typical values described by Gudmundsson (*i.e.*, between 100 and 1000 hours/year) [12]. Also, the maintenance wage per hour was fixed to $53 per hour. As before, such a value was chosen to correspond to a typical 2012 salary for this field in the United States [12]. However, this value still needs to be adjusted by the CPI factor to correspond to the year 2028, as stated above. In addition, the fuel price was set at $4/gallon and was selected to reflect an average price in the United States [47]. On the other hand, the cost of the insurance was calculated at the amount of the selling price of the aircraft, as it was suggested by Gudmundsson. Finally, it should be noted that cost of the engine overhaul fund was neglected. Since the BeLI is expected to perform very few flights, the engine does not have to be characterized by the highest reliability, as it was already mentioned above. Therefore, it seems reasonable to not perform regular engine overhauls. However, it was decided that a more strict annual inspection should be carried out. Such a choice was made because it is still necessary to

guarantee that the engine is operating properly, but also because the BeLI must be able to fly in less than ideal conditions. Not upgrading the annual inspection does not seem realistic. Therefore, this cost is set at $750 per year. This value is higher than the one suggested by Gudmundsson, which is $500 [12].

Using all these assumptions, the cost per flight hour and per aircraft can be determined. This one is around **111$/h**. In addition, it seems important to note that a saving of $751 can be achieved on the total cost of each aircraft flight with the BLI implementation. This value was obtained by still considering the Gudmundsson equations [12] and by assuming that the ratio between the thrust generated with and without BLI is 93.17% by applying the mean reduction of drag as explained in Section 6.4.1. As it can be observed, the primary characteristic of the BeLI provides yet another advantage.

It should be noted that the costs stated above are only valid for a single aircraft. However, it is reasonable to assume that a fleet of aircraft should be used in order to multiply the number of missions that can be performed simultaneously, and hence to be able to save more people. Therefore, the cost analysis was extended. More precisely, the operational costs for the twentieth and hundredth aircraft in a fleet were determined. For these, the cost of maintenance and insurance were reduced by an arbitrarily chosen factor. The latter amounts 10 and 20% for the twentieth and hundredth aircraft, respectively. This results in an operational cost of $103 and $95 per flight hour. It seems reasonable to assume that the customer will perform the BeLI maintenance on an assembly line and that the insurance cost per aircraft is lower for a larger fleet. The results are shown in Figure 8.5.
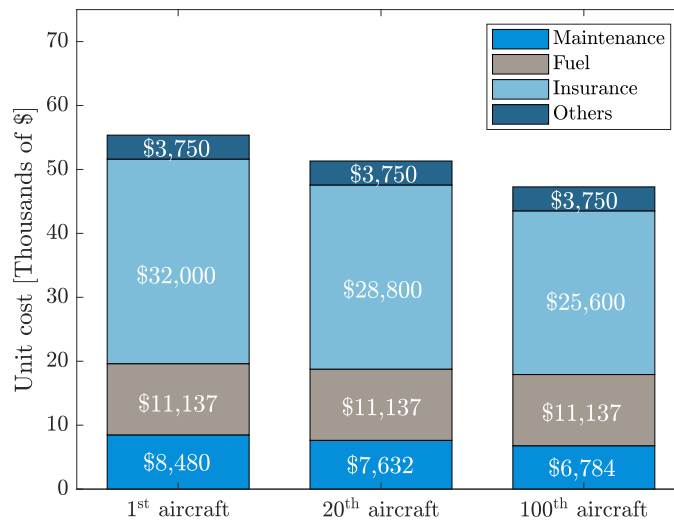

Figure 8.5: Yearly operating costs of the BeLI in thousands of dollars.

In order to ensure the competitiveness of the BeLI, it is also necessary to determine the operational cost required to save one person. The latter can be computed by taking the yearly costs shown in Figure 8.5 and by considering the fact that the BeLI is expected to perform 50 sorties. In addition, it should be recalled that the payload of the BeLI is able to help a minimum of 36 people per flight, as mentioned in Section 6.7. If the aircraft is assumed to perform a total of 50 flights in one year and that it is able to rescue 36 people per mission, it follows that the cost

to save one person is \$31 for the first aircraft of a fleet, \$29 for the twentieth and \$26 for the hundredth. However, it is worth noting that such values seem highly unlikely to be achieved but can be considered as an ideal case. Since it is reasonable to think that a fleet of the BELI will be used to perform the missions, a more realistic value was computed. In 2021, approximately 100 severe natural disasters occurred in the United States [48][49]. If a fleet of 20 aircraft is arbitrarily assumed, it is reasonable to consider that each of them will operate 5 missions every year. If it is assumed that the BELI will be able to save 36 people per flight, it results that the cost to save one person is approximately \$285.

9 Trade-off study

A trade-off study on the aspect ratio of the wing is performed by varying its value by ±10% to ensure the BeLI design optimality. In order to draw a consistent comparison, all three configurations have to be made stable. The variation of the MTOW is found negligible. Table 9.1 hereafter presents the result of the trade-off.

Table 9.1: Trade-off on the aspect ratio of the wing justifying BeLI design. Positive effects are denoted in green while negative ones are in red. All impacts are expressed in percentage of variation.

Wing AR [-]	-10%	BeLI	+10%
Take-off length [ft]	-4.5%	1797	+3.5%
Landing length [ft]	-5.6%	1421	-0.03%
Maximum take-off altitude [ft]	+4.6%	14630	-4.3%
Best rate of climb [ft/min]	-0.5%	9716	+1.2%
Climb distance [nm]	+1.0	31.5	-1.0
Loiter maximum turnrate [°/s]	-6.7%	10.6	+5.8%
Loiter minimum turn radius [ft]	+6.6%	2315	-6.0%
Fuel mass for the primary mission [lbs]	+7.6%	3533	+5.5%

An increase of the aspect ratio leads, *ceteris paribus*, to an increase of the lift to drag ratio, an increase of the parasitic drag and on the other hand a decrease in the induced drag. However, each configuration has been made stable and therefore the overall geometry slightly differs from the reference one to ensure said stability. It can clearly be seen that a decrease of the aspect ratio leads to worse performance except in take-off and landing phases. However, the fuel and maneuvers performance are weakened without any added value due to the transformation of a threshold into an objective. On the opposite, an increase of the aspect ratio appears first to be a better solution for maneuvers without not so high drawbacks in take-off or landing performance. The fuel mass is nevertheless also increased and subsequently the range is negatively affected. Since it is the main concern of the BeLI, an increase of aspect ratio is rejected too. Moreover, a larger aspect ratio would increase the bending moment the wing undergo which is tedious in a structural point of view. It also makes the aircraft more difficult to store. The aspect ratio of the BeLI is seen to lie on the perfect range of values to achieve maximum range.

10 Conclusion

As an answer to the request for proposal of the AIAA and the growing need for Dr. SAAV in this ecological disaster era, the BELIevers presented the BeLI. This innovative and versatile aircraft taking advantage of the boundary layer ingestion is able to decrease its drag in order to cover more land with subsequently a fewer fuel consumption. Hence, this aircraft can be part of an ecological policy while ensuring excellent performance. Furthermore, beside the fact that the BeLI is an aircraft that is neither expensive to buy nor to operate, it is designed to rapidly reach devastated areas. With its high payload capacity and large operating range, the BeLI is the ultimate solution to prevent the loss of many lives. Whatever the competition does, the BeLI does it further, greener, better.

Firstly, the conceptual design of the BeLI was investigated. From the requirements, design choices of each main components of the aircraft has been made. A literature review ensuring the BeLI could take advantage of the boundary layer ingestion was then performed. The methodology followed afterwards consisted in an iterative process on the design of each component to respect the requirements. A trade-off study was also performed to optimize the aircraft geometry. The BeLI went from draft to thoroughly designed aircraft.

Secondly, the conceptual design gave way to the preliminary design. It consisted in an in-depth analysis of the aircraft with more precise tools. The structure was analysed using finite element method, a drag study was conducted and the aerodynamics of the wing was studied. Both static and dynamic stabilities were proven. Moreover, the performance of the BeLI for the different phases of the mission was studied. The different requirements are seen to be met by the BELIevers ' solution. A cost analysis was finally carried out in order to provide proof of a beneficial trade-off between the cost and the attritability of the mission.

The next step for the future of the BeLI and of those living in hazardous areas is to conduct an even more detailed study of its performance and to build a first prototype. By expanding the boundaries, the BeLI is able to reach further afield and save more lives. Yesterday's idea, tomorrow's solution.

References

[1] Center for Climate and Energy Solutions, "Hurricanes and climate change." URL: https://www.c2es.org/content/hurricanes-and-climate-change/. Last accessed 15 February 2023.

[2] E. Duffin, "Natural disasters in the u.s. - statistics & facts." URL: https://www.statista.com/topics/1714/natural-disasters/#topicOverview, November 2022. Last accessed 15 February 2023.

[3] Departments agencies of the Federal Government produced by the Office of the Federal Register (OFR) and the Government Publishing Office, "Electronic code of federal regulations." URL: https://www.ecfr.gov/current/title-14/chapter-I/subchapter-C/. Last accessed 16 February 2023.

[4] "Uav market." URL: https://www.marketsandmarkets.com/Market-Reports/unmanned-aerial-vehicles-uav-market-662.html?gclid=CjwKCAjwl6OiBhA2EiwAuUwWZZqQC2w5Ee6r9uMvHOnm5f4_hivRghlVpL1zjueWOsWF55_hZdOdfBoC8f4QAvD_BwE. Last accessed 25 April 2023.

[5] "Unmanned aerial vehicle (uav) market." URL: https://www.alliedmarketresearch.com/unmanned-aerial-vehicle-market-A09059#:~:text=The%20global%20unmanned%20aerial%20vehicle,with%20a%20CAGR%20of%2010.0%25. Last accessed 25 April 2023.

[6] "Worldriskreport 2022." URL: https://weltrisikobericht.de/wp-content/uploads/2022/09/WorldRiskReport-2022_Online.pdf. Last accessed 25 April 2023.

[7] F. A. et al., WorldRiskReport 2022. Bündnis Entwicklung Hilft, 2022.

[8] L. Noels, "Aircraft design - conceptual design." URL: http://www.ltas-cm3.ulg.ac.be/AERO0023-1/ConceptionAeroDesign.pdf, 2022.

[9] Daniel P. Raymer, Aircraft Design: A Conceptual Approach. Playa del Rey, California: Conceptual Research Corporation, 6 ed., 2018.

[10] M. H. Sadraey, Aircraft Design A Systems Engineering Approach. A John Wiley & Sons, Ltd., 2012.

[11] NASA, "The supercritical airfoil," 2004.

[12] S. Gudmundsson, General Aviation Aircraft Design: Applied Methods and Procedures. Butterworth-Heinemann, 2014.

[13] D. Scholz, "Aircraft design - lecture notes." URL: http://LectureNotes.AircraftDesign.org., 2015.

[14] E. Torenbeek, Synthesis of Subsonic Airplane Design. Martinus Nijhoff Publishers, 1982.

[15] N. Budziszewski, J. Friedrichs, "Modelling of a boundary layer ingesting propulsor." DOI: http://dx.doi.org/10.3390/en11040708, 2018.

[16] A. Uranga *et al.*, "Boundary layer ingestion benefit of the d8 transport aircraft." DOI: https://doi.org/10.2514/1.J055755. Last accessed 19 April 2023.

[17] D. Hall *et al.*, "Boundary layer ingestion propulsion benefit for transport aircraft." DOI: https://doi.org/10.2514/1.B36321. Last accessed 20 April 2023.

[18] A. Uranga *et al.*, "Analysis of the aerodynamic benefit from boundary layer ingestion for transport aircraft." DOI: https://doi.org/10.2514/1.J056781. Last accessed 21 April 2023.

[19] C. Kaminski, M. Kinze, "Design optimization of a boundary layer ingestion propulsion system for a long-range, high-altitude uav." URL: https://docplayer.net/227825888-Design-optimization-of-a-boundary-layer-ingestion-propulsion-system-for-a-long-range-high.html. Last accessed 16 February 2023.

[20] A. Yildirim *et al.*, "Performance analysis of optimized starc-abl designs across the entire mission profile." DOI: https://doi.org/10.2514/6.2021-0891. Last accessed 19 April 2023.

[21] T. G. Tillman *et al.*, "Aircraft system study of boundary layer ingesting propulsion larry hardin." DOI: https://doi.org/10.2514/6.2012-3993, 2012.

[22] "Military turbojet/turbofan specifications." URL: https://jet-engine.net/miltfspec.htm. Last accessed 16 February 2023.

[23] Civil jet aircraft design, data sets, "Data b : Engine data file : Pratt & whitney engines." URL: https://booksite.elsevier.com/9780340741528/appendices/data-b/table-3/default.htm. Last accessed 15 February 2023.

[24] Daidzic, Nihad E., "Estimation of performance airspeeds for high-bypass turbofans equipped transport-category airplanes," *Journal of Aviation Technology and Engineering*, 2016.

[25] M. Bartel, T. Young, "Simplified thrust and sfc calculations of modern two-shaft turbofan engines for preliminary aircraft design." DOI: https://doi.org/10.2514/6.2007-7847, 2012.

[26] P. Sforza, *Commercial Airplane Design Principle*. Butterworth-Heinemann, 2014.

[27] "Data section 2022." URL: https://www.goodyearaviation.com/resources/pdf/Data-Section-2022.pdf. Last accessed 16 February 2023.

[28] M. H. D. Jorgensen, *The AGAS 2000 Precision Airdrop System*. AIAA, 2005.

[29] "Joint precision airdrop system (jpads)." URL: https://asc.army.mil/web/portfolio-item/cs-css-joint-precision-airdrop-system-jpads/. Last accessed 25 April 2023.

[30] Centers for Disease Control and Prevention, "Get the facts: Data and research on water consumption." URL: https://www.cdc.gov/nutrition/data-statistics/plain-water-the-healthier-choice.html, January 2018. Last accessed 20 February 2023.

[31] Backcountry Survival, "What's the minimum amount of water needed to survive?." URL: https://www.backcountrysurvival.co.uk/2016/05/20/minimum-amount-of-water-needed-to-survive/. Last accessed 10 May 2023.

[32] "Icom france, ic-sat100m." URL: https://www.icom-france.com/en/produit/IC-SAT100M.php. Last accessed 26 April 2023.

[33] Ansys, "Granta design ces edupack software 2018." URL: https://www.ansys.com/products/materials/granta-edupack.

[34] I. Kroo, *Aircraft Design: Synthesis and Analysis*. Stanford, CA 94309: Desktop Aeronautics, January 2001.

[35] R. D. Finck, *USAF Stability and Control DATCOM*. Wright-Patterson AFB, 1978.

[36] M. Cook, *Flight Dynamics Principles*. Elsevier, 2007.

[37] A. Crovato, A. P. Prado, P. H. Cabral, R. Boman, V. E. Terrapon, and G. Dimitriadis, "A discrete adjoint full potential formulation for fast aerostructural optimization in preliminary aircraft design," *Aerospace Science and Technology*, vol. 138, p. 108332, 2023.

[38] J. Litt *et al.*, *Validation of an Integrated Airframe and Turbofan Engine Simulation for Evaluation of Propulsion Control Modes*. AIAA, 2015.

[39] R. aviation, "Federal aviation regulations." URL: https://www.risingup.com/fars/info/23-index.shtml. Last accessed 09 May 2023.

[40] T. Megson, *Aircraft Structure for Engineering Students: Fourth Edition*. Elsevier, 2007.

[41] "The top 10 highest altitude airports in the world." URL: https://www.airport-technology.com/features/feature-the-top-10-highest-altitude-airports-in-the-world/. Last accessed 25 April 2023.

[42] "Simple flying: How is an aircraft refuel ?." URL: https://simpleflying.com/how-is-an-aircraft-refuled/. Last accessed 25 April 2023.

[43] U. B. of Labor Statistics, "Consumer price index." URL: https://www.bls.gov. Last accessed 15 April 2023.

[44] N. B. of Economic Research, "Inflation dynamics during covid-19." URL: https://www.nber.org/reporter/2021number3/inflation-dynamics-during-covid-19. Last accessed 20 April 2023.

[45] N. Financial, "How has the pandemic impacted inflation." URL: https://blog.nationwidefinancial.com/markets-economy/how-has-the-pandemic-impacted-inflation/. Last accessed 20 April 2023.

[46] A. Group, "Why inflation has spiked since covid – and how that impacts the world of work." URL: https://www.adeccogroup.com/future-of-work/latest-insights/why-inflation-has-spiked-since-covid-and-how-that-impacts-the-world-of-work/. Last accessed 21 April 2023.

[47] U. E. I. A. (EIA), "Petroleum other liquids." URL: https://www.eia.gov/dnav/pet/hist/eer_epjk_pf4_rgc_dpgD.htm. Last accessed 17 April 2023.

[48] IMF, "Climate change indicators dashboard." URL: https://climatedata.imf.org/datasets/b13b69ee0dde43a99c811f592af4e821_0/explore. Last accessed 09 May 2023.

[49] Statista, "Natural disasters in the u.s. - statistics facts." URL: https://www.statista.com/topics/1714/natural-disasters/#topicOverview. Last accessed 09 May 2023.